Title
Modeling of Magnetoelastic Nanostructures with a Fully-coupled Mechanical-Micromagnetic Model and Its Applications

Author
Liang, Cheng-Yen (Charles)

Publication Date
2016

Peer reviewed|Thesis/dissertation

UNIVERSITY OF CALIFORNIA

Los Angeles

Modeling of Magnetoelastic Nanostructures with a Fully-coupled Mechanical-Micromagnetic Model and Its Applications

A dissertation submitted in partial satisfaction of the

requirements for the degree Doctor of Philosophy

in Mechanical Engineering

by

Cheng-Yen Liang

2016

ABSTRACT OF THE DISSERTATION

Modeling of Magnetoelatic Nanostructures with a Fully-coupled Mechanical-Micromagnetic Model and Its Applications

by

Cheng-Yen Liang

Doctor of Philosophy in Mechanical Engineering

University of California, Los Angeles, 2016

Professor Gregory P. Carman, Chair

Micromagnetic simulations of magnetoelastic nanostructures traditionally rely on either the Stoner-Wohlfarth model or the Landau-Lifshitz-Gilbert (LLG) model assuming uniform strain (and/or assuming uniform magnetization). While the uniform strain assumption is reasonable when modeling magnetoelastic thin films, this constant strain approach becomes increasingly inaccurate for smaller in-plane nanoscale structures. In this dissertation, a fully-coupled finite element micromagnetic method is developed. The method deals with the micromagnetics, elastodynamics, and piezoelectric effects. The dynamics of magnetization, non-uniform strain distribution, and electric fields are iteratively solved.

This more sophisticated modeling technique is critical for guiding the design process of the nanoscale strain-mediated multiferroic elements such as those needed in multiferroic systems. In this dissertation, we will study magnetic property changes (e.g., hysteresis, coercive field, and spin states) due to strain effects in nanostructures. in addition, a multiferroic memory device is studied. The electric-field-driven magnetization switching by applying voltage on patterned electrodes simulation in a nickel memory device is shown in this work. The deterministic control law for the magnetization switching in a nanoring with electric field applied to the patterned electrodes is investigated. Using the patterned electrodes, we show that strain-induced anisotropy is able to be controlled, which changes the magnetization deterministically in a nano-ring.

The dissertation of Cheng-Yen Liang is approved.

Christopher S. Lynch

Robert N. Candler

Pei-Yu Chiou

Gregory P. Carman, Committee Chair

University of California, Los Angeles

2016

I dedicate my dissertation work to my family. A special feeling of gratitude goes to my loving parents, Ming-Kuang Liang and Tsuei-Rung Chiou, who always emphasized the importance of education. They not only gave me emotional support, but instilled in me a diligent work ethic and persistent determination to be whatever I wanted to be in life without limitations. And my brother, Li-Yen Liang, who always makes me laugh and can pick up anytime even if we haven't talked for a while.

Table of Contents

List of Figures

Acknowledgements

I have never thought about earning a PhD before I came to UCLA. It was just like a dream. And dreams come true!

I would like to express the appreciation to my committee chair, Professor Gregory Carman, who has the attitude and the substance of a genius: he continually and convincingly encourages me to "Change the world" and enjoy the research adventure in this 5 years. Without his advice, I would not have finished my PhD and this dissertation. Furthermore, I would like to thank my committee members, Professor Chris Lynch, Robert Candler, and Pei-Yu (Eric) Chiou, who gave me inspiration. I would like to thank them for their willingness to review the dissertation and suggestions in my research.

A special thank to Professor Abdon Sepulveda and Scott Keller for their technical discussions and after-meeting beverage time. They also brought me to Barney's multiple times during my PhD career. Both Abdon and Scott encouraged me during my PhD career when I felt discouraged. Without Professor Abdon Sepulveda and Scott Keller, I could not have finished my research.

A great thank you to my friends and labmates at UCLA (Kyle Wetzlar, Scott keller, Scott Strutner, Paul Nordeen, Cai Chen, John Domann, Andres Chavez, Anthony Barra, Ted Lee, Joseph (Devin) Schneider, Qianchang Wang, Chin-Jui (Ray) Hsu, and Hyungsuk Kim), giving me endless laughs, parties, sarcastics, and happy lab environment. I would always remember the word, "Happy boss, Happy us" in AML and in TANMS!

In addition, I would like to thank my friends from Taiwan in Friday Night Group (FNG). We have a lot of fun Friday nights; this helps us release pressure in PhD life.

This work was supported by NSF Nanosystems Engineering Research Center for Translational Applications of Nanoscale Multiferroic Systems (TANMS) Cooperative Agreement Award (No. EEC-1160504).

VITA

Education

2007	M.S. Mechanical Engineering *National Taiwan University, Taiwan*
2005	B.S. Mechanical Engineering *National Chung Cheng University, Taiwan*

Employment History

2010-2016	Graduate Student Researcher *UCLA Active Materials Laboratory (Professor Greg. P. Carman)*
2010-2016	Graduate Student Researcher *NTU Fracture Laboratory (Professor Chien-Ching Ma)*

Publications and conference presentations

- ***Cheng-Yen Liang***, Scott M. Keller, Abdon E. Sepulveda, Wei-Yang Sun, Kyle Wetzlar, Gregory. P. Carman, *"Modeling of Magnetoelatic Nanostructures with a Fully-coupled Mechanical-Micromagnetic Model,"* Nanotechnology 25 435701 (2014)

- ***Cheng-Yen Liang***, Jizhai Cui, Scott M. Keller, Abdon E. Sepulveda, Wei-Yang Sun, Chris Lynch, Gregory. P. Carman, *"Electrical Control of a Single Magnetoelastic Domain Structure on a Clamped Piezoelectric Thin Film – Analysis,"* Journal of Applied Physics 116 123909 (2014)

- ***Cheng-Yen Liang***, Abdon E. Sepulveda, Daniel Hoff, Scott M. Keller, Gregory. P. Carman, *"Strain-mediated Deterministic Control of 360^o Domain Wall Motion in Magnetoelastic Nanorings,"* Journal of Applied Physics (2015)

- JiZhai Cui, ***Cheng-Yen Liang***, EA Paisley, A Sepulveda, JF Ihlefeld, GP Carman, "*Generation of localized strain in a thin film piezoelectric to control individual magnetoelectric heterostructures*," Applied Physics Letters 107 (9), 092903 (2015)

- Hyunmin Sohn, Mark E. Nowakowski, ***Cheng-Yen Liang***, Joshua L. Hockel, Kyle Wetzlar, Scott Keller, Brenda M. McLellan, Matthew A. Marcus, Andrew Doran, Anthony Young, Mathias Kläui, Gregory P. Carman, Jeffrey Bokor, Robert N. Candler, *"Reversible electrically-driven magnetic domain wall rotation in multiferroic RING heterostructures"*, ACS Nano (2015)

- Xu Li , Dorinamaria Carka , ***Cheng-Yen Liang***, Abdon E. Sepulveda , Scott M. Keller , Pedram Khalili Amiri , Gregory P. Carman , Christopher S. Lynch,"*Strain-mediated 180*

degree perpendicular magnetization switching of a single domain multiferroic structure," Journal of Applied Physics 118, 014101 (2015)

- ***Cheng-Yen Liang***, Abdon E. Sepulveda, Scott M. Keller, Gregory. P. Carman, *"Deterministic switching of a magnetoelastic single-domain nano-ellipse using bending,"* Journal of Applied Physics 119, 113903 (2016)

1. Introduction and Literature Review

Recently, multiferroics is becoming an attractive field and stimulating many new research interests which are driven by the complex physics of these materials. Ferromagnetic, ferroelectric, and elastic effects are coupled in multiferroics[1][2]. This opens a new way for developing novel technologies based on these multifunctional materials, such as sensors[3], transducers[3], memory devices[4], and spintronic devices[5].

Multiferroic materials are being studied for use in magnetic random access memory (MRAM) with higher efficiency, lower energy consumption, and lower heating effects than traditional memory devices[4]. Traditional methods use external magnetic fields[6]; however, the switching field increases as the size of the device decreases, which requires high power consumption in high-density magnetic memories. An alternative method is spin-transfer torque approach[37], which uses a spin-polarized current to switch the magnetization in magnetic layers; the current reduces when the device size reduces. However, the current used for reorienting the magnetization is still too high for commercial applications. Using multiferroics for memory applications is a promising approach for controlling the magnetization eliminating the use of currents. In this approach, the magnetization is manipulated by applying electric fields to ferromagnetic/ferroelectric composites. These composites couple the electric field and the magnetization in ferromagnetic/ferroelectric heterostructures, enabling the magnetoelectric (ME) effect. Based on this magnetoelectric coupling effect, new devices can be designed, which reduce power consumption and operate at room temperature since the magnetization is manipulated through electric fields instead of external magnetic fields and currents.

Three main works have been studied to achieve the magnetoelectric effect[63]. The first is the exchange bias method, in which the magnetization is pinned in a reference direction at the interface between antiferromagnetic/ferromagnetic layers[7]. The second is the charge-mediated approach, in which charges are induced at the interface of FM/FE thin films when the electric field is applied. This produces magnetization changes due to the spin-dependent screening of an electric field[8]. The third is to use strains to control the magnetization in the FM/FE heterostructures[9]. The strain is produced by applying an electric field in the ferroelectric layer and the piezoelectric effect. This induced strain is transferred to the ferromagnetic layer, altering the magnetization via magnetostriction. This last method is a novel technique in developing strain-mediated magnetization control for information technologies. The goal of this dissertation is to develop a model, which is able to be used for strain-mediated multiferroic device design and analysis[30][32][42][62].

The organization of this dissertation is as follows. In chapter 1. , previous works will be reviewed. In chapter 2. , a three dimensional numerical method based on finite elements for micromagnetic-elastodynamics coupled simulations will be developed. The analytical results on single domain nanostructures are compared to both conventional analytical methods and experimental results to validate the model. In chapter 3. , magnetization switching dynamics in a multiferroic single domain memory bit will be predicted. The response of this multiferroic nanoscale structure and thick substrate clamping problem will be discussed. In chapter 5. , deterministic electric field control of 360^{o} domain wall motion in a nano-ring is demonstrated using patterned electrodes and two alternative electrode architectures are studied. In chapter 6. , we conclude the work in this dissertation and future works are provided at the end of the chapter.

1.1 Stoner-Wolhfarth Model

Micromagnetic theory is to analyze magnetization processes and domain structures and to calculate the spin structures of domain wall in on sub-micrometer length scales. In micromagnetics, Stoner–Wohlfarth theory was proposed by Stoner and Wohlfarth in 1948[10]. It is the simplest static model for calculating the magnetization in small particles and for MRAM and computer storage applications[11]. The Stoner–Wohlfarth model assumes that the magnetization in a small particle behaves as single magnetic domain and the rotation of the magnetization is coherent. The exchange energy is assumed constant and has no influence on the rotation of the magnetization since the particle is assumed single domain. The energy terms considered in the model are the Zeeman energy and the anisotropic energy. Those energy terms compete with each other, causing the magnetization changes. Types of the anisotropic energy include magnetocrystalline anisotropy, strain-induced anisotropy, and shape anisotropy (demagnetization)[10]. Therefore, the energy in the Stoner–Wohlfarth model can be expressed as

$$E = E_u + E_\sigma + E_d + E_z$$
$$= K_u \sin^2(\varphi - \theta) + \frac{3}{2}\lambda_s \sigma \sin^2(\varphi - \theta) + \left(\mu_0 M_s (N_\perp - N_\parallel)\right) \sin^2(\varphi - \theta)$$
$$- \mu_0 M_s H cos(\theta)$$

where E_u is the uniaxial anisotropic energy, E_σ is the strain-induced anisotropic energy, , E_d is the shape (demagnetization) anisotropic energy, and E_z is the Zeeman energy from applied fields. K_u is the uniaxial magnetocrystalline anisotropic constant, λ_s is the magnetostriction, σ is the uniaxial stress applied to the small particle, M_s is the saturation magnetization, $N_\perp, N_\parallel$ are the

demagnetization factor perpendicular and parallel to the easy axis, and μ_0 is the permeability of free space.

Previously, influences of stress in the coercive force behavior and hysteresis curves in thin films have been done by using the Stoner–Wohlfarth model. *Callegaro et al.* constructed a model based on bi-dimensional Stoner–Wohlfarth model in which the magnetostriction, intrinsic anisotropy, and applied field interactions between electroplated nickel film grains was considered[13]. *Sablik et al.* used a modified the Stoner–Wohlfarth model and a domain wall pinning model[58] for the magnetic hysteresis and coercivity of a ferromagnetic material consisting with single domain grains under torsion[14]. *Szaboet al.* studied the magnetization behavior of the Stoner–Wohlfarth particle with linear excitation and in a rotational magnetic field[15]. This work showed that the variation of the magnetization vector can have jumps and that these jumps correspond to the Barkhausen effect[59]. *Peng et al.* demonstrated that the applied stress on the thin film has a significant effect on the shapes of the hysteresis curves[16]. They also found that the coercivity increases as the longitudinal tensile stress increases. The magnetostriction of the amorphous thin film is strongly influenced by the applied stress.

The stress effect was not only studied in the thin films, but also in bulk ferromagnetic materials. When a ferromagnetic bulk material is subjected to stresses, the magnetic domains in the material change. The mechanism is that an anisotropic energy is induced in the ferromagnetic body by stresses and is called the stress-induced anisotropy. *IZAWA et al.* analyzed the stress-induced anisotropy in ferromagnetic materials. They found that the magnetization reversal can take place for small stresses if a sufficient demagnetizing field exists[17]. *Sablik et al.* studied the effect of biaxial stress on magnetoelastic processed polycrystalline bulk steels. They used the effective stress equal to one of the deviatoric normal stress components in the Schneider-

Cannell-Watts model for stress-induced hysteresis curves changes[18]. *Jiles et al.* proposed a new theoretical model in which the mechanism in the change of magnetization is the unpinning of domain walls when subjected to an applied uniaxial stress[19]. *Callegaro* showed that the effect of stress on the coercive force is completely different for thin and thick films. The magnetic properties of the thick nickel film behave like bulk nickel, whereas results on lower thicknesses show a continuous transition from thin film to bulk-like behavior[20]. *Chen and Jiles et al.* studied the magneto-mechanical effect in magnetic materials under torsional stress and the relationship. They investigated the change of magnetization as a function of applied torque for cylindrical ferromagnetic rods. They showed substantial changes in surface field at remanence under torsion[21]. *Bulte et al.* presented a hypothesis to explain the mechanism that externally applied stresses can affect the magnetic properties of ferromagnetic materials. They explained that the magneto-mechanical effect results from the spin–spin and spin–orbit coupling interactions with magnetic moments, which in turn alters the magnetocrystalline anisotropy and exchange energies in ferromagnetic materials[22]. *Mudivarthi et al.* derived the relationship for magnetoelastic, elastic, and mechanical work. They showed that the magnetoelastic, elastic, and mechanical energies are identical to the stress-induced anisotropy with magnetostriction-induced fourth order anisotropy, which is able to be used in the analysis of the change in magnetization due to stress in magnetostrictive materials. They also provided an expression for energy density which is suitable for 3-dimensional magneto-mechanical coupling magnetization dynamics[23].

1.2 Micromagnetics (Landau-Lifshitz-Gilbert Equation, LLG)

The Stoner–Wohlfarth model is based on the minimization of the free energy for a ferromagnetic material. These approaches allow us to predict the equilibrium configurations for the material. The assumptions of this approach are single domain particles and coherent magnetization behaviors. However, challenges appear when using these concepts for memory applications, estimation of time response, and design of multiferroic devices. Therefore, magnetization dynamics becomes the most important topic in micromagnetic analysis. Recently, the dynamics of magnetization analysis is based on the phenomenological equation, the Landau-Lifshitz-Gilbert equation, developed by Landau and Lifshitz in 1935[24]. They proposed a dynamical model for the precessional motion of the magnetization. This model was based on a continuum precession equation and quantum-mechanical effects. The anisotropy and dissipation in the approach were introduced phenomenologically by means of the effective field.

T. L. Gilbert successively modified the phenomenological Landau-Lifshitz equation[25], which could not account for the large noneddy-current damping in thin Permalloy sheets. The problem undertaken in this study was to reform Landau-Lifshitz equation with the theory of damping in physical systems such that large damping is able to be taken into consideration. Gilbert started the phenomenological theory of an un-damped and uncoupled magnetization, which is based on a classical variational principle. The equations of motion are derived from the potential energy of the magnetization field via this variation procedure. Furthermore, he introduced a damping term by using a Lagrangian formulation for the equations of motion and added a velocity-dependent term derived from the Rayleigh's dissipation function. The modified Landau-Lifshitz equation was derived with the damping term and can be used with large

damping conditions. He also mentioned that the damping terms in the Landau-Lifshitz equation and the modified equation are identical.

Using a modified Landau-Lifshitz equation, *Kikuchi* found that the minimum magnetization reversal time corresponds to a critical value of the damping constant in a single-domain sphere and an infinitely-wide thin single-domain sheet of ferromagnetic material[26]. *Visintin* incorporated Maxwell's equations, mechanical equations of motion, and constitutive equations into the Landau-Lifshitz's equation. In addition, He provided magnetic energy functionals for the anisotropic energy and exchange energy in the equation. Finally, he proved that the Landau-Lifshitz's equation has a solution but it is not unique[27]. *Mallinson* discussed the relationship between the Landau-Lifshitz equation and the modified Landau-Lifshitz-Gilbert equation[28]. He showed that the underlying physics is different even though the equations have the identical mathematical form. He found that the Landau-Lifshitz equation cannot be strand for a lager damping condition, it is only valid in the small damping case. On the other hand, the Gilbert-modified Landau-Lifshitz equation is valid in the large damping case.

1.3 LLG + Elastodynamics

Currently, since the applications for strain-mediated multiferroic devices are increasing. The stress/strain effects on the dynamics of magnetization have become a popular topic in micromagnetics. In addition, with the development of the computer technology, complex micromagnetic problems can be solved by the use of numerical methods.

Voltairas et al. presented a simple micromagnetic model to study the inverse magnetoelastic effect on the coercivity and remanence magnetization in ferromagnetic thin films. The method was constrained to be a one-dimensional plane strain model with an external magnetic field applied parallel or perpendicular to the stress direction[29]. *Zhu et al.* studied the effect of stress on the magnetic properties of thin films. In this study, they found that due to the inverse magnetoelastic effect, a negative strain decreases the coercivity while a positive strain increases in a nickel film[30]. *Shu et al.* proposed a two-dimensional framework to deal with the issues of loss of strain compatibility and negligence of intrinsic stresses[31]. Their framework was based on micromagnetics in order to explore the effects of stress on the magnetostrictive behavior in thin films. The simulation had good prediction domain patterns an hysteresis in small magnetostrictive materials (nickel) while crude prediction for magnetostrictive materials(Terfenol-D). *Zhang and Chen* used a phase-field microelasticity theory of Khachaturyan[61] coupled with the micromagnetic model to predict the magnetic domain structures and temporal evolution in giant magnetostrictive materials[32]. They studied the effects of elastic energy and magnetostatic energy on magnetic domain structures. Mechanical equilibrium is included in their model in order to take into account strains inside the domain structures. *Banas et al.* provided a numerical 2D scheme for modeling the Landau-Lifshitz-

Gilbert equation (LLG) coupled with the equation of elastodynamics. The model describes the behavior of ferromagnetic materials when mageto-mechanical coupling is taken into account[33]. *Hu et al.* carried out a micromagnetic simulation to study the stress effects on hysteresis curves and magnetization dynamics. In this article, they used the fast Fourier transform method in reciprocal space for solving the temporal Landau-Lifshitz-Gilbert equation. Simulations were performed to study the effect of uniaxial stress on the magnetic hysteresis in a magnetic material[34]. *Dean et al.* developed a method, in which they implemented complex deformational changes for magnetoelastic effects in micromagnetic simulations. The Cauchy stress tensor was taken into account in their approach. Stress variations were calculated and implemented in the micromagnetic simulations[35]. *Bur Et al.* reported strain-induced induce coercive field changes in patterned single-domain nickel nanostructures deposited on Si/SiO2 substrate. Experimental data is compared with micromagnetic simulations with uniform and non-uniform strain conditions. The strain conditions were calculated using finite element method and the results were fed to a micromagnetic simulator code with effective magnetoelastic anisotropy[36].

Dynamics of magnetization due to spin torque transfer effects and eddy currents have also been studied recently. *Slonczewski* proposed a new mechanism for exciting the magnetic state of a ferromagnet, he predicted that transfer of vectorial spin accompanies an electric current flowing perpendicular to two parallel magnetic films connected by a normal metallic spacer with the assumption ballistic conditions[37]. *Berger et al.* studied the spin torque transfer effect. In his work, the interaction between spin waves and itinerant electrons is considerably enhanced in the vicinity of an interface between normal and ferromagnetic layers in metallic thin films[38]. *Bertotti et al.* presented an analytical technique to predict the effect of eddy currents on the

magnetization dynamics in metallic thin films. Due to eddy current effects, the magnetization is no longer uniform across the conducting film thickness. With the effective damping constant approximation and neglecting the exchange effects, the magnetization dynamics in metallic films can be predicted by using LLG equation[39]. *Monk et al.* proposed an eddy-current micromagnetic model to describe the eddy current magnetization behavior in ferromagnetic films due to field. The existence and uniqueness of a weak solution of the eddy current-LL model are proven in this work[40]. *Iyer et al.* studied the modified Landau-Lifshitz-Gilbert (LLG) equation for a conducting, magnetic body. They derived a well-defined expression for the magnetic field due to eddy current losses. They showed that the work done by eddy currents is a Rayleigh type dissipation function opposing the change in magnetization[41].

1.4 LLG + Piezoelectric Constitutive Equations

W. Eerenstein et al. demonstrated electrically induced giant magnetic changes at a single epitaxial interface in LSMO films on BTO substrates. In this study, the switching of BTO domains alters in LSMO the local strain, magnetic anisotropy and thus the magnetization. The magnetoelectric coupling at the interface of magnetic/ferroelectric thin film over a wide range of temperatures is obtained and it is able to inspire further study with single epitaxial interfaces[42]. *Pertsev et al.* presented a theoretical model for magnetization rotation induced by electric field applied to the substrate in nickel/CFO epitaxial heterostructure. They showed that magnetization reorientation occurs at small strains and also predicted a large magnetoelectric susceptibility in the ferromagnetic/ferroelectric heterostructures[43]. *Atulasimha et al.* showed that magnetization rotation in a multiferroic nickel/PZT nanomagnet can be controlled by applying the electric field on the piezoelectric layer. In addition, Bennett clocking is presented in nanomagnetic logic

arrays resulting in unidirectional propagation of logic bits from one stage to another. Micromagnetic simulations are performed for this multiferroic nanomagnet chain. Results show that The stress-induced anisotropy generated in the nickel layer due to strain can rotate the second magnet out of the initial state upon removal of the stress. The energy dissipated in this method is lower than that in spin-transfer torque for magnetization rotation[44]. *Roy et al.* studied the switching dynamics of a single-domain magnetostrictive/piezoelectric nanomagnet subjected to in-plane stress. The voltage was applied through the piezoelectric thickness, generating mechanical strains. The strain is assumed fully-transferred to the magnetostrictive layer by elastic coupling. Since the strain is generated in the magnetostrictive layer, the easy axis changes due to the stress-induced uniaxial anisotropy, causing 90^{o} magnetization rotation. The effect of the voltage ramp rate on the reversal time, response time magnetization rotation and the switching time due to stress and material properties have also been discussed[45]. *Fashami and Roy et al.* studied the magnetization dynamics of a multiferroic Terfenol-D/PZT logic chain with nearest-neighbor dipole coupling using the LLG equation. Low-energy dissipation nanomagnetic logic (NML) bits was designed in their work[46]. *Livesey et al.* derived the magnetoelectric coupling term in piezoelectric/magnetostrictive thin film heterostructures using Landau-Ginzburg free energy expansion in terms of strain, magnetization, and electric polarization. The FMR frequency shift in the in BTO/NFO superlattice is calculated and may result from the geometry and strain boundary conditions[47]. *Hu et al.* used the phase-field model, coupled with the time-dependent Ginzberg-Landau equation (TDGL) and the Landau-Lifshitz-Gilbert equation (LLG) to study the magnetic domain switching in CoFeB/BTO heterostructures grown on a substrate. In this article, they presented the 90^{o} perpendicular domain can be switched in the magnetic layer due to electromechanical strains originating from the FE layer[48]. *Zavaliche et*

al. presented the magnetization reversal induced by an electric field in the BFO/CFO vertical heterostructure. In the article, they showed that an electric field applied to the piezoelectric matrix leads to a change in its shape during switching, which dynamically alters the magnetic anisotropy of the ferrimagnetic pillars via their magnetostriction. Therefore, magnetization reversal is induced through the application of an electric field to the columnar ferroelectric/ferrimagnetic epitaxial nanocomposite. Magnetization has shown to be a function of temperature, strain and magnetic field work[49]. *Thiele* investigated the influence of a reversible biaxial strain on the magnetization M of epitaxial LSMO manganite films deposited on a PMN-PT single crystal substrate[50]. *Moutis et al.* studied the electric-field modulation of coercive field Hc through the inverse piezoelectric (PE) effect in a periodic array of CoFe stripes patterned on a commercial PZT substrate. They showed that the coercive field Hc is dependent on the piezo-strain of the ferroelectric substrate applied under the electric field[51]. *Brandlmaier et al.* showed that the ferromagnetic anisotropy of a thin magnetic crystalline film can be manipulated in situ via the application of stress. They experimentally demonstrated that the magnetic anisotropy of the magnetic thin film can be reoriented with the piezo-actuator[52]. *Chung et al.* studied the magnetic domain change using an electric field in a nickel/PZT thin film due to the magnetoelectric effects. They experimentally demonstrated magnetic domain changes when the electric field was applied to the PZT thin film[53][54]. *Brintlinger et al.* reported direct observation controlled and reversible switching of magnetic domains using static electric fields applied in situ during Lorentz microscopy. The strain in this study is assumed fully-transferred from the BTO layer to the FeGa layer. Domain wall motion was observed when the mechanical strain was applied to the magnetic thin film. Simulations based on the object-oriented micro-magnetic framework (OOMMF) were performed for comparison[55]. *Tuomas et al.* reported an

approach to electrically control local magnetic properties, including the writing and erasure of regular ferromagnetic domain patterns and the motion of magnetic domain walls, in CoFe-BTO heterostructures. It is shown that domain correlations and strong inter-ferroic domain wall pinning persist in an applied electric field[56]. *Geprags et al.* used a ferromagnetic/PZT actuator composite with mechanical strain effect to show the nonvolatile switching for the remanent magnetization in single-crystalline ferromagnets. They demonstrated that the voltage-induced strain causes nonvolatile 90^0 remanent magnetization rotation[57].

Previous literatures have been shown to obtain the magnetization equilibrium state with Stoner-Wolhfarth model and OOMMF. Those methods assumed small single domain elements, uniaxial shape anisotropy with one anisotropy constant. In addition, to deal with strain-mediated magnetization dynamics, strain is assumed to be uniformly distributed within the magnetic elements. Effective strain-induced anisotropy is the term implemented in those methods. Strain and magnetization state are not iteratively simulated in the models. This is sufficient to describe highly symmetric cases like a prolate spheroid of revolution or ferromagnetic/ferroelectric thin film heterostructures. However, real systems are often more complex, and strain variations in FM/FE heterostructures and the effects in micromagnetics with elastodynamics and piezoelectrics are coupled.

In this dissertation, a fully-coupled finite element micromagnetic method is developed. The method deals with the micromagnetics, elastodynamics, and piezoelectric effects. The dynamics of magnetization, non-uniform strain distribution, and electric fields are iteratively solved. Initial conditions for magnetization starts arbitrarily. For every configuration (time step) a new demagnetization field, strain state and magnetic fields are solved. New fields and strain states are used for calculating the effective field, which in turn yields a new magnetic moment

state through micromagnetics. These steps are iterated until equilibrium state is achieved. This model is validated by experimental data and the simulated results are also compared with the experiments.

2. Modeling of Magnetoelastic Nanostructures with a Fully-Coupled Mechanical-Micromagnetic Model

Micromagnetic simulations of magnetoelastic nanostructures traditionally rely on either the Stoner-Wohlfarth model or the Landau-Lifshitz-Gilbert (LLG) model assuming uniform strain (and/or assuming uniform magnetization). While the uniform strain assumption is reasonable when modeling magnetoelastic thin films, this constant strain approach becomes increasingly inaccurate for smaller in-plane nanoscale structures. This chapter presents analytical work to significantly improve simulation of finite structures by fully coupling LLG with elastodynamics, i.e. the partial differential equations are intrinsically coupled. The coupled equations developed in this manuscript along with Stoner-Wohlfarth model and LLG (constant strain) are compared to experimental data on nickel nanostructures. The nickel nanostructures are 100x300x35 nm single domain elements fabricated on a Si/SiO_2 substrate, which are mechanically strained while experiencing an applied magnetic field to generate M vs. H curves. Results reveal that this chapter's fully-coupled approach is significantly superior regarding agreement with experimental data on coercive field changes. This more sophisticated modeling technique is critical for guiding the design process of future nanoscale strain-mediated multiferroic elements such as those needed in memory systems.

2.1 Introduction

Electrical control of ferromagnetic elements represents an important and emerging area of study in multiferroics. Magnetic control has conventionally been accomplished using an applied magnetic field rather than an electric field. Recently a number of relatively newer methods for controlling magnetization have been studied including carrier-mediated ferromagnets[64][65], exchange coupled multiferroic interfaces[66][67], and spin-transfer torque[68][69][70]. While these areas represent important topics, electrically induced strain-mediated control of magnetic properties may represent a more promising approach in the near term. This statement is based on the relative maturity of both piezoelectric and magnetostrictive materials required for the strain mediated multiferroics approach, i.e. new materials are unnecessary. One application for strain-mediated multiferroics is in magnetic random access memory (MRAM) where substantial reduction in write energies are possible[71][72]. However, a robust modeling approach that accurately predicts the nanoscale structures magnetic response is presently unavailable.

The strain-mediated multiferroic approach consists of mechanically coupling magnetoelastic elements onto ferroelectric substrates[73][74][75], e.g. sputter deposition of composite heterostructures[78][79][80]. In these composites, an electric field applied to the ferroelectric/piezoelectric substrate induces an anisotropic strain in the magnetoelastic material. The anisotropic stain induces a magnetic anisotropy via the converse magnetoelastic effect[76][77]. There exist fairly extensive studies containing both theoretical and experimental work on strain-mediated magnetization changes, coercivity changes[81], and strain-induced anisotropy in continuous magnetic thin films[82]. In all of the continuous film studies the strain is appropriately assumed to be fully-transferred from the ferroelectric to ferromagnetic layer by

treating the magnetoelastic energy as a pure uniaxial anisotropy applied to the magnetic media. For example, T. Brintlinger et al. reported both experimental and analytical predictions using OOMMF and constant strain assumptions to show reversible switching in FeGa/BTO thin film[55]. In recent years several additional studies, such as ferroelectric/ferromagnetic film coupling by Lahtinen et al.[56] and magnetic thin film stress modeling by Bai et al.[84], have demonstrated that this constant strain methodology works reasonably well for continuous thin films[86].

A relatively less studied area is the strain-mediated effect in multiferroic nanostructures[87]. For example, Bur et al. reported strain-induced coercive field changes in patterned single-domain nickel nanostructures deposited on Si/SiO_2 substrates[36]. Bur's study showed that the coercive field is a direct function of applied strain due to the magnetoelastic effect. In this work, experimental data was compared to micromagnetic simulations with uniform and non-uniform strain conditions[36]. However, the strain states were calculated before performing the micromagnetic simulation, thus the governing equations were not fully coupled. A few studies also exist on uniform strain transfer and strain-induced change of magnetization in nanostructures[44][45] [87]; however, as the thickness of the nanostructures increases or in-plane dimensions decrease, the validity of the fully-transferred strain assumption becomes increasingly compromised[35][85] [90]. Therefore, more sophisticated modeling is required.

Recently, researchers have begun to investigate more sophisticated modeling techniques for coupling LLG with elastodynamics. These approaches include mathematical [33][91][92][93]and numerical methods[30][31][32][34][94]for the solutions of coupled micromagnetic and elastodynamic equations. The mathematical approach includes showing the existence and convergence of the coupled solutions, such as those presented by Banas et al.[33]

and Alouges et al.[91] Numerical approaches have also been presented by Y.C.Shu et al.[31] using a numerical framework to explore stress effects on magnetoelastic thin film behavior, and by Mieche and Ethiraj for describing magnetic and mechanically effects on micron size magnetic domains structures[94]. More recently, Zhang and Chen used a phase-field method to combine micromagnetic and elastodynamic equations for predicting magnetic domain structures and their temporal evolution in magnetoelastic materials[32]. Micromagnetic coupled models have also been previously used to analyze the magnetic domain switching behavior in ferromagnetic/ferroelectric heterostructures when an electric field is applied to the ferroelectric layer[32][87][95][96]. While a few sophisticated solutions have been presented, these presentations do not compare their data directly with experimental results and thus leaves the modeling approaches questionable.

In this chapter, we develop a numerical method based on finite elements to fully-coupled micromagnetic simulations with elastodynamics in finite size 3D structures. The analytical results are compared to both conventional analytical methods and experimental results. The new coupled model provides an approach to simultaneously solve the full strain and micromagnetic spin distribution in the finite composite system as a function of position and time. In this chapter, the strain-induced coercive changes in a nickel nanostructure elastically coupled to a Si/SiO_2 substrate is investigated. Displacements are applied to the substrate producing strain and magnetic spin variations in the nickel nanostructure. Magnetic hysteresis curves at constant strain are predicted and compared to the Stoner-Wohlfarth (SW) [97][98]and the Landau-Lifshitz-Gilbert (LLG) model [24][25] assuming uniform strain. Comparing these analytical results with the experimental data by Bur et al.[36] revealed that the strain distribution significantly influences the magnetic hysteresis curves and the coercive fields. We demonstrate

that the new coupled model results are in significantly better agreement with the experimental data when contrasted with the Stoner Wohlfarth or LLG model assuming uniform strain.

2.2 Theory

In this section, we derive the theoretical magnetoelastic framework for a problem between micromagnetics and elastodynamics. The methodology, in differential form, reduces to seven coupled PDEs, which in turn are formulated in their weak form. Assumptions include small elastic deformations, linear elasticity, magnetostatics, and negligible electrical current contributions. In this work we have not included the piezoelectric relations which would be trivial to add into the formulations; the test data used by Bur et al.[36] relied on mechanical loading rather than electric field loading.

The equilibrium for magnetic systems is characterized by local minima of the total free energy density E_{tot}, written as[24][25] [32]

$$E_{tot} = E_{ext} + E_{ex} + E_{anis} + E_d + E_{el} \tag{2-1}$$

which consists of the external energy density E_{ext} in an applied external field, the exchange energy density E_{ex}, the magnetocrystalline anisotropy energy density E_{anis}, the demagnetization energy density E_d, and the elastic energy density E_{el}.

The E_{ext} is produced by the applied magnetic field $\underline{H}_{ext}$ and is expressed as

$$E_{ext} = -\mu_0 M_s \left(\underline{m} \cdot \underline{H}_{ext} \right) \tag{2-2}$$

where $\underline{m}$ is the magnetization normalized by the saturation magnetization M_s, and μ_0 is the permeability of free space. E_{ex} is defined by the magnetization gradient and the exchange stiffness constant A_{ex} as [24][25]

$$E_{ex} = A_{ex}\left(\nabla \underline{m}\right)^2 \tag{2-3}$$

The anisotropy energy density E_{anis} for a cubic crystal is defined as [25][31][32]

$$E_{anis} = K_1\left(m_1^2 m_2^2 + m_2^2 m_3^2 + m_3^2 m_1^2\right) + K_2\left(m_1^2 m_2^2 m_3^2\right) \tag{2-4}$$

where K_1 and K_2 are cubic anisotropy constants. Equation (2-4) must be modified to account for hexagonal or uniaxial crystals. The demagnetization energy density E_d is given by[25][97]

$$E_d = -\frac{1}{2}\mu_0\left(M_s \underline{m} \cdot \underline{H}_d\right) \tag{2-5}$$

where $\underline{H}_d$ is the demagnetization field. $\underline{H}_d$ is determined from Ampere's law ($\nabla \times \underline{H}_d = 0$), Gauss's law ($\nabla \cdot \underline{B} = 0$), and the relation between the magnetic induction $\underline{B}$ and magnetization $\underline{m}$ as[99]

$$\underline{B} = \underline{H}_d + M_s \underline{m} \tag{2-6}$$

$\underline{H}_d$ is related to the gradient of a magnetic potential ϕ by using Ampere's law,

$$\underline{H}_d = -\nabla\phi \tag{2-7}$$

The elastic energy density term (E_{el}) in Eq.(2-1) can be written as[31][32][33]

$$E_{el} = \frac{1}{2}\underline{\underline{\varepsilon}}^{el} : \underline{\underline{\underline{\underline{C}}}} : (\underline{\underline{\varepsilon}}^{el}) \tag{2-8}$$

where $\underline{\underline{\underline{\underline{C}}}}$ is the elastic stiffness tensor and $\underline{\underline{\varepsilon}}^{el}$ is the elastic strain tensor of the material.

In magnetostrictive materials, magnetic moments and displacements are coupled. Therefore, the total strain $\underline{\underline{\varepsilon}}$ in a ferromagnetic material is composed of magnetic ($\underline{\underline{\varepsilon}}^{m}\left(\underline{m}\right)$) and elastic ($\underline{\underline{\varepsilon}}^{el}$) contributions as [33]

$$\underline{\underline{\varepsilon}} = \underline{\underline{\varepsilon}}^{m}\left(\underline{m}\right) + \underline{\underline{\varepsilon}}^{el} \tag{2-9}$$

where $\underline{\underline{\varepsilon}}^{m} = \underline{\underline{\underline{\underline{\lambda}}}}^{m}\,\underline{m}\underline{m}^{T}$ is the strain associated with local magnetization changes and $\underline{\underline{\underline{\underline{\lambda}}}}^{m}$ is the magneto-mechanical coupling tensor. In the case of a cubic crystal, $\underline{\underline{\varepsilon}}^{m}$ is given by [31][32][33]

$$\varepsilon_{ij}^{m} = \begin{cases} \frac{3}{2}\lambda_{100}\left(m_i m_j - \frac{1}{3}\right) & i = j \\ \frac{3}{2}\lambda_{111} m_i m_j & i \neq j \end{cases} \tag{2-10}$$

where λ_{100} and λ_{111} are the magnetostriction constants along the $\langle 100 \rangle$ and $\langle 111 \rangle$directions. For hexagonal or uniaxial crystals, equation (2-10) would need to be modified.

The total strain $\underline{\underline{\varepsilon}}$ is related to the displacement $\underline{u}$ by [31][32][33]

$$\underline{\underline{\varepsilon}} = \frac{1}{2}\left(\nabla\underline{u} + \left(\nabla\underline{u}\right)^{T}\right) \tag{2-11}$$

and the stress tensor $\underline{\underline{\sigma}}$ is related to the strains as

$$\underline{\underline{\sigma}} = \underline{\underline{\underline{\underline{C}}}}\,\underline{\underline{\varepsilon}}^{el} = \underline{\underline{\underline{\underline{C}}}}\left[\underline{\underline{\varepsilon}} - \underline{\underline{\varepsilon}}^{m}\left(\underline{m}\right)\right] \tag{2-12}$$

where the stress distribution is governed by the elastodynamic equation

$$\rho\frac{\partial^2 \underline{u}}{\partial t^2} - \nabla\cdot\underline{\underline{\sigma}} = \underline{0} \tag{2-13}$$

and ρ is the mass density.

The effective magnetic field $\underline{H}_{eff}$ is obtained by differentiating the total energy density (Eq.2-1) with respect to magnetization [24][31][32][33][97]

$$\underline{H}_{eff} = -\frac{1}{\mu_0 M_S}\frac{\partial E_{tot}}{\partial \underline{m}} = \underline{H}_{ext} + \underline{H}_{ex} + \underline{H}_{anis} + \underline{H}_{d} + \underline{H}_{me}\left(\underline{m},\underline{u}\right) \tag{2-14}$$

where $\underline{H}_d$ is defined in Eq. (2-7), $\underline{H}_{ext}$ is the applied external field, and [24][25][31][32][33]

$$\underline{H}_{ex} = \frac{2A_{ex}}{\mu_0 M_s}\Delta\underline{m}$$

$$H^{i}_{anis} = -\frac{2m_i}{\mu_0 M_S}\left[K_1\left(m_j^2 + m_k^2\right) + K_2\left(m_j^2 m_k^2\right)\right] \tag{2-15}$$

$$\underline{H}_{me} = -\frac{1}{\mu_0 M_S}\underline{\underline{\underline{\underline{C}}}}\left(\underline{\underline{\varepsilon}} - \underline{\underline{\varepsilon}}^{m}\left(\underline{m}\right)\right)\cdot\frac{\partial \underline{\underline{\varepsilon}}^{m}\left(\underline{m}\right)}{\partial \underline{m}}$$

The effective field $\underline{H}_{eff}$ term is used in the phenomenological Landau-Lifshitz-Gilbert (LLG) micromagnetic relation [24]

$$\frac{\partial \underline{m}}{\partial t} = -\mu_0\gamma\left(\underline{m}\times\underline{H}_{eff}\right) + \alpha\left(\underline{m}\times\frac{\partial \underline{m}}{\partial t}\right) \tag{2-16}$$

where γ is the Gilbert gyromagnetic ratio and α is the Gilbert damping constant.

Equations (2-1) - (2-16) represent a system of equations describing the magnetoelastic response of a coupled micromagnetic-mechanical system. This set of equations can be reduced further; using Gauss's law ($\nabla \cdot \underline{B} = 0$) and Eqs. (2-6) and (2-7), the magnetic potential ϕ satisfies the Poisson equation

$$\nabla^2 \phi = \nabla \cdot \left(M_s \underline{m} \right) \tag{2-17}$$

Substituting Eqs. (2-11) and (2-12) with the expression for $\underline{\underline{\varepsilon}}^m \left(\underline{m} \right)$ into Eq. (2-13) which reduces to modified a partial differential equation relating to the displacements $\underline{u}$ and the magnetization $\underline{m}$:

$$\rho \frac{\partial^2 \underline{u}}{\partial t^2} - \nabla \cdot \underline{\underline{\underline{\underline{C}}}} \left[\frac{1}{2} \left(\nabla \underline{u} + \left(\nabla \underline{u} \right)^T \right) \right] + \nabla \cdot \underline{\underline{\underline{\underline{C}}}} \left(\underline{\underline{\underline{\lambda}}}^m \underline{m} \underline{m}^T \right) = \underline{0} \tag{2-18}$$

Combining Eqs. (2-14) and (2-16) produces the final three partial differential equations as a function of the displacement $\underline{u}$, the magnetic potential ϕ, and the magnetization $\underline{m}$:

$$\frac{\partial \underline{m}}{\partial t} = -\mu_0 \gamma \left(\underline{m} \times \left(\underline{H}_{ext} + \underline{H}_{ex}(\underline{m}) + \underline{H}_d(\phi) + \underline{H}_{anis}(\underline{m}) + \underline{H}_{me}(\underline{m}, \underline{u}) \right) \right) + \alpha \left(\underline{m} \times \frac{\partial \underline{m}}{\partial t} \right) \tag{2-19}$$

Equations (2-17), (2-18), and (2-19) are a system of the seven coupled partial differential equations for the seven unknown variables represented by $\underline{u}$, ϕ, and $\underline{m}$. To solve this system of

coupled equations, the PDEs are formulated in their weak forms. The weak form of Eq. (2-17) is obtained by multiplying with a test functions ζ, which satisfies boundary conditions and the governing equation with this set integrated over the volume Ω. After integrating by parts and using the divergence theorem, we obtain [99][101]

$$-\int_{\Omega}(\nabla\phi)\frac{\partial\zeta}{\partial\underline{x}}d\Omega+\int_{\Omega}\left(M_s\underline{m}\right)\frac{\partial\zeta}{\partial\underline{x}}d\Omega=0 \tag{2-20}$$

with prescribed magnetic potential boundary conditions[99],

$$\begin{cases}\phi_{in}=\phi_{out}\\ \dfrac{\partial\phi_{in}}{\partial n}-\dfrac{\partial\phi_{out}}{\partial n}=-\left(M_s\underline{m}\right)\cdot n\end{cases}\quad\text{on } S \tag{2-21}$$

where ϕ_{in} and ϕ_{out} are the inner and outer magnetic potentials and $\hat{n}$ is the unit normal to the surface S.

Similarly, the weak formulation for Eq. (2-18) is obtained by multiplying with a test vector function ($\underline{\eta}$) and integrating over the volume Ω. After integrating by parts and applying the divergence theorem, we obtain[31]

$$\int_{\Omega}\left(\rho\frac{\partial^2\underline{u}}{\partial t^2}\right)\cdot\underline{\eta}d\Omega+\int_{\Omega}\nabla\underline{\eta}\cdot\left(\underline{\underline{\underline{C}}}\left[\frac{1}{2}\left(\nabla\underline{u}+\left(\nabla\underline{u}\right)^T\right)\right]\right)d\Omega+\int_{\Omega}\nabla\cdot\underline{\underline{\underline{C}}}\left(\underline{\underline{\underline{\lambda}}}^m\underline{m}\underline{m}^T\right)\underline{\eta}d\Omega=\int_S\underline{\eta}\cdot\underline{\underline{\underline{C}}}\left[\frac{1}{2}\left(\nabla\underline{u}+\left(\nabla\underline{u}\right)^T\right)\right]\cdot ndS \tag{2-22}$$

with prescribed displacements and prescribed tractions on boundaries,

$$\begin{aligned}&\underline{u}=\underline{u}^0 && \text{on } S_1\\ &\underline{\underline{\underline{\sigma}}}\cdot\hat{n}=\underline{t} && \text{on } S_2\end{aligned} \tag{2-23}$$

where S_1 and S_2 are sub-boundaries on S ($S_1 \cup S_2 = S$).

Finally, to construct the weak form of Eq. (2-19), we multiply the test vector functions $\underline{\psi}$ and integrate over the volume Ω. After integrating $\underline{H}_{ex}$ by parts, the weak form is [100]

$$\int_\Omega \left(\frac{\partial \underline{m}}{\partial t} - \alpha \left(\underline{m} \times \frac{\partial \underline{m}}{\partial t} \right) \right) \cdot \underline{\psi} d\Omega =$$

$$-\int_\Omega \mu_0 \gamma \left(\underline{m} \times \left(\underline{H}_{ext} + \underline{H}_d + \underline{H}_{anis} + \underline{H}_{me} \right) \right) \cdot \underline{\psi} d\Omega + \frac{2A_{ex}\gamma}{M_s} \sum_l \int_\Omega \left(\underline{m} \times \frac{\partial \underline{m}}{\partial x_l} \right) \cdot \frac{\partial \psi_l}{\partial x_l} d\Omega \qquad (2\text{-}24)$$

with the boundary condition

$$\frac{\partial \underline{m}}{\partial n} = 0 \qquad \text{on } S \qquad (2\text{-}25)$$

and subject to the constraint by definition

$$|\underline{m}| = 1 \qquad \text{on } \Omega \qquad (2\text{-}26)$$

Equations (2-20), (2-22), and (2-24) are subject to the boundary conditions given in Eqs. (2-21), (2-23), and (2-25), representing a well-posed problem that can be solved using finite element methods.

2.3 Simulation

The weak forms of Eqs. (2-20), (2-22), and (2-24) [99][100][101] are solved using finite element methods with an implicit time stepping scheme and the backward differentiation formula (BDF)[102]. In order to decrease solution time, the system of equations with ϕ, $\underline{m}$, $\underline{u}$ is solved using a segregated solution approach, which splits the solution process into substeps using a damped Newton's method[102]. In this chapter we have implemented the mathematical model (see flowchart in Figure 2-1) in a commercially available partial differential equation solver COMSOL (i.e. commercial code has graphical user interfaces) [102]. In general, as shown in Figure 2-1, initial conditions are first applied followed by a Newton iteration approach to converge for a given time step. Once converged, the time step is advanced and the process is repeated. The mathematical model described in this chapter can be similarly implemented in other finite element or numerical analysis packages that provide platforms to solve partial differential equations. For all numerical problems, convergent studies (i.e., mesh size and time steps) were conducted to ensure accuracy. The model was validated by comparing with experimental data.

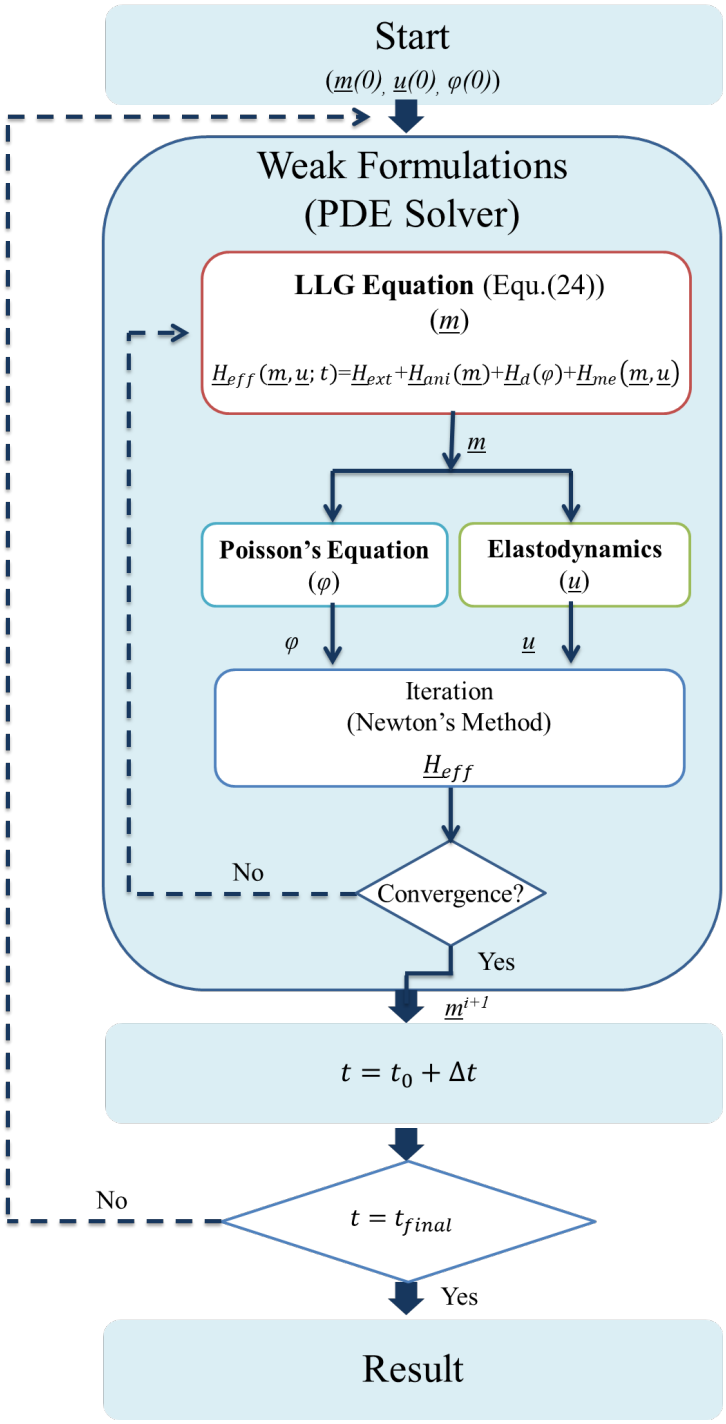

Figure 2-1 (Color) Flowchart of the fully-coupled FEM simulation.

Experimental tests have been previously conducted by Bur et al.[36] on 100 nm × 300 nm × 35 nm nickel nanostructures attached to a SiO_2 substrate subjected to mechanical loads. In their study, the change of the M vs. H curve as a response to applied mechanical loads was reported. An illustration of the finite element model used to analyze the experimental data is shown in Figure 2-2(a). The nickel nanostructure was assumed to be perfectly bonded to the substrate. The structure shown in Figure 2-2(a) is discretized using tetrahedral elements with a size on the order of nickel's exchange length. The nickel properties used were[24][97][102] $M_s = 4.8\times10^5 (A/m)$; $A_{ex} = 1.05\times10^{-11}(J/m)$; $\lambda_{100} = -46\times10^{-6}$, $\lambda_{111} = -24\times10^{-6}$, $c_{11} = 2.5\times10^{11}(N/m^2)$, $c_{12} = 1.6\times10^{11}(N/m^2)$, and $c_{44} = 1.18\times10^{11}(N/m^2)$. The exchange length, defined as $\sqrt{\frac{2A}{\mu_0 M_s^2}}$, is 8.5 nm for nickel. The Gilbert damping constant was set as $\alpha = 0.5$ to improve stability and process time. The Young's modulus and Poisson's ratio of the isotropic substrate (SiO_2) used were $E_{SiO_2} = 70(Gpa)$ and $\upsilon = 0.2$, respectively.

Figure 2-2(b) illustrates the magnetic field direction and boundary conditions. The external magnetic field was applied along the y-direction. Displacements were applied on the SiO_2 boundaries at x=1000 nm and y=1000 nm to induce relative strains ($\varepsilon_{yy} - \varepsilon_{xx}$) of -1210, -671, 260, 0, 235, 645, and 1060 $\mu\varepsilon$, where $\varepsilon_{xx} = -\nu\varepsilon_{yy}$ in the effective substrate. Roller conditions were used along the planes at x=0 and y=0. The displacement conditions were initially applied and the magnetization states for all elements were allowed to reach equilibrium. Subsequently, an external magnetic field (H_{ext}) was first varied from 0 to 1250 Oe followed by a reduction to -1250 Oe and finally back to 0 Oe. In the applied field region of -750~-250 Oe and 250~750 Oe which represents values near the coercive field H_c, the field values were

incremented by 15 Oe while for all other field regions the increments were 250 Oe. The magnetization of the nickel nanostructure in the y direction at each applied field was determined by volume averaging the y-component of magnetization throughout the Ni nanostructure.

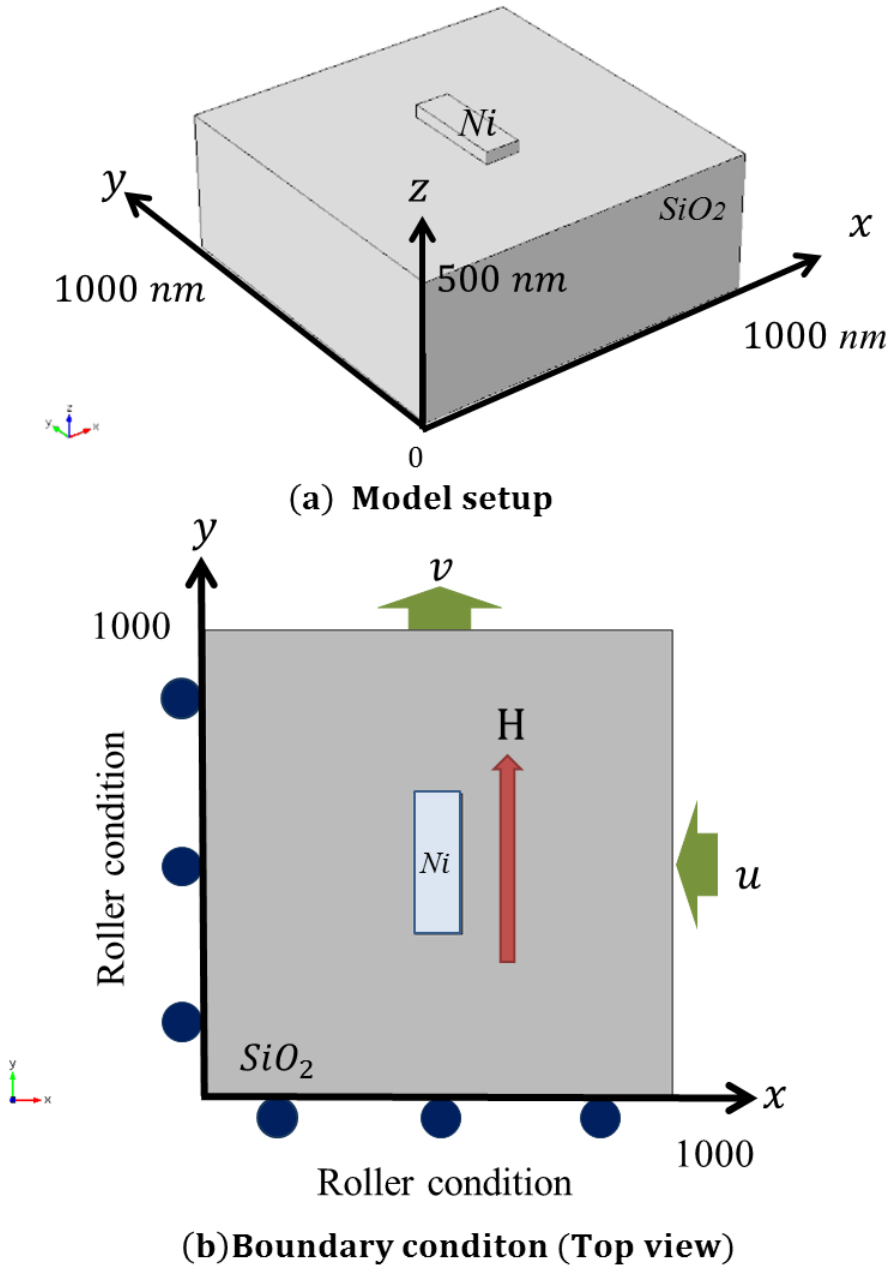

Figure 2-2 (Color) Schematic diagram of the model and boundary conditions.

2.4 Results and Discussion

In this section, experimental data[36] is compared to three different analytical models. The three models are the SW model[10][98], assuming cooperative spin and constant strain; the LLG micromagnetic model assuming spatially (homogeneous) uniform strain (ε=constant) [25][76][77] and the proposed model of LLG with equations of elastodynamics (LLG/EQ) derived in the analytical section of this document. This section makes use of the term "magnetostrictive strain" to describe the local strain experienced by the magnetic nanostructure as a response to the applied displacement (i.e. effective $\varepsilon_{yy} - \varepsilon_{xx}$ in the substrate). The following paragraphs provide results for strain distribution, magnetic hysteresis curves, coercive field values, and magnetostrictive strains as a function of magnetic field.

In Figure 2-3, experimental results and analytical results for the volume-averaged normalized magnetization M vs. applied H in the nickel nanostructure are plotted for the SW model, the LLG model, and the LLG/EQ model. Each figure is evaluated for seven different applied displacements/strains ($\varepsilon_{yy} - \varepsilon_{xx}$). In general, the area of all three hysteresis predictions (including experiments) decreases as the applied strains ($\varepsilon_{yy} - \varepsilon_{xx}$) increase. This trend is expected since nickel is a negative magnetostrictive material. The SW model is a single-domain/spin model to approximate M vs. H hysteresis curves and describe basic micromagnetic phenomena. As can be seen in Figure 2-3(b), the SW model does not accurately predict the experimental results depicted in Figure 2-3 (a)[36]. The SW hysteresis area is much larger than the experimental data (i.e. over 50% larger than experimental results). In addition, SW predicts sharp coercive field changes while experiments are considerably smoother near coercive fields. The LLG model and the LLG/EQ model provide much closer approximations to experimental

data when compared to SW. The LLG hysteresis curves are different than those from the LLG/EQ model with non-uniform strains, as shown in Figure 2-3 (c) and Figure 2-3 (d). This is because the LLG model assumes constant strains and increases the amount of magnetoelastic energy input to the Ni nanostructures. In general, the SW model for coherent spin behavior and the LLG model have significant disagreement with the experimental results, which cannot be used to design more complicated magnetic nanostructures, while the LLG/EQ model curves provides more accurate predictive results.

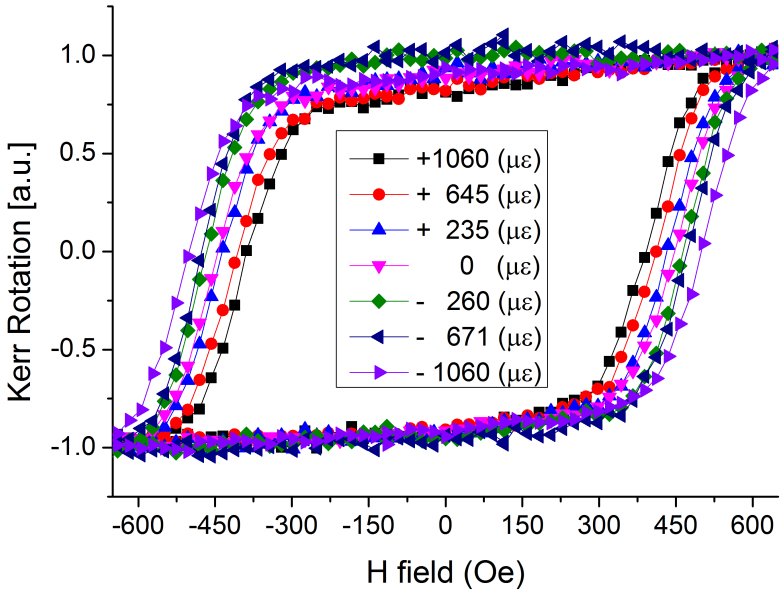
Kerr Rotation [a.u.]
1.0
0.5
0.0
-0.5
-1.0
-600
-450
-300
-150
0
150
300
450
600
H field (Oe)
+1060 (με)
+ 645 (με)
+ 235 (με)
0 (με)
- 260 (με)
- 671 (με)
- 1060 (με)

(a)

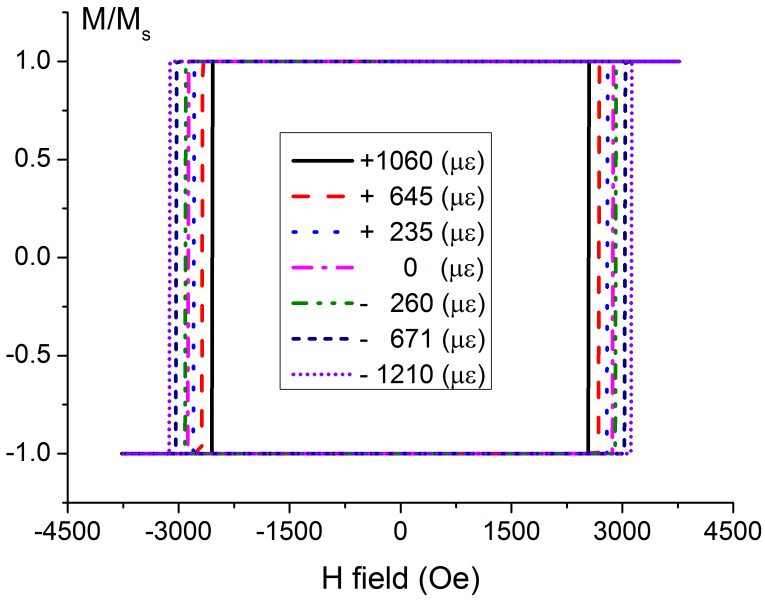
M/M$_s$
1.0
0.5
0.0
-0.5
-1.0
-4500
-3000
-1500
0
1500
3000
4500
H field (Oe)
+1060 (με)
+ 645 (με)
+ 235 (με)
0 (με)
- 260 (με)
- 671 (με)
- 1210 (με)

(b)

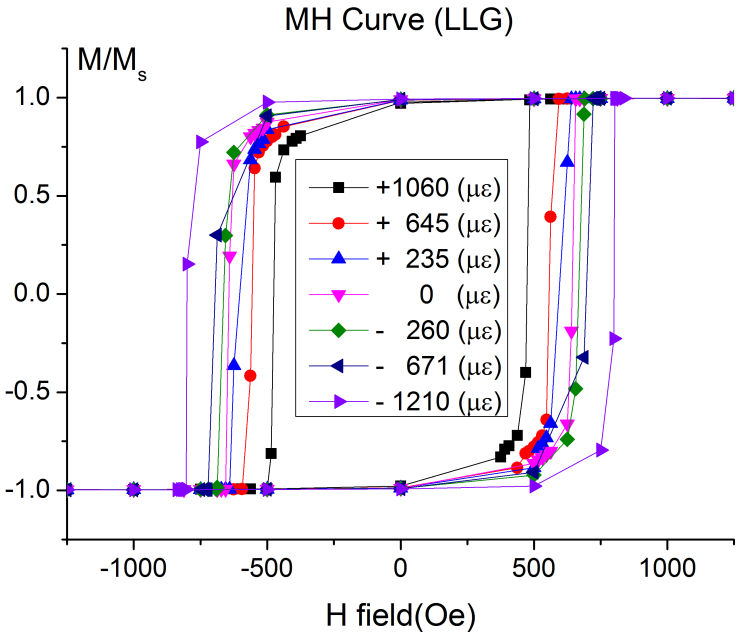

(c)

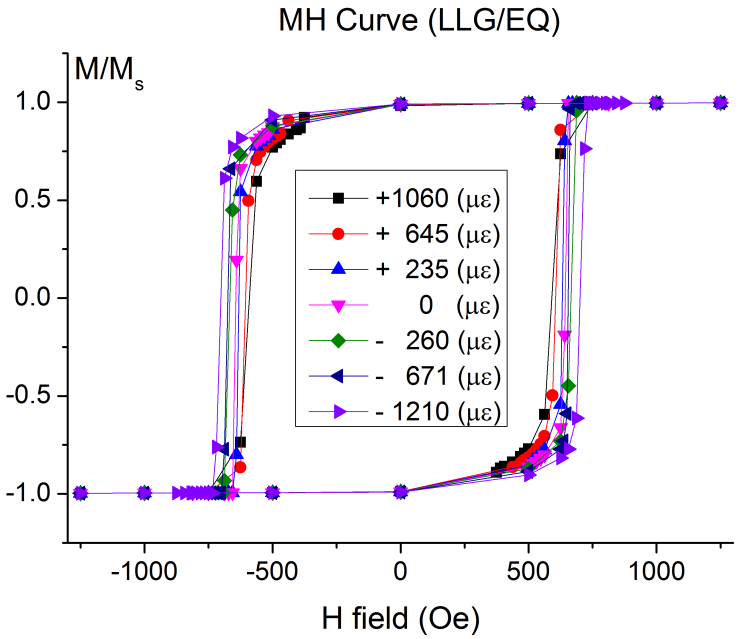

(d)

Figure 2-3 (Color) Hysteresis curves of external fields acting on the 100 nm × 300 nm × 35 nm Ni nanostructure generated using (a) experimental data (longitudinal MOKE), (b)

Stoner-Wolhfarth (SW) model, (c) LLG, and (d) LLG/EQ models for comparison, using volume-averaged values. The SW model displays impractically sharp hysteretic behavior due to its perfectly spin-oriented single domain assumption, and both the SW and traditional LLG models clearly show coercivity overestimation when compared to experimental data.

Figure 2-4(a) compares the coercive fields H_c as a function of applied strain ($\varepsilon_{yy} - \varepsilon_{xx}$) for the SW model, the LLG model, the LLG/EQ model, and the experimental data. All curves show both a relatively linear relationship between H_c and the applied strains ($\varepsilon_{yy} - \varepsilon_{xx}$) with a decreasing H_c as the applied relative strain ($\varepsilon_{yy} - \varepsilon_{xx}$) increases. The SW model shows significant disagreement with the experimental data by as much as 2350 Oe, while the LLG model and LLG/EQ model results have relatively better agreement but still differing by as much as 200 Oe. Such inconsistencies in the analytical results are attributed to thermal issues, surface roughness, aspect ratio, or geometric smoothing in the nanostructure, which are not adequately represented in the simulations. In Figure 2-4(b), the change in coercive field values (i.e., $\Delta H_c = H_c - H_c^0$) for the SW model ($\Delta H_c = 3\lambda_s E\left(\varepsilon_{yy} - \varepsilon_{xx}\right)/M_s$), the LLG model, the LLG/EQ model, and experiments are provided. The LLG/EQ model shows very good agreement with experiment data (less than 2% deviation) while the SW model and the LLG model both relatively poor agreement with errors as large as 60%. These set of comparisons clearly indicate that non-uniform strain distributions must be considered when predicting and understanding the strain-mediated magnetic anisotropic effect in nanostructures. Therefore, caution should be taken when using SW or LLG simulations in these finite size structures.

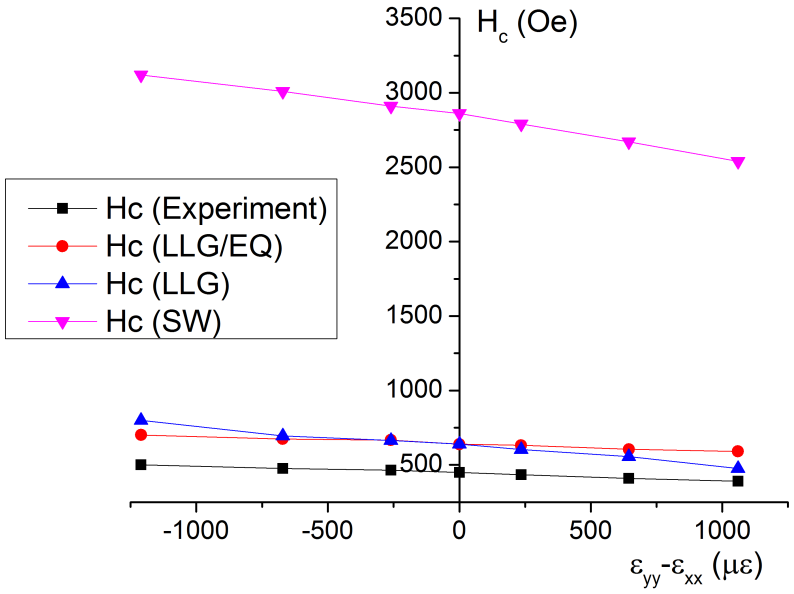

(a)

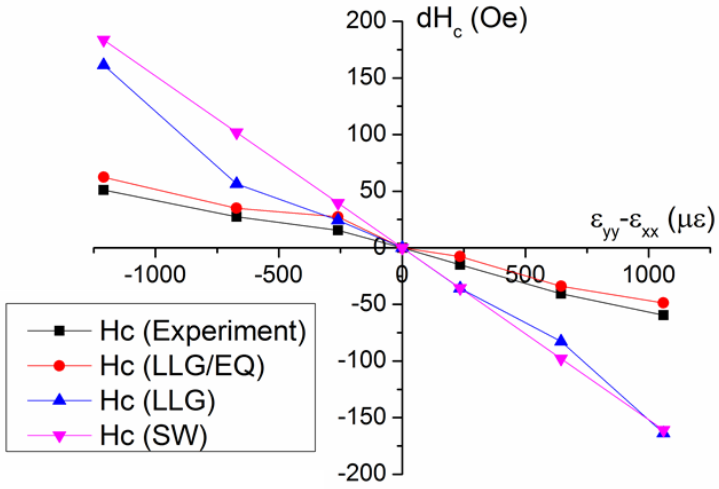

(b)

Figure 2-4 (Color) Comparison of experimental values with LLG/EQ, LLG, and Stoner-Wohlfarth models for (a) coercive field H_c and coercive difference ΔH_c, as a function of $\varepsilon_{yy} - \varepsilon_{xx}$ (b).

Figure 2-5 shows analytical LLG/EQ results of the relative strain distribution in the Ni nanostructure with an effective applied strain $\varepsilon_{yy} - \varepsilon_{xx} = -671\mu\varepsilon$ and zero applied magnetic field. Figure 2-5(a) shows the surface plot for strains ($\varepsilon_{yy} - \varepsilon_{xx} = -671\mu\varepsilon$) in the nickel nanostructure. The simulation results clearly show that the strain distribution is non-uniform throughout the nanostructure. The relative strain values vary substantially between $-700\mu\varepsilon$ and $-80\mu\varepsilon$. Figure 2-5(b) plots the relative strain ($\varepsilon_{yy} - \varepsilon_{xx}$) as a function of *y* at *x* = 50 nm for four different *z* values. Large strain variations are observed near the nanostructure ends (*y* = 0 nm and *y* = 300 nm), while the strain in the middle (*y* = 150 nm) is relatively uniform. The volume-averaged strain $\varepsilon_{yy} - \varepsilon_{xx}$ for the nickel nanostructure is $-322\mu\varepsilon$ and is 50% less than the applied strain. The strain variation as a function of position occurs due to a well-known phenomenon, classically referred to as shear lag in the mechanics community. Therefore, one can clearly see that the assumption of constant strain present in SW and LLG is inappropriate for this structure.

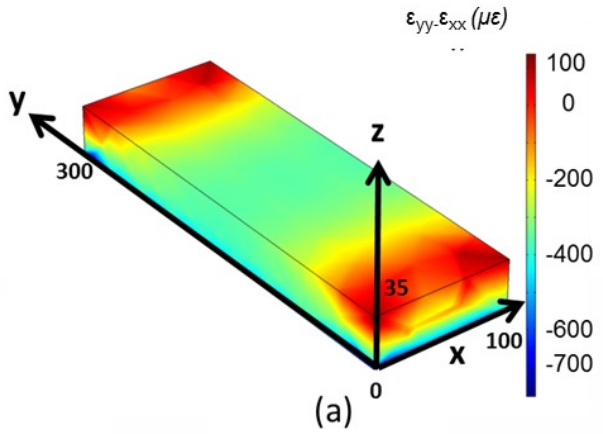

(a)

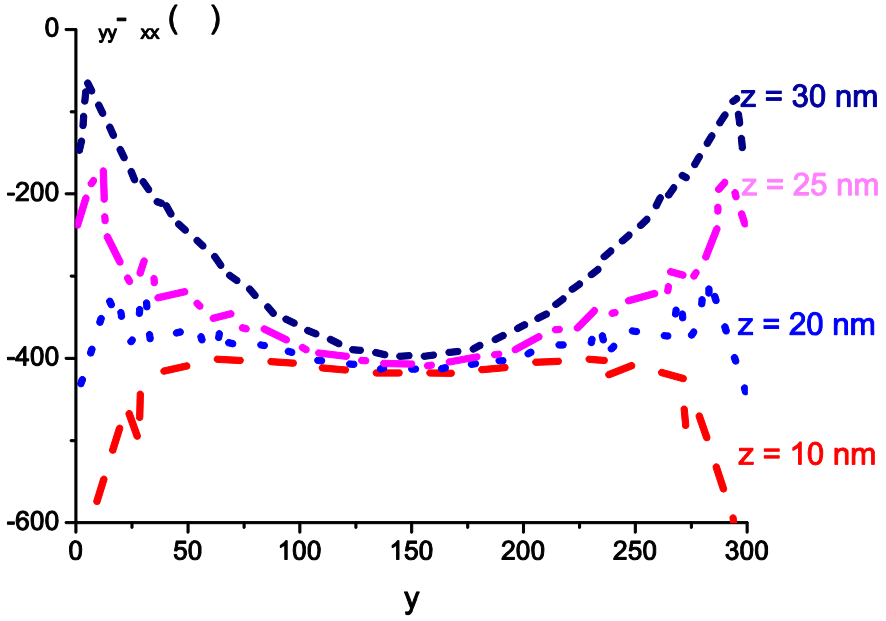

(b)

Figure 2-5 (Color) The non-uniform relative strain distributions in a 100 nm × 300 nm × 35 nm Ni nanostructure subjected to a strain of $\varepsilon_{yy} - \varepsilon_{xx} = -671\mu\varepsilon$, expressed as a surface plot of the non-uniform strain distribution in the nickel nanostructure (a) and relative strain $\varepsilon_{yy} - \varepsilon_{xx}$ as a function of *y* at different *z* values and *x* = 50 nm (b).

The LLG/EQ model is also able to predict the influence of magnetic field on magnetostrictive output strains which once again requires a fully coupled solution to accurately represent the response of a nanoscale structure. Figure 2-6 shows analytical results for the normalized magnetization M vs. applied H along the geometric hard y-axis (along the short width of the nanostructure) with an applied $\varepsilon_{yy} - \varepsilon_{xx} = -1210\mu\varepsilon$. Figure 2-6 shows the spin states and the surface strain plots for the magnetostrictive strain ($\varepsilon_{11}^{m} = \frac{3}{2}\lambda_{100}\left(m_1^2 - \frac{1}{3}\right)$) under different applied H in the *y*-axis. The complete hysteresis loop follows a chronological number sequence ($1 \rightarrow 5$) as shown in Figure 2-6. The hysteresis loop begins at point 1 with zero applied field. When the applied field increases, the magnetization increases, saturating when the applied field is ~937 Oe (point 2). When the applied field is reversed, the normalized magnetization decreases to 0.1 at H = 0. The normalized magnetization is nonzero because remnant magnetic spins persist along the hard geometric axis of the nickel nanostructure. As the applied field becomes negative, the magnetization response asymmetrically mirrors the positive H as expected. Figure 2-7 plots magnetic spin states under the five applied fields (points 2 to 5) indicated in Figure 2-6. Without an applied field, the spins point along the geometric easy axis of the nanostructure. When a sufficiently large positive or negative field is applied along the *x*-axis, the spins form a flower state, fanning out along the *x*-axis to accommodate the demagnetization effect at the corners. Figure 2-7 shows the magnetostrictive strain (ε_{11}^{m}) distribution in the nickel nanostructure. When the applied field is zero, the magnetostrictive strain (ε_{11}^{m}) is fairly uniformly distributed through the nanostructure. When the applied field is large, the magnetostrictive strain (ε_{11}^{m}) is large in the middle of the nanostructure and is small at the corners, once again showing that constant strain assumptions are invalid.

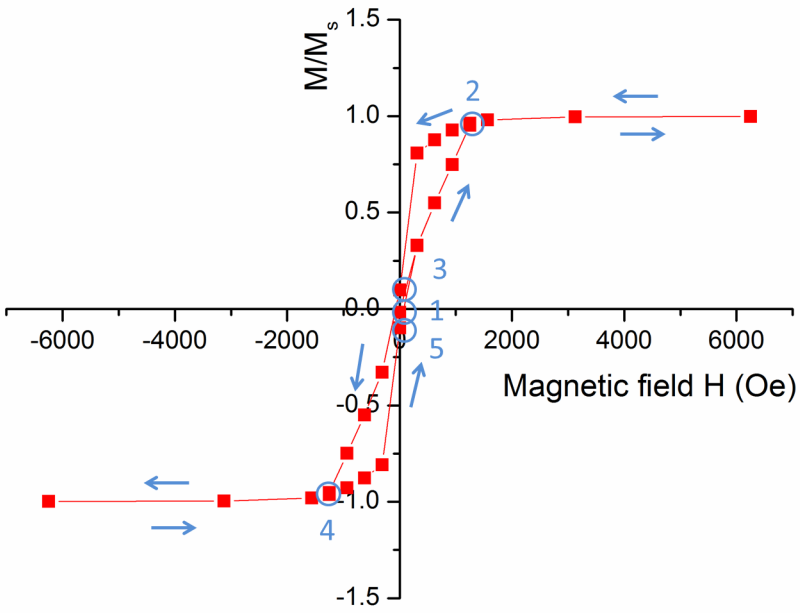

Figure 2-6 (Color) Hysteresis along the y-axis (y-axis) of the nanostructure under -1210 $\mu\varepsilon$.

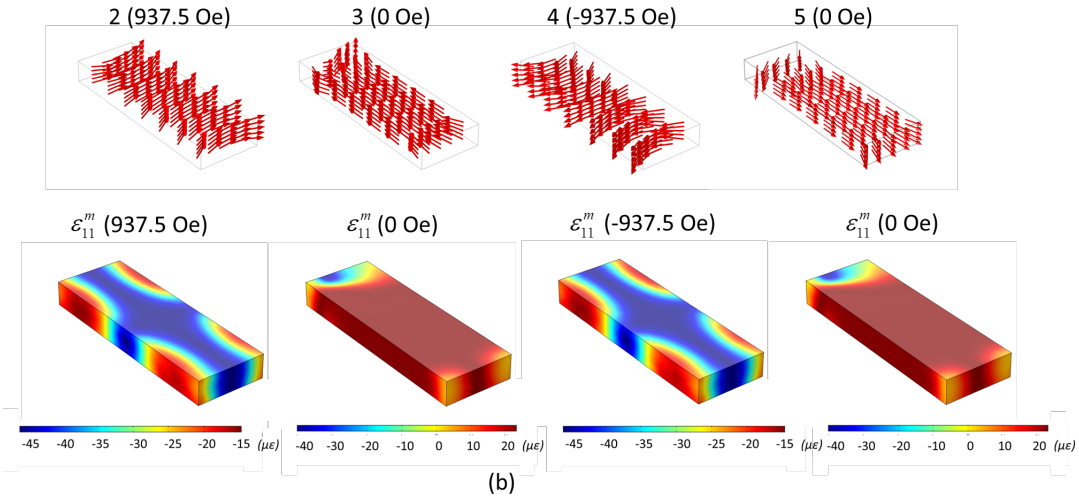

Figure 2-7 (Color) Spin states corresponding to hysteresis points in Figure 5 (top) and illustration of magnetostrictive strain (ε_{11}^m) in the nanostructure (bottom).

Figure 2-8 shows four ($\varepsilon_{22}^{m} = \frac{3}{2}\lambda_{100}\left(m_2^2 - \frac{1}{3}\right)$) magnetostrictive strain states and their corresponding applied field results for nickel nanostructure. As shown in Figure 2-8(a), the complete magnetization loop follows a chronological sequence ($1 \rightarrow 12$). Without the application of a magnetic field (point 1), the spin state is a single domain aligned along the long axis of the structure. The spins are uniformly pointing along the *y*-axis at the center of the nanostructure, which then fan outwards along the nanostructure toward the corners due to demagnetization effects. The magnetostrictive strain is $-44\mu\varepsilon$ in this initial state. When the magnetic field increases ($1 \rightarrow 3$), the spins at the corners are forced to saturate along the easy axis, and the magnetostrictive strain decreases to $-46\mu\varepsilon$. When reversing the magnetic field ($3 \rightarrow 7$) to -560 Oe, there is a peak showing that the spin state forms an ordered 'S' shaped state within the structure. This is the critical field strength where the spins begin flipping to the opposite direction. The magnetostrictive strain is approximately $-10\mu\varepsilon$ in this state. As the field decreases ($7 \rightarrow 9$), the spins begin pointing along the negative *y*-axis. This presentation illustrates the complex states that the magnetic spins take and are strongly influenced by finite size or shear lag effects in the nanostructure, i.e. inhomogeneous strains.

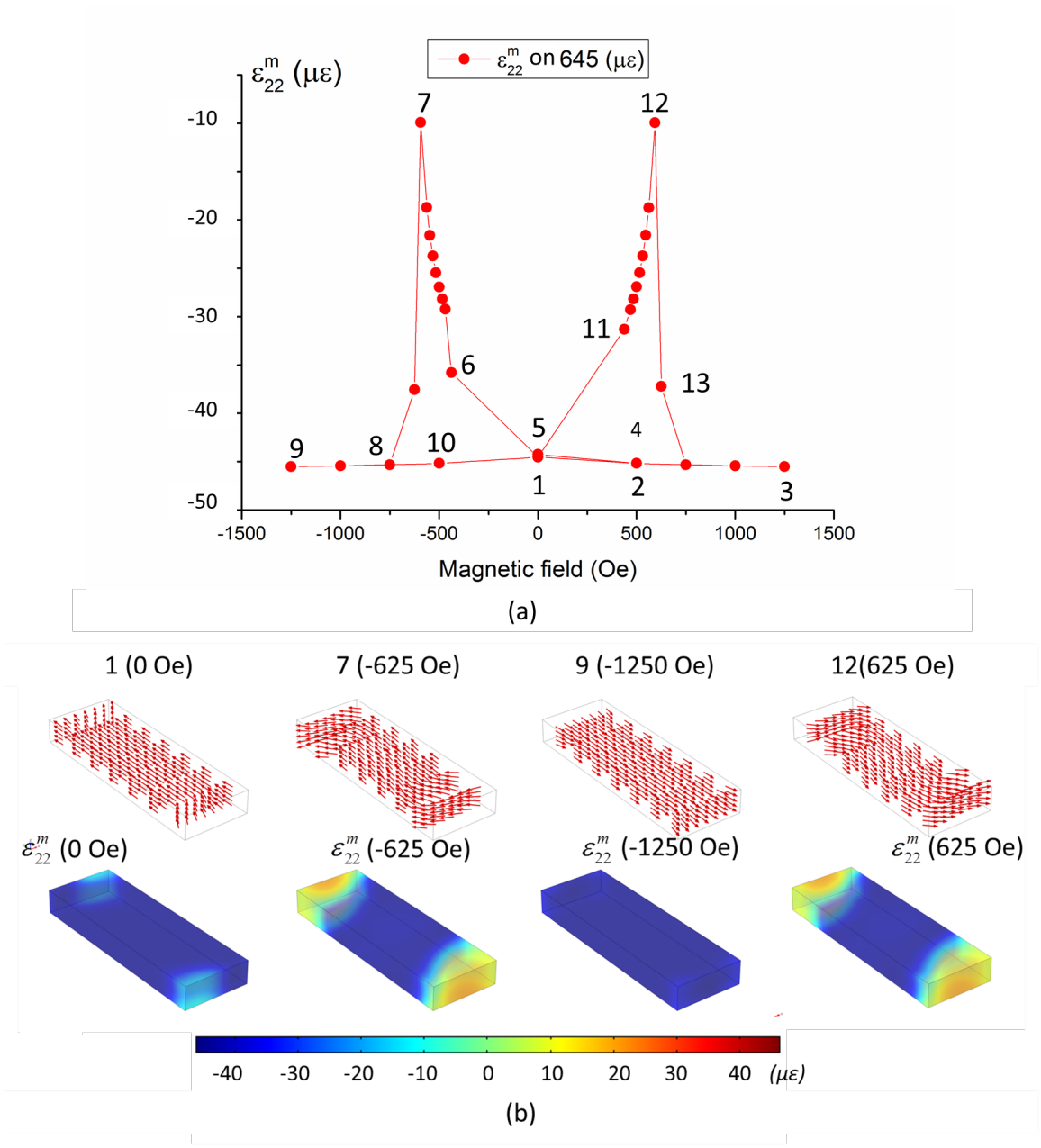

Figure 2-8 (Color) Magnetostrictive strain (vs.) applied magnetic fields (a), and nanostructure spin state at four distinct points of the graph (b, top) and their corresponding magnetostrictive strain states (b, bottom).

In conclusion, we have developed a numerical approach based on finite element for simulating magnetization states, magnetic hysteresis curves, and strain-induced coercive field changes in magnetic nanostructures by coupling the spatially-dependent strain state with micromagnetic simulation (LLG/EQ model) with elastodynamics. This model provides substantially better predictive results than the LLG model and the conventional Stoner-Wohlfarth (SW) model and in some cases must be used to accurately predict the response of a nanoscale structure. The LLG/EQ coupled model was verified with existing experimental data validating its predictive capabilities. In general, this work strongly encourages researchers to use coupled solutions when modeling the magnetoelastic response of finite size structures to accurately predict the magnetoelastic response. This is important in a wide range of fields, including memory, motors, and spin wave propagation.

3. Electrical Control of a Single Magnetoelastic Domain Structure on a Clamped Piezoelectric Thin Film – Analysis

This chapter presents an analytical model coupling Landau-Lifshitz-Gilbert micromagnetics with elastodynamics and electrostatics to model the response of a single domain magnetoelastic nano-element attached to a piezoelectric thin film (500 nm). The thin film piezoelectric is mounted on a Si substrate, globally clamping the film from in-plane extension or contraction. Local strain transfer to the magnetoelastic element is achieved using patterned electrodes. The system of equations is reduced to eight coupled partial differential equations as a function of voltage (V), magnetic potential ϕ, magnetic moments ($\underline{m}$), and displacements ($\underline{u}$), i.e. fully coupled material. The weak forms of the partial differential equations are solved using a finite element formulation. The problem of a Ni single domain structure (i.e. 150nm x 120nm x 10 nm) on a thin film (500nm) PZT-5H attached to an infinite substrate is studied. Discretization in the single domain structure is on the order of the exchange length (8.5nm), providing spatial and temporal information on the local mechanical and magnetic fields. A -0.5 V potential is applied to a pair of surface electrodes, producing out-of-plane deformation and in turn straining the magnetoelastic single domain nanostructure in-plane. This strain is sufficient to reorient a single domain structure representative of an idealized memory element.

3.1 Introduction and Background

For the past decade, researchers have focused on developing a magnetic memory element using a multiferroic material[103]. One approach uses a strain-mediated composite approach consisting of layered piezoelectric and magnetoelastic materials strain coupled together[42][104][105]. Researchers have analytically shown that the energy required to reorient/write a single magnetic domain structure can be very small, i.e. considerably smaller than conventional approaches to writing bits of memory[45][87][106][107]. However, the multiferroic composite memory element is typically fabricated on a fairly thick substrate system, e.g. silicon. This thick substrate clamps the piezoelectric/magnetoelastic material, limiting the amount of strain that can be generated, posing a significant challenge for the implementation of a strain-mediated memory element. In this analytical work we demonstrate a concept to overcome the substrate clamping issue and show reorientation of a magnetic single domain between two stable states by simply pulsing the voltage.

Previous researchers have demonstrated the control of the magnetization states in thin film magnetoelastic material deposited on a thick piezoelectric substrate[53][54] [108][109][110]. This effect has been used to alter magnetic domains [42][53][54] [104] and to shift the magnetic coercive field[109][110]. As an alternative to using in-plane polarized piezoelectric material, some researchers such as Wu used the auxetic piezoelectric strain produced by [011] cut PMN-PT, while others have used the same effect in PZN-PT single crystals[111][112]. These single crystal approaches resulted in a proposed design of a magnetoelectric memory system, but once again still required bulk piezoelectric material[73][87]. Moutis et al. in 2008 reported electric-field modulation of coercive field H_c using periodic arrays of ferromagnetic (FM) $Co_{50}Fe_{50}$

stripes[51]. Bur et al. in 2011 reported strain-induced coercive field changes in patterned single-domain nickel nanostructures deposited on a thick Si/SiO_2 substrate using external mechanical loads[36], while Nan et al. suggested single domain reorientation on bulk PMN-PT single crystal[87]. Regarding piezoelectric materials deposited onto a substrate, out-of-plane magnetic reorientation has been achieved with magnetic BFO/CFO vertical nanoscale structures embedded in a ferroelectric thin film, as described by Zavaliche et al. in 2005[49], but this approach is non-deterministic. Chung et al. studied single domain elements on a thin film piezoelectric[53][54], but did not demonstrate reorientation of the magnetic domain. None of these studies provides an acceptable approach to reorient a single domain structure deterministically using strain-mediated approach on a constrained substrate.

The development of a strain-mediated multiferroic memory device requires the magnetization of each element to be individually controllable using a ferroelectric thin film grown on a substrate (e.g. Si wafer). The problem with this concept it that the thin film piezoelectric is clamped by the thick substrate and prevents strain transfer. Cui et al. suggested the use of patterned electrodes to overcome substrate clamping and obtain highly localized strain in both the thin film piezoelectric and the magnetic material[113]. The general concept was demonstrated on a bulk piezoelectric ceramic, but did not include detailed analysis (or experiments) for a thin film piezoelectric.

The analysis of single domain switchable magnetoelectric heterostructures requires the use of the Landau-Lifshitz-Gilbert LLG micromagnetic approaches developed in the 1950s[24][25]. An important addition to micromagnetics was the inclusion of strain (or stress) for magnetostrictive materials by Zhu et al. in 2001[30]. This was used by Hu in 2006 to model the effect of stress on hysteresis curves and magnetization dynamics, showing the interaction of

stress with coercivity and the easy axis of magnetoelastic materials[34]. Building on these advancements, Hu et al. used stability conditions and proposed an electric field read and write MERAM device[106]. A balance of both shape and strain anisotropy was used to describe an elliptical nanomagnet that could be switched under stress by Roy et al[45]. In most of these studies, however, magnetization and strain were assumed to be spatially homogeneous and thus the clamping issues produced by the substrate were not addressed. D'Souza et al. in 2011 proposed and analyzed a low-power 4-state universal logic gate using a linear array of multiferroic nanomagnets[114], but did not consider the substrate clamping issue. Tiercelin et al. described and analyzed a magnetoelectric memory cell that balanced strain anisotropy, shape anisotropy, and a bias field[107]. In this later work the elastic contribution was modeled separately and the piezoelectric film was not attached to a substrate.

In this chapter, a single domain magnetoelastic elliptical nanostructure deposited onto a thin film piezoelectric wafer attached to a thick substrate is modeled by coupling micromagnetics (LLG), elastodynamic, and electrostatics partial differential equations. The nickel magnetoelastic ellipse (150 nm x 120 nm x 10 nm) has shape anisotropy and an applied magnetic field along the minor axis to shift the energy wells, as described originally by Tiercelin in 2011[107]. The thin film (500 nm) piezoelectric is attached to a thick substrate that clamps and prevents relative in-plane motion of the piezoelectric at the interface of the film with the substrate. Four electrodes are placed around the Ni magnetoelastic element similar to Tiercelin[107]; however, these electrodes produce out-of-plane electric fields rather than in-plane electric fields[113], and the thin film is mounted onto a substrate. The intrinsic coupling of the piezoelectric response with the magnetoelastic response through strain is modeled by coupled partial differential equations (i.e. electrostatics tied to micromagnetics while solving elastodynamics). The numerical

formulation uses tetrahedral finite elements with a maximum size equal to the exchange length of nickel (~8.5 nm), providing spatially varying strains, electric fields, and magnetic spins throughout the structure. Therefore, the model captures all the relevant physics required to accurately predict the response of this multiferroic nanoscale structure and demonstrates single domain magnetic reorientation in a strain-mediated structure attached to a thick clamped substrate.

3.2 Theory for Computational Model

Strain-mediated multiferroic composites consist of both piezoelectric and magnetoelastic materials. Thus, the fundamental governing equations for predicting the dynamic response are based on electrostatics, micromagnetics (LLG), and elastodynamics. In this chapter, the general governing equations for a strain-mediated electro-mechanical and magnetoelastic materials are derived as in the previous chapter, from which individual phases represent limiting cases. The following derivation presents a general approach for developing the governing equations in weak forms, which are then implemented into a finite element formulation. Assumptions include small elastic deformations, linear elasticity, linear piezoelectricity, electrostatics, and negligible electrical current contributions. The single general derivation presented can be subsequently decoupled to predict the response of an electro-mechanical or magnetoelastic material.

The strain for a multiferroic (magneto-electric-elastic) material is given by

$$\underline{\underline{\varepsilon}} = \underline{\underline{\varepsilon}}^{el} + \underline{\underline{\varepsilon}}^{PE} + \underline{\underline{\varepsilon}}^{m}\left(\underline{m}\right) \tag{3-1}$$

where $\underline{\underline{\varepsilon}}$ is the total strain with contributions from the elastic strain $\underline{\underline{\varepsilon}}^{el} = \underline{\underline{\underline{\underline{C}}}}^{-1}\underline{\underline{\sigma}}$, the piezoelectric strain $\underline{\underline{\varepsilon}}^{PE} = \underline{\underline{\underline{d}}}\,\underline{E}$, and the magnetostriction strain $\underline{\underline{\varepsilon}}^{m} = \underline{\underline{\underline{\underline{\lambda}}}}^{m}\,\underline{m}\underline{m}^{T}$. Here $\underline{\underline{\underline{\underline{C}}}}$ is the elastic stiffness tensor, $\underline{\underline{\sigma}}$ is the stress tensor, $\underline{\underline{\underline{d}}}$ is the piezoelectric strain tensor, $\underline{E}$ is the electric field vector, $\underline{\underline{\underline{\underline{\lambda}}}}$ is the magneto-mechanical coupling tensor, and $\underline{m} = \frac{M}{M_s}$ is the normalized local magnetization vector with M_s representing saturation magnetization. For a cubic crystal, the components of $\underline{\underline{\varepsilon}}^{m}$ in a cubic referenced coordinate system are given by

$$\varepsilon_{ij}^{m} = \begin{cases} \frac{3}{2}\lambda_{100}\left(m_i m_j - \frac{1}{3}\right) & i = j \\ \frac{3}{2}\lambda_{111} m_i m_j & i \neq j \end{cases} \tag{3-2}$$

where λ_{100} and λ_{111} are magnetostriction constants along the $\langle 100 \rangle$ and $\langle 111 \rangle$ directions[25][31][32][33][97][115]. For hexagonal or uniaxial crystals, equation (3-2) would have a different form that can easily be implemented in the approach[97], and for an isotropic polycrystalline the two coefficients have the same value.

The electrical portion of the constitutive equation, assuming negligible magnetic and electric field coupling, is given by

$$\underline{D} = \underline{\underline{d}}^{T} \underline{\underline{\sigma}} + \underline{\underline{\varepsilon}}_s \underline{E} \tag{3-3}$$

where $\underline{\underline{\varepsilon}}_s$ is the dielectric tensor and $\underline{D}$ is the electric displacement. For a general multiferroic material, an additional term would appear in equation (3-3) representing the coupling between magnetic and electric fields, but for this derivation we have assumed this component is negligible. The coupling between magnetic and electric fields in the material modeled in this chapter arises due to the stress term in equation (3-3) and its coupling to magnetic strain presented in equation (3-1). The electrostatic governing equations are

$$\begin{aligned} \nabla \cdot \underline{D} &= \rho_f \\ \underline{E} &= -\nabla V \end{aligned} \tag{3-4}$$

where V is the electric potential and ρ_f is density of free charges. The electric potential V is obtained by combining equations (3-3) and (3-4) for electrostatic behavior ($\rho_f = 0$):

$$\nabla \cdot \left[\underline{\underline{d}}^{T} \underline{\underline{\sigma}} + \varepsilon_s \left(-\nabla V \right) \right] = 0 \tag{3-5}$$

The magnetic response of the multiferroic media is governed by the phenomenological Landau-Lifshitz-Gilbert (LLG) micromagnetic relation[25]

$$\frac{\partial \underline{m}}{\partial t} = -\mu_0 \gamma \left(\underline{m} \times \underline{H}_{eff} \right) + \alpha \left(\underline{m} \times \frac{\partial \underline{m}}{\partial t} \right) \tag{3-6}$$

where μ_0 is the permeability in the vacuum, γ is the Gilbert gyromagnetic ratio, and α is the Gilbert damping constant. $\underline{H}^{eff}$ is the effective magnetic field, which is obtained from the total energy density and is given by[24][25]

$$\underline{H}_{eff} = -\frac{1}{\mu_0 M_S} \frac{\partial E_{tot}}{\partial \underline{m}} = \underline{H}_{ext} + \underline{H}_{ex} + \underline{H}_{anis} + \underline{H}_{d} + \underline{H}_{me} \left(\underline{m}, \underline{u}(\underline{E}) \right) \tag{3-7}$$

where E_{tot} is the total energy density, which includes the Zeeman energy density due to an applied external field, the exchange energy density, the magnetocrystalline anisotropy energy density, the demagnetization energy density, and the elastic energy density[25][31][32]. $\underline{H}_{ext}$ is the applied external field, $\underline{H}_{ex}$ is the exchange field, $\underline{H}_{anis}$ is the anisotropic field, $\underline{H}_{d}$ is the demagnetization field and $\underline{H}_{me}$ is the magnetoelastic field. Expressions for these terms follow

$$\underline{H}_{ex} = \frac{2A_{ex}}{\mu_0 M_s} \nabla^2 \underline{m} \tag{3-8.1}$$

$$H^{i}_{anis} = -\frac{2m_i}{\mu_0 M_S} \left[K_1 \left(m_j^2 + m_k^2 \right) + K_2 \left(m_j^2 m_k^2 \right) \right] \tag{3-8.2}$$

where K_1 and K_2 are cubic anisotropy constants[25][31][32][33]. The equation for the anisotropy field H^{i}_{anis} will take a different form for other crystal symmetries. The demagnetization field $\underline{H}_{d}$ is determined from Ampere's law ($\nabla \times \underline{H}_{d} = 0$), Gauss's law ($\nabla \cdot \underline{B} = 0$), and the relation between the magnetic induction $\underline{B}$ and magnetization $\underline{m}$ [99]:

$$\underline{B} = \underline{H}_{d} + M_s \underline{m} \tag{3-9}$$

$\underline{H}_{d}$ is expressed as the gradient of a magnetic potential ϕ by using Ampere's law[99]:

$$\underline{H}_d = -\nabla\phi \tag{3-10}$$

Using Gauss's law with equations (3-9) and (3-10), the magnetic potential ϕ satisfies the Poisson equation[33][99]:

$$\nabla^2\phi = \nabla\cdot\left(M_s\underline{m}\right) \tag{3-11}$$

The magnetoelastic field is obtained by differentiating the elastic energy density in equation (3-7) [31][33]:

$$\underline{H}_{me} = -\frac{1}{\mu_0 M_S}\underline{\underline{\underline{C}}}\left(\underline{\underline{\varepsilon}} - \underline{\underline{\varepsilon}}^m\left(\underline{m}\right) - \underline{\underline{\varepsilon}}^{PE}\left(\underline{E}\right)\right)\cdot\frac{\partial\underline{\underline{\varepsilon}}^m\left(\underline{m}\right)}{\partial\underline{m}} \tag{3-12}$$

The mechanical response of the is governed by the elastodynamic equation [33]

$$\rho\frac{\partial^2\underline{u}}{\partial t^2} - \nabla\cdot\underline{\underline{\sigma}} = \underline{0} \tag{3-13}$$

where ρ is the mass density. The total strain $\underline{\underline{\varepsilon}}$ from equation (3-1) is related to the displacement $\underline{u}$ vector as

$$\underline{\underline{\varepsilon}} = \frac{1}{2}\left(\nabla\underline{u} + \left(\nabla\underline{u}\right)^T\right) \tag{3-14}$$

and the stress tensor $\underline{\underline{\sigma}}$ is related to the strains as[33]:

$$\underline{\underline{\sigma}} = \underline{\underline{\underline{C}}}\,\underline{\underline{\varepsilon}}^{el} = \underline{\underline{\underline{C}}}\left[\underline{\underline{\varepsilon}} - \underline{\underline{\varepsilon}}^m\left(\underline{m}\right) - \underline{\underline{\varepsilon}}^{PE}\left(\underline{E}\right)\right] \tag{3-15}$$

Equations (3-1) - (3-15) represent a system of equations describing the electro-magneto-mechanical response. Substituting equations (3-14) and (3-15) and the expression for $\underline{\underline{\varepsilon}}^m\left(\underline{m}\right)$ into equation (3-13) results in a modified elastodynamic partial differential equation in terms of displacements $\underline{u}$, electric field $\underline{E}$ and magnetization $\underline{m}$ [32]:

$$\rho\frac{\partial^2\underline{u}}{\partial t^2} - \nabla\cdot\underline{\underline{\underline{C}}}\left[\frac{1}{2}\left(\nabla\underline{u} + \left(\nabla\underline{u}\right)^T\right)\right] + \nabla\cdot\underline{\underline{\underline{C}}}\left(\underline{\underline{\lambda}}^m\,\underline{m}\underline{m}^T\right) + \nabla\cdot\underline{\underline{\underline{C}}}\left(\underline{\underline{d}}\,\underline{E}\right) = \underline{0} \tag{3-16}$$

where the electric field E is obtained from equation (3-4). Note that the partial differential equation is fully coupled with electric ($\underline{E}(V)$), magnetic ($\underline{m}$), and mechanical displacement fields ($\underline{u}$); thus a fully coupled multiferroic material is modeled. Combining equations (3-6) and (3-7) produces the modified LLG equation in terms of displacements ($\underline{u}$), electric field ($\underline{E}$) and magnetization ($\underline{m}$):

$$\frac{\partial \underline{m}}{\partial t} = -\mu_0 \gamma \left(\underline{m} \times \left(\underline{H}_{ext} + \underline{H}_{ex}(\underline{m}) + \underline{H}_{d}(\phi) + \underline{H}_{anis}(\underline{m}) + \underline{H}_{me}(\underline{m}, \underline{u}(\underline{E})) \right) \right) + \alpha \left(\underline{m} \times \frac{\partial \underline{m}}{\partial t} \right) \quad (3\text{-}17)$$

Equations (3-5), (3-11), (3-16) and (3-17) represent eight fully coupled partial differential equations for the eight unknown variables represented by V , $\underline{u}$, ϕ and $\underline{m}$. In this chapter, the coupled PDEs are formulated in their weak forms. The weak form of equation (3-5) is obtained by multiplying it by test functions β which satisfy boundary conditions, and then integrating over the volume Ω . Using the divergence theorem gives

$$\begin{aligned} &\int_{\Omega} \left(\varepsilon_s - \underline{\underline{d}} \underline{\underline{\underline{\underline{C}}}} \underline{\underline{d}}^T \right) (-\nabla V) \frac{\partial \beta}{\partial \underline{x}} d\Omega + \int_{\Omega} \left(\underline{\underline{d}}^T \underline{\underline{\underline{\underline{C}}}} \left(\frac{1}{2} \left(\nabla \underline{u} + (\nabla \underline{u})^T \right) - \underline{\underline{\underline{\lambda}}}^m \underline{m}\underline{m}^T \right) \right) \frac{\partial \beta}{\partial \underline{x}} d\Omega = \\ &\int_{S} \left(\varepsilon_s - \underline{\underline{d}} \underline{\underline{\underline{\underline{C}}}} \underline{\underline{d}}^T \right) (-\nabla V) \beta n dS + \int_{S} \left(\underline{\underline{d}}^T \underline{\underline{\underline{\underline{C}}}} \left(\frac{1}{2} \left(\nabla \underline{u} + (\nabla \underline{u})^T \right) - \underline{\underline{\underline{\lambda}}}^m \underline{m}\underline{m}^T \right) \right) \beta n dS \end{aligned} \quad (3\text{-}18)$$

with the following prescribed electric potential boundary conditions

$$V = V_0 \text{ on } S \quad (3\text{-}19)$$

where V_0 is the electric potential on the surface S. The weak form of equation (3-11) is obtained by using a test functions ζ giving[99]

$$-\int_{\Omega} (\nabla \phi) \frac{\partial \zeta}{\partial \underline{x}} d\Omega + \int_{\Omega} \left(M_s \underline{m} \right) \frac{\partial \zeta}{\partial \underline{x}} d\Omega + \int_{S} \left(-\nabla \phi + M_s \underline{m} \right) \zeta n dS = 0 \quad (3\text{-}20)$$

With the following prescribed magnetic potential boundary conditions[99],

$$\begin{cases} \phi_{in} = \phi_{out} \\ \dfrac{\partial \phi_{in}}{\partial n} - \dfrac{\partial \phi_{out}}{\partial n} = -\left(M_s \underline{m}\right) \cdot n \end{cases} \quad \text{on } S \tag{3-21}$$

where ϕ_{in} and ϕ_{out} are the inner and outer magnetic potentials and $\hat{n}$ is the unit normal to the surface S. Similarly, the weak formulation for equation (3-16) is obtained by using test vector functions η, producing

$$\begin{aligned} &\int_\Omega \left(\rho \frac{\partial^2 \underline{u}}{\partial t^2}\right) \cdot \underline{\eta} d\Omega + \int_\Omega \nabla \underline{\eta} \cdot \left(\underline{\underline{\underline{\underline{C}}}} \left[\frac{1}{2}\left(\nabla \underline{u} + \left(\nabla \underline{u}\right)^T\right)\right]\right) d\Omega + \int_\Omega \left[\underline{\underline{\underline{\underline{C}}}} \left(\underline{\underline{\underline{\lambda}}}^m \underline{m} \underline{m}^T\right) + \underline{\underline{\underline{\underline{C}}}} \left(\underline{\underline{\underline{d}}}(-\nabla V)\right)\right] \nabla \underline{\eta} d\Omega \\ &= \int_S \underline{\eta} \cdot \underline{\underline{\underline{\underline{C}}}} \left[\frac{1}{2}\left(\nabla \underline{u} + \left(\nabla \underline{u}\right)^T\right) - \left(\underline{\underline{\underline{\lambda}}}^m \underline{m} \underline{m}^T\right) - \left(\underline{\underline{\underline{d}}}(-\nabla V)\right)\right] \cdot \hat{n} dS \end{aligned} \tag{3-22}$$

with prescribed displacements and prescribed tractions on the corresponding boundaries[31],

$$\underline{u} = \underline{u}^0 \qquad \text{on } S_1 \tag{3-23.1}$$

$$\underline{\underline{\sigma}} \cdot \hat{n} = \underline{t} \qquad \text{on } S_2 \tag{3-23.2}$$

where S_1 and S_2 are sub-boundaries on S ($S_1 \cup S_2 = S$). Finally, to construct the weak form of equation (3-17), the vector test function $\underline{\psi}$ is used to produce

$$\begin{aligned} &\int_\Omega \left(\frac{\partial \underline{m}}{\partial t} - \alpha \left(\underline{m} \times \frac{\partial \underline{m}}{\partial t}\right)\right) \cdot \underline{\psi} d\Omega = \\ &-\int_\Omega \mu_0 \gamma \left(\underline{m} \times \left(\underline{H}_{ext} + \underline{H}_d + \underline{H}_{anis} + \underline{H}_{me}\right)\right) \cdot \underline{\psi} d\Omega + \frac{2A_{ex}\gamma}{M_s} \sum_l \int_\Omega \left(\underline{m} \times \frac{\partial \underline{m}}{\partial x_l}\right) \cdot \frac{\partial \psi_l}{\partial x_l} d\Omega \end{aligned} \tag{3-24}$$

with the boundary condition [24][25] [91][101]

$$\frac{\partial \underline{m}}{\partial n} = 0 \qquad \text{on } S \tag{3-25}$$

and subject to the constraint [24][25] [91][101]

$$\left|\underline{m}\right| = 1 \qquad \text{on } \Omega \tag{3-26}$$

which is a direct consequence of the LLG equation [24][25] [91][101]. Finally, equations (3-18), (3-20), (3-22), and (3-24) in addition to the boundary conditions given in equations (3-19), (3-21), (3-23), and (3-25), represent a well-posed problem that can be solved using finite element methods.

The weak forms are solved using the finite element method with an implicit time stepping scheme and backward differentiation formula (BDF)[102]. To decrease solution time, the system of equations is solved using a segregated solution approach, which splits the solution process into substeps using a damped Newton's method[102]. For all numerical problems, convergence studies (i.e., mesh size and time steps) were conducted to ensure accuracy. The time step is 5 x 10^{-11} s and duration is 2 x 10^{-12} s[102].

3.3 Results

Prior to showing analytical results, we first describe the physical mechanism of deterministically reorienting the magnetization in a single domain element by 90 degrees using magnetoelastic properties[107]. Figure 3-1 shows the energy profiles as a function of the magnetization angle for two different nanoscale geometries (~100 nm, in-plane 10 nm thick), i.e. a circular. Figure 3-1(a) or elliptical disk Figure 3-1(b). For a circular disk, as shown in Figure 1a, there are no preferential magnetic energy wells, thus the in-plane magnetization direction is independent of angle. For an elliptical disk, as shown in Figure 3-1(b), there are two energy minima aligned along the major axis at 0 and 180 degrees. By introducing a magnetic bias field (H_b) aligned along the ellipse's minor axis (see Figure 3-1(c)), the angle between the energy wells decreases, i.e. from 0/180 in Figure 3-1(b) to 45/135 in Figure 1c with H_b applied. The simultaneous application of a magnetic field and a mechanical strain to the magnetoelastic ellipse (e.g. negative magnetostriction), as shown in Figure 3-1(d) and Figure 3-1(e), modifies the two energy wells magnitude relative to each other rather than substantially change the angle (i.e. 45/135). This approach, i.e. application of a constant magnetic bias field with the application and removal of a mechanical strain, allows deterministic strain-mediated switching between two stable states[107].

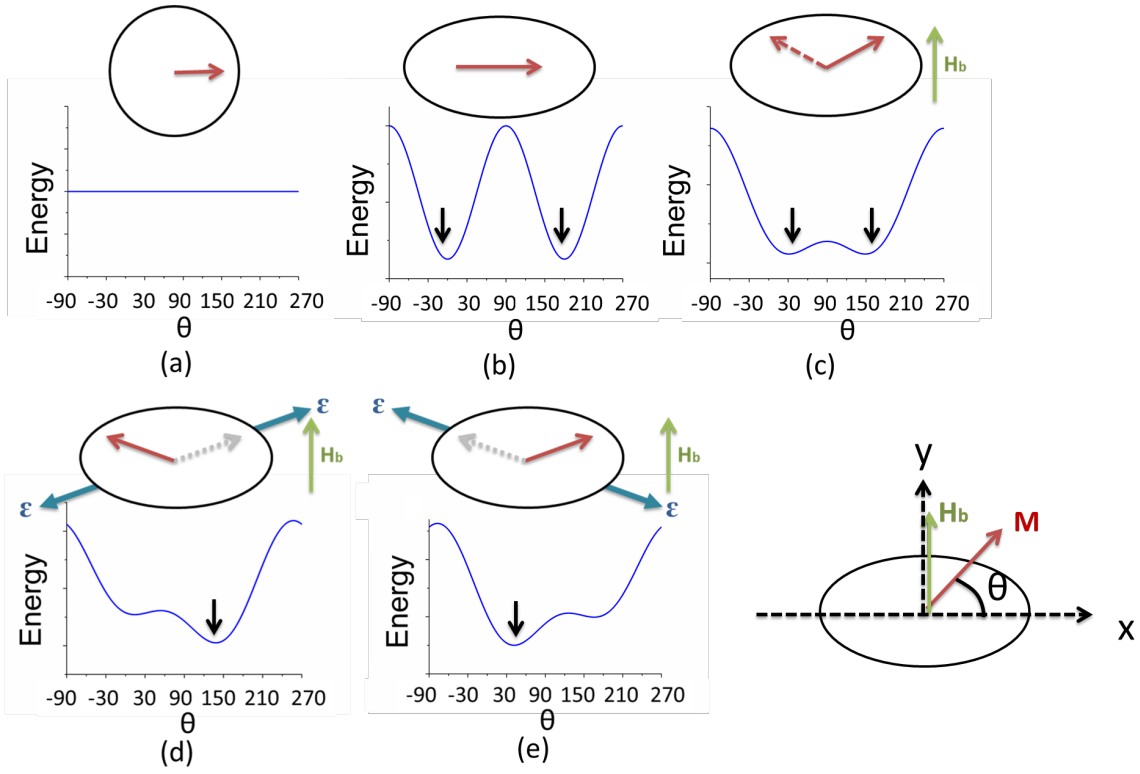

Figure 3-1 (Color) An energetic diagrammatic description of the proposed memory element.

(a) Circular disk: Isotropic shape in-plane.

(b) Elliptical disk: shape anisotropic induced easy direction along the major axis of the ellipse (0 or 180).

(c) Bias field effect: two stable states are generated by a bias field H_b. Energy barrier between two states is lowered by bias field H_b.

(d) and (e) Interaction of shape anisotropy, bias field, and applied tensile strain, changing the energy profile (+θ or –θ).

Figure 3-2 shows an illustration of the analytical model to demonstrate reorientation of a Ni magnetoelastic ellipse. The 500 nm PZT-5H thin film has a Pt bottom ground electrode deposited onto a 0.5mm thick Si substrate. The PZT-5H is represented with linear piezoelectric elements (i.e., subset of derived model) for this region. While not shown in Figure 3-2(a), an exchange layer could be used between the Pt and Ni structures for applying the bias field in-situ (i.e. following the concept introduced in Figure 3-1(d) & Figure 3-1(e))[117]. Figure 3-2(a) shows the 150nm x 120 nm x 10 nm Ni ellipse surrounded by four 125 nm x 125 nm x 10 nm Au electrodes. The Ni is represented with nonlinear magnetoelastic elements, while the Au is represented with linear mechanics elements (i.e. both subsets of the derived model). The two electrodes A-A are at a 45-degree angle, and the two electrodes B-B are at a 135 degree angle relative to the major axis of the ellipse (i.e. x-direction). The PZT-5H film is poled through the thickness in the z direction. The model presented in Figure 3-2 for the Ni ellipse, the electrodes, and the PZT-5H film thickness have not been optimized for a given objective function and are only presented to demonstrate the concept of single domain switching by 90 degrees on a thin film PZT mounted to a Si substrate. Rather than model the entire substrate, the interface of the PZT with the Pt/Si interface is clamped to prevent displacement. As shown in the cross-section of Figure 3-2(b), the in-plane x-y dimensions have been reduced to 1000 x 1000 nm, and these boundaries along the x- and y-directions are also clamped to prevent displacements. In this model voltage is always applied to two top Au electrode sets (i.e. either A-A or B-B sets) with the bottom Pt electrode grounded; that is, the electric field is applied through the thickness of the PZT-5H. Figure 3-2(c) illustrates the deformation generated with the application of a voltage to produce a positive electric field. The d_{33} out-of-plane extension under the two sets of electrodes (e.g. A-A) generates an in-plane anisotropic tensile strain in the Ni nanodot, as illustrated with

the dashed line. This local anisotropic strain switches the magnetic spin state of the Ni ellipse (or energy wells) between the two stable energy wells, as shown in Figure 3-1(d) and Figure 3-1(e). The strain produced with this geometric configuration has been previously demonstrated on a bulk PZT sample, as described by Cui[113]. When the A-A electrodes are energized, the spins align along 45 degree direction; while if the B-B electrodes are energized, the spins align along 135 degree. Both angles represent stable equilibrium positions without a voltage/electric field applied.

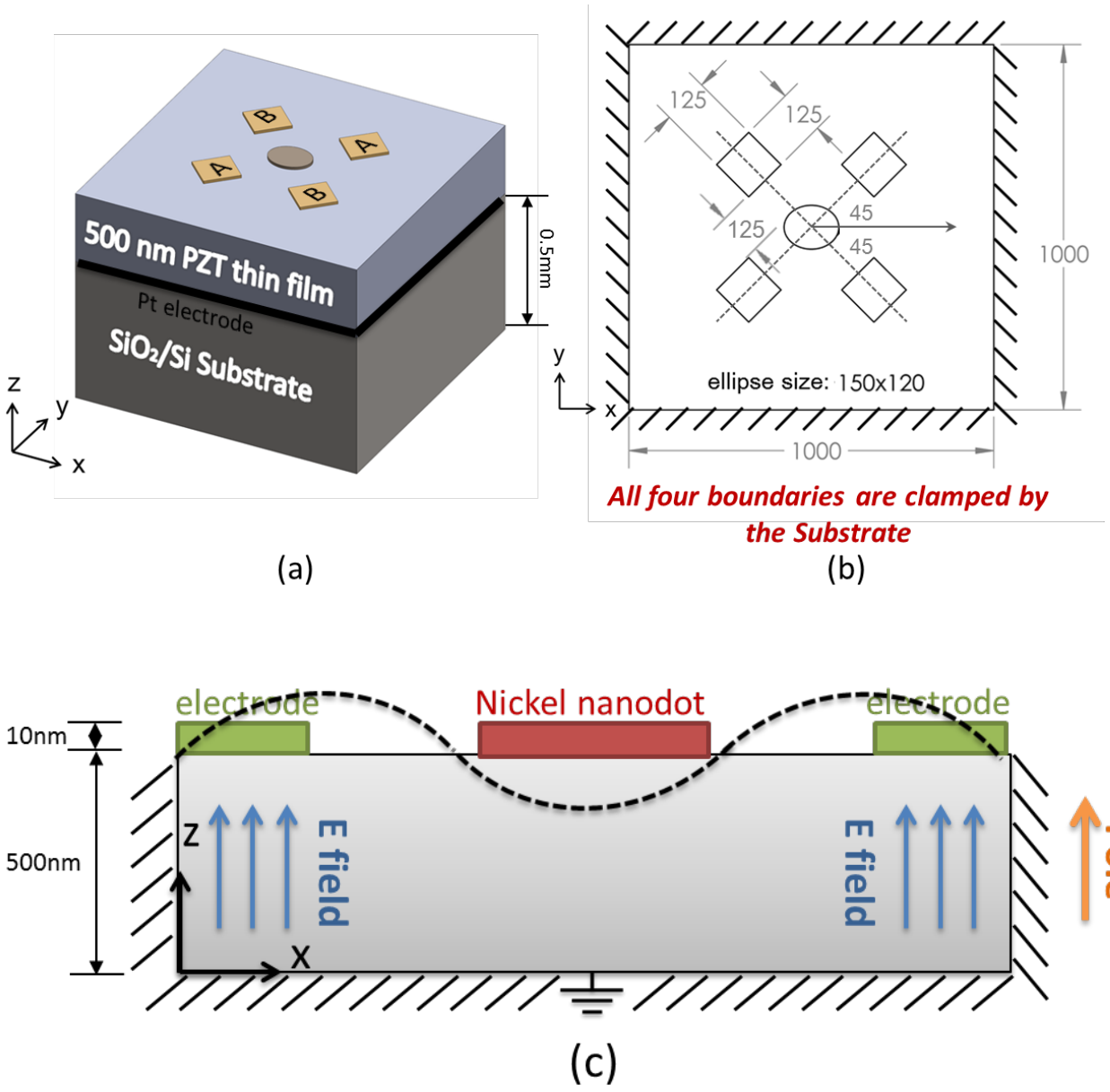

Figure 3-2 (Color) Schematic of the bi-stable memory bit.

(a) The memory bit consists of an elliptical ferromagnetic element deposited on a ferroelectric layer with patterned electrodes around the ferromagnetic element.
(b) Schematic of top view, showing all four boundaries of the PZT thin film clamped by the Si substrate.
(c) Cross-section view, showing mechanical response to applied electric field. By applying a positive voltage to the two electrode pairs (A-A), mechanical stretching is induced between the electrodes.

The finite element model for Figure 3-2(a) is constructed as follows. The nickel properties are $M_s = 4.8\times10^5 (A/m)$; $A_{ex} = 1.05\times10^{-11} (J/m)$; $\lambda_{100} = -46\times10^{-6}$, $\lambda_{111} = -24\times10^{-6}$, $c_{11} = 2.5\times10^{11} (N/m^2)$, $c_{12} = 1.6\times10^{11} (N/m^2)$, and $c_{44} = 1.18\times10^{11} (N/m^2)$ [97]. The magnetocrystalline anisotropy energy term is an order of magnitude smaller than the magnetoelastic energy (i.e. soft ferromagnetic material) and is assumed negligible. The Gilbert damping constant was set as $\alpha = 0.5$ to improve stability and process time. The PZT-5H material properties are [102] $d_{33} = 5.93\times10^{-10} (C/N)$; $d_{31} = -2.74\times10^{-10} (C/N)$, $c_{11} = c_{22} = 1.27205\times10^{11} (Pa)$, $c_{12} = 8.02122\times10^{10} (Pa)$, $c_{13} = c_{23} = 8.46702\times10^{10} (Pa)$, $c_{33} = 1.17436\times10^{11} (Pa)$, $c_{44} = c_{55} = 2.29885\times10^{10} (Pa)$, and $\rho = 7500 (kg/m^3)$. The Young's modulus and Poisson's ratio for Au are $E^{Au} = 7\times10^{10} (N/m^2)$ and $\nu^{Au} = 0.44$, respectively[102]. The exchange length, defined as $\sqrt{\frac{2A_{ex}}{\mu_0 M_s^2}}$, is 8.5 nm for nickel[97][115]. The nickel nanoellipse is discretized using tetrahedral elements with a size on the order of nickel's exchange length. The remainder of the structure (i.e. PZT-5H thin film, Au electrodes) is discretized using tetrahedral elements with graded element sizes dependent upon local geometry. The voltage used during this study is -0.5 V applied as a step function for 6 x 10^{-11} s on either electrodes A-A or B-B (electrical field through the thickness is 1 MV/m). That is, a voltage is applied for a period of time sufficiently long to allow spin equilibrium to be obtained, and the voltage is then removed. All simulations include a magnetic bias field applied along the minor axis of the nano-ellipse. Prior to application of the bias magnetic field or voltage, all magnetic spins are uniformly canted out of the x-y plane at 45 degrees and allowed to precess toward an equilibrium state.

The first study determines the influence of magnitude bias field (Figure 3-1(b)-(c)) on the location of the magnetic energy wells. In this study, the same boundary conditions as described above were used, but the applied voltage is zero. Figure 3-3 plots the magnetic energy well location (see insert for angle definition) as a function of applied bias magnetic field. Figure 3-3 also includes results from a Stoner-Wohlfarth model [10][98]with the finite element model. As the results show, as the magnetic field increases, the angle of the stable energy well increases and approaches 90 degrees. While the Stoner-Wohlfarth and the finite element model are in good agreement when determining the location of the energy wells, the Stoner-Wohlfarth model does a poor job of predicting the combined magnetic/elastic response of this structure. To approach the angle pictorially represented in Figure 3-1(c), a constant bias field (H_b) of 9000 A/m is required to orient the magnetic energy wells at ~45 and ~135 degrees. This value can be achieved using an antiferromagnetic exchange coupling layer[117]. The following simulations incorporate an $H_{b=}$ 9000 A/m.

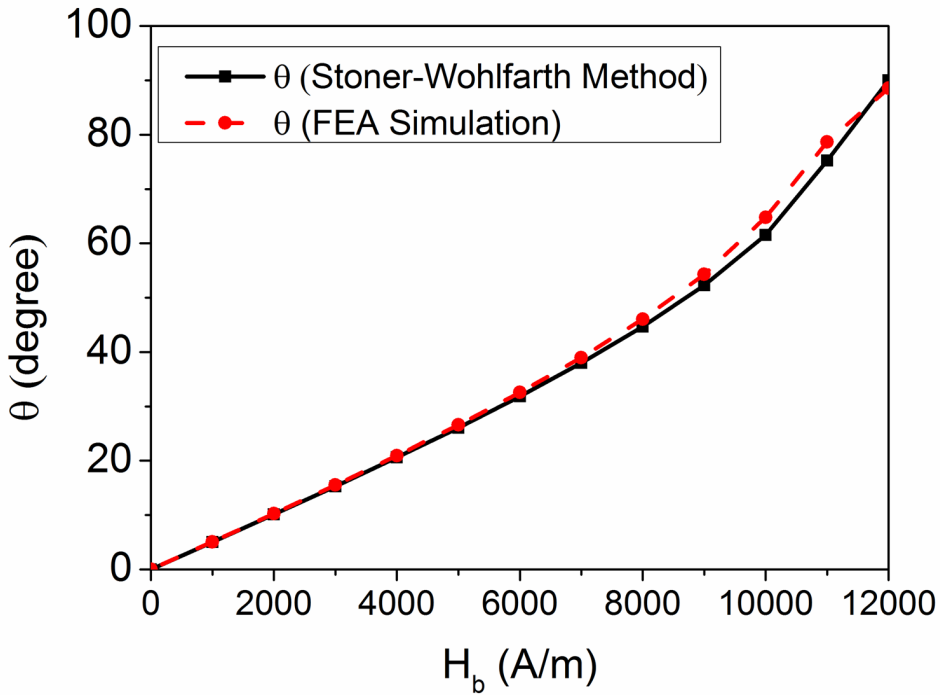

Figure 3-3 (Color) The angle of the energy minima and energy barrier, comparing values obtained from Stoner-Wohlfarth (SW) calculation and present FEA simulation work, as a function of applied bias field.

Figure 3-4 shows results for H_b= 9000 A/m and -0.5 V applied to the A-A electrode pair. In Figure 3-4(a), a three-dimensional deformation plot along with relative strain contour plots ($\varepsilon'_{AA} - \varepsilon'_{BB}$) are presented. The terms ε'_{AA} and ε'_{BB} represent the normal strains along A-A and B-B axes, respectively. The contour plot indicates that the strain is limited to the region between electrodes A-A and does not significantly influence the surrounding region. Figure 3-4(b) provides a 2-D deformation plot along with relative strain contour plots for section A-A. The deformation is very similar to that presented in Figure 3-2(c). That is, the PZT beneath the electrodes expands out-of-plane. This expansion, in turn, generates tensile strain in the center region along the A-A direction. The contour strain plot shows that the anisotropic strain ($\varepsilon'_{AA} - \varepsilon'_{BB}$) in the Ni nanoellipse is on the order of 450 με but is spatially distributed. To more closely examine the strain distribution, Figure 3-4(c) provides the anisotropic strain ($\varepsilon'_{AA} - \varepsilon'_{BB}$) as a function of position along the A-A direction (see insert). The five curves in the figure represent five different *z* locations through the thickness in the Ni nanoellipse. In general, the anisotropic strain decreases from the bottom (i.e. interface of PZT with Ni) to the top of the Ni nanoellipse. Also there is a significant reduction in strain near the edges of the Ni nanoellipse, *x* = 40 nm and 175 nm due to the shear lag effect. Shear lag effects become important and must be taken into account as the thickness of the magnetic layer increases relative to the minor axis dimension. At the top of the Ni (t = 10 nm), the strain near the edge (axis = 40nm and 175nm) is about 100 με, while the relative strain at the center (axis=100nm) is about 400 με. At the bottom of the Ni (t = 2 nm), the strain near the edge (*x* = 40nm and 175nm) is about 300 με while the relative strain at the center (*x* = 100nm) is about 500 με, which shows that the strain decreases through the thickness. The average strain transferred to the nanoellipse is approximately 450 με,

representing a ~60% decrease in strain magnitude compared to material near the electrodes (~1000με). The strain also decreases significantly in the Ni nanoellipse between two neighbors.

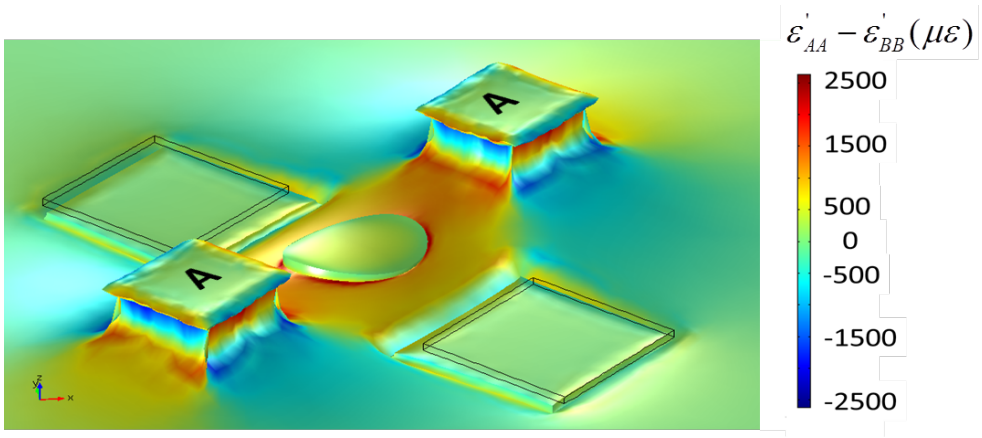
$\varepsilon'_{AA} - \varepsilon'_{BB}(\mu\varepsilon)$
2500
1500
500
0
-500
-1500
-2500
A
A

(a)

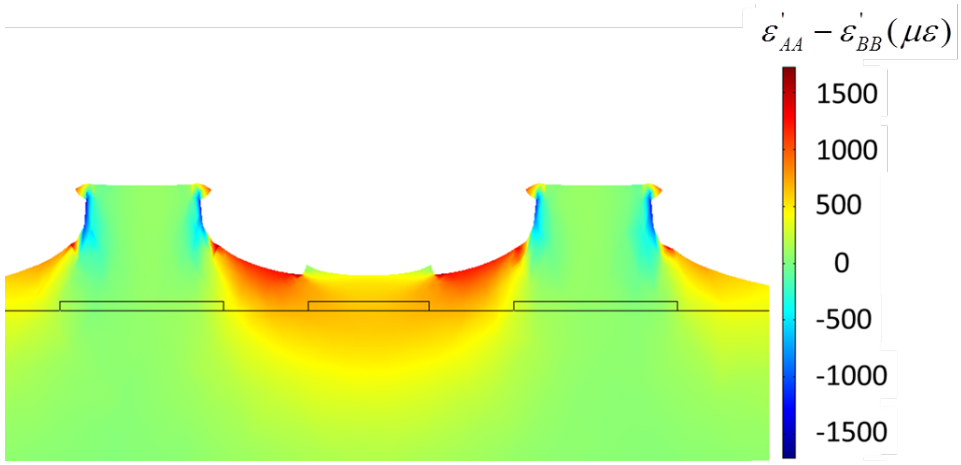
$\varepsilon'_{AA} - \varepsilon'_{BB}(\mu\varepsilon)$
1500
1000
500
0
-500
-1000
-1500

(b)

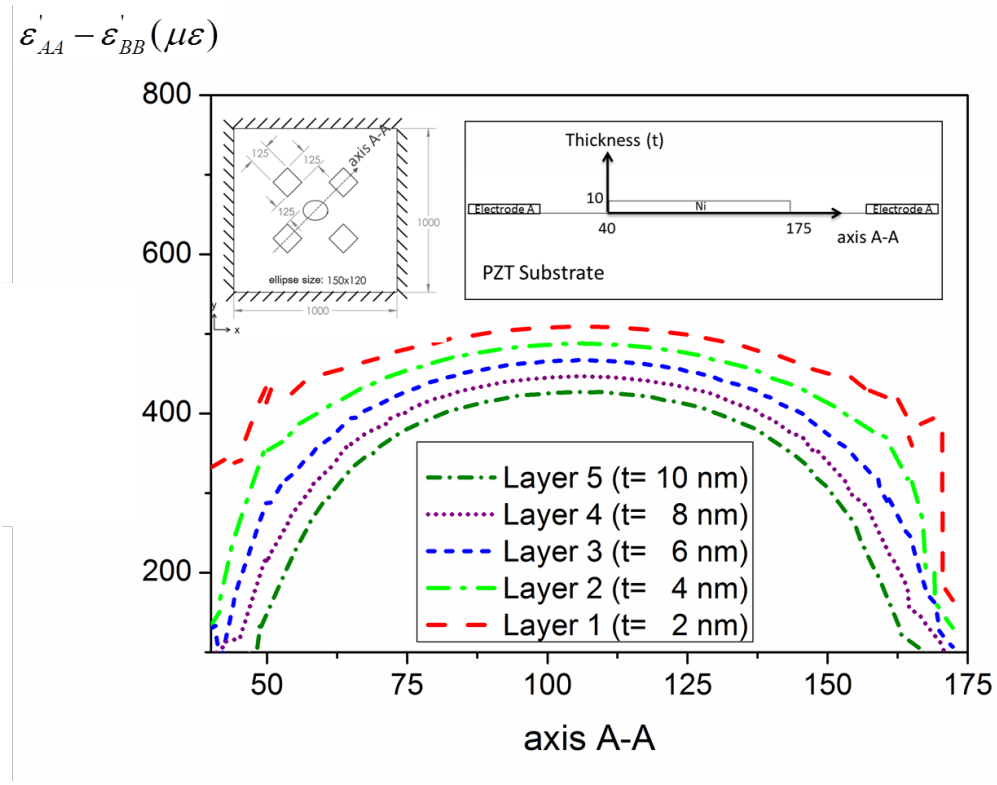

(c)

Figure 3-4 (Color) Simulation results (displacement scale exaggerated)

(a) Voltage applied on A-A electrode pair. Two electrodes expand out-of-plane and tensile strain is induced in the middle region.

(b) Cross-section 2D plot along A-A. Tensile strain is induced in the middle (~800 με). The strain transferred to the nano-ellipse is ~450 με. Non-uniform strain distribution exists between the substrate and the nano-ellipse.

(c) Strain for different layers in the nanoellipse along A-A.

Figure 3-5 shows the magnetic response of the structure when either electrodes A-A (Figure 3-5(a)) or B-B (Figure 3-5(b)) are energized. The magnetization is initially in an equilibrium state at ~45 degrees with respect to the x-axis. Electrodes A-A are initially energized as shown in Figure 3-5(a). The top figure shows the voltage applied and the magnetic dipole orientations in the Ni nanoellipse after equilibrium is reached. The larger arrow on the Ni nanoellipse is used to inform the reader of the magnetic spin states of each element. The bottom Figure 3-5(a) shows an exaggerated in-plane (x-y plane) deformation plot along with a relative strain contour plot ($\varepsilon'_{AA} - \varepsilon'_{BB}$). The deformation plot in this figure illustrates the stretching of the ellipse along the A-A direction that is consistent with the results shown in Figure 3-4. This stretching causes the magnetic spins in a negative magnetic material like Ni to rotate toward the stable equilibrium position located at ~135 degrees (see Figure 3-1(d) and Figure 3-1(e)) as shown in Figure 3-5(a). When the voltage is removed (not shown), the magnetic spins are stable at ~135 degree and do not return to ~45 degrees. Following this voltage loading sequence, electrodes B-B are energized with results shown in Figure 3-5(b). As can be seen in the bottom of Figure 3-5(b), the displacement of the Ni nanoellipse is now along the B-B axis rather than along the A-A axis as shown in Figure 3-5(a). This stretching of the ellipse along B-B causes the magnetic spins to reorient along the A-A axis as shown in Figure 3-5(b) top with the large red arrow. Once the voltage is removed, the magnetic spins remain along the B-B axis since this is a stable equilibrium position (see Figure 3-1(d)).

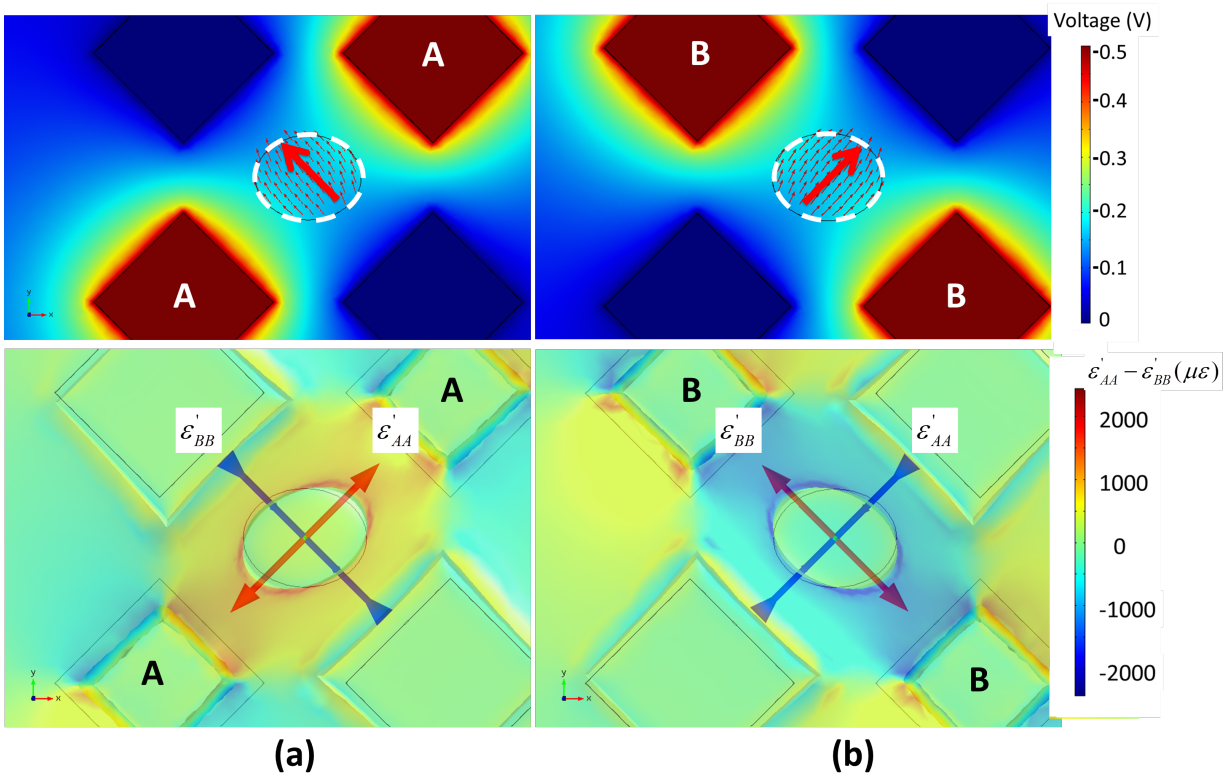

Figure 3-5 (Color) Top view of strain intensity plot from the fully-coupled simulation results.

(a) (top) Magnetization rotates due to the application of strain from electrode pair (A-A). (bottom) Applied voltage on A-A creating 45-degree tensile principle strain.
(b) (top) Magnetization rotates due to the application of strain from electrode pair (B-B). (bottom) Applied voltage to B-B creating 135-degree tensile principle strain.

Figure 3-6 shows magnetization and voltage applied as a function of time for the case presented in Figure 3-5. The blue dashed line is the voltage applied to A-A, the green dashed line is the voltage applied to B-B and the red line is the average magnetization state. The left vertical axis corresponds to the magnetization direction (i.e. angle measured from x-axis) while the right vertical axis represents voltage. Initially the stable magnetic equilibrium is at ~45 degree when a voltage is applied to A-A at time = 1.5 ns and held until 3.5 ns. The magnetization responds at approximately 2 ns and switches from 45 to ~135 at 3ns. The magnetization response time is approximately 1.5 ns. When the voltage (A-A) is removed, the magnetization remains in this new state, since it represents a stable equilibrium well. When the second pair (B-B) is energized at 4.5 ns, the magnetization rotates back to ~45 degrees, and remains there following removal of the voltage to B-B. The electrical energy required to "write" (switch) this magnetic single domain can be calculated from the surface charge on the electrodes and the applied voltage. For the mechanism shown in Figure 3-5 and Figure 3-6, the switching energy is approximately 8 fJ. This energy is associated with deformation of the PZT, strain in the electrodes, and strain in the Ni structure. This value is considered a conservative value, given that the structure has not been optimized with respect to PZT thickness or electrode size.

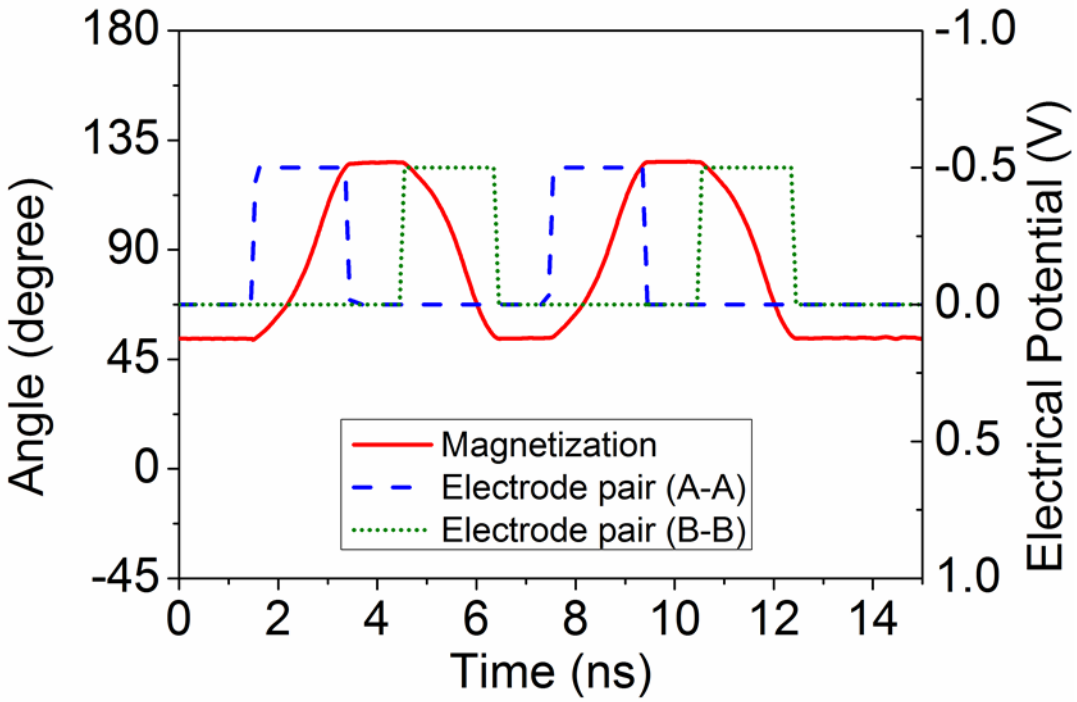

Figure 3-6 (Color) Time response of the memory bit. The magnetization starts at zero and voltage is applied to electrode pair A-A, switching M to the "1" state; voltage on B-B switches M to the "0" state. The magnetization is bi-stable. The dashed blue line represents voltage applied to A-A; the dash green line represents voltage applied to B-B; and the red line represents the response of the magnetization.

3.4 Conclusion

This chapter presented a robust analytical model combining micromagnetics with elastodynamics and electrostatics to solve a strain-mediated composite multiferroic problem. The solution was implemented in a finite element code providing both spatial and temporal information on the magnetic, electric, and mechanical fields. The problem of a single magnetic domain structure attached to a clamped piezoelectric thin film was studied. Analytical results demonstrate that out-of-plane deformations produce sufficient strain to reorient the magnetic structure, overcoming the classical substrate clamping problem. Work remains to be conducted on other magnetoelastic materials and optimizing the various structural geometries to minimize the required electrical energy to reorient or write this domain structure.

4. Deterministic switching of a magnetoelasitc single-domain nano-ellipse using bending

In this chapter, a fully coupled analytical model between elastodynamics with micromagnetics is used to study the switching energies using voltage induced mechanical bending of a magnetoelastic bit. The bit consists of a single domain magnetoelastic nano-ellipse deposited on a thin film piezoelectric thin film (500 nm) attached to a thick substrate (0.5mm) with patterned electrodes underneath the nano-dot. A voltage applied to the electrodes produces out of plane deformation with bending moments induced in the magnetoelastic bit modifying the magnetic anisotropy. To minimize the energy two design stages are used. In the first stage, the geometry and bias field (H_b) of the bit are optimized to minimize the strain energy required to rotate between two stable states. In the second stage, the bit's geometry is fixed and the electrode position and control mechanism is optimized. The electrical energy input is about 200 (aJ) which is approximately two orders of magnitude lower than spin transfer torque approaches

4.1 Introduction

The use of multiferroic systems for development of low energy memory applications has received considerable attention in the past few years. The main concept is to use a multilayered composite material system consisting of piezoelectric and magnetoelastic layers and control the magnetization by induced strain[42][43][104][108]. The actuation mechanism consists of applying voltage to a piezoelectric substrate creating deformation which in turns transfers to a ferromagnetic nano-dot placed on top. However, the multiferroic composite memory elements intrinsically reside on a fairly thick substrate system. This thick substrate clamps the piezoelectric/magnetoelastic material limiting the amount of strain that can be generated and poses a significant problem for this area of study[53][54][68][110]. In this paper we present a mechanism to overcome this limitation and, more importantly, we show that local strain profiles can be used to reorient the magnetization vector between two stable equilibrium points.

Researchers have demonstrated the feasibility of the magnetization control between stable states in thin film magnetoelastic material deposited on a thick piezoelectric substrate.This voltage induced strain mediation effect to manipulate the magnetization is generally referred to as the converse magnetoelectric effect[110]. There have been extensive studies that contain both theoretical and experimental work on strain-mediated magnetization changes, coercivity changes and strain-induced anisotropy in continuous magnetic thin films[111]. In all of the continuous film studies, the strain is appropriately assumed to be fully transferred from the ferroelectric to the ferromagnetic layer by treating the magnetoelastic energy as a pure uniaxial anisotropy to be applied to the magnetic media. For example, T. Brintlinger et al.[55] reported both experimental and analytical predictions, using OOMMF and constant strain assumptions that show reversible

switching in FeGa/BTO thin film. In recent years, several additional studies, such as ferroelectric/ferromagnetic film coupling by Lahtinen et al.[104] and magnetic thin film stress modeling by Bai et al[84], have demonstrated that this constant strain methodology works reasonably well for continuous thin films.

The strain-mediated effect in multiferroic nanostructures has been used to alter magnetic domains[128][129][130] and to shift the magnetic coercive field. Bur et al.[36] reported strain-induced coercive field changes in patterned single-domain nickel nanostructures deposited on a thick Si/SiO2 substrate using external mechanical loads. Moutis et al.[51] reported electric-field modulation of coercive field H_c using a piezoelectric on a periodic array of ferromagnetic (FM) $Co_{50}Fe_{50}$ stripes but once again this was on an entire substrate. Out of plane magnetic reorientation has also been achieved with magnetic BFO/CFO vertical heterostructures embedded into a ferroelectric described by Zavaliche et al.[49] While demonstrating the concept this approach produced excitation in all the magnetic elements simultaneously and thus, the mechanism does not lend itself to individual element control nor could it be used for deterministic reorientation of the magnetic moment. Brandlmaier et al.[52] used the biaxial strain difference produced on the side of a piezoelectric stack actuator to control the magnetic anisotropy of a thin crystalline Fe_3O_4 film on bulk material. As an alternative to using in plane polarized piezoelectric material, some researchers such as Wu used the auxetic piezoelectric strain produced by [011] cut PMN-PT while others have used PZN-PT single crystals. These single crystal approaches resulted in a proposed design of a magnetoelectric memory system but once again required bulk piezoelectric material, which is not amenable to memory fabrication processes. In a device proposed by Hu et al.,[87] they suggested individual magnetic elements

could be controlled by very small single crystal PMN-PT elements, a configuration that presents significant fabrication challenges.

The development of a strain mediated multiferroic memory device requires that the magnetization to be individually controllable for each nano-dot and the ferroelectric thin film be grown on a substrate (e.g. Si wafer). The main difficulty here is that the thin film piezoelectric is clamped by the thick substrate and prevents strain transfer. Cui et al.[113] suggested the use of patterned electrodes to overcome substrate clamping and obtain highly localized strain in a thin film piezoelectric and the magnetic material. The concept was demonstrated on a bulk ceramic and relatively large magnetic elements and did not include detailed analysis (or experiments) for thin film piezoelectric on a thick substrate controlling a single magnetic domain element.[137] In addition to single-bit multiferroic memory devices, nanomagnetic-based Boolean logic circuit also attracts research attention because of its non-volatile and energy-efficient properties. D'Souza et al.[140] experimentally demonstrated strain-induced switching of single-domain magnetostrictive nanomagnets (lateral dimensions~200 nm) fabricated on a bulk PMN–PT substrates can implement a nanomagnetic Boolean NOT gate and steer bit information unidirectionally in dipole-coupled nanomagnet chains. From their estimation, the energy dissipation for logic operations using thin film is only about ~1 aJ/bit.

The design of single domain switchable magnetoelectric heterostructures requires the use of Landau-Liftshitz-Gilbert equation. The micromagnetics tools used today are largely based on phenomenological approaches developed in the 1950s that have been refined considerably in recent years[25]. An important addition to micromagnetics was the inclusion of strain (or stress) for magnetostrictive materials by Zhu et al.[30] as an extra term in the effective magnetic field.

This was then used by Hu[34] to model the effect of stress on hysteresis curves and magnetization dynamics, showing the interaction of stress with coercivity and the easy axis of magnetoelastic materials. Based on these results, Hu et al.[106] used stability conditions and proposed an electric field read and write MERAM device. A balance of shape anisotropy and strain anisotropy was used to describe an elliptical nanomagnet that could be switched under stress by Roy et al[45]. However, in most of these studies magnetization and strain was assumed to be spatially uniform and thus did not consider the clamping issue or the effects of a properly tailored strain field profile. D'Souza et al[114]. proposed and analyzed a low-power 4-state universal logic gate using a linear array of multiferroic nanomagnets but did not consider the substrate clamping issue. Tiercelin et al[107]. described and analyzed a magnetoelectric memory cell that balanced strain anisotropy, shape anisotropy, and a bias field. In this later work the elastic contribution was modeled separately and the piezoelectric film was not attached to a substrate. Liang et al[137]. a design based on four patterned electrodes was introduced. In this work a fully coupled model was used to analyze the design and is was shown that, by applying an electric field thru the thickness of the piezoelectric substrate, the clamping effect can be overcome. Also, in this work, it was concluded that the effect of shear lag produces localized strain profiles (70%). Biswas et al[141]. proposed a scheme that can flip the magnetization of the soft layer (complete 180° rotation) in MTJ multiferroic memory bit with stress alone and without the need for any feedback circuitry that undermines the energy-efficiency and reliability of the bit writing scheme.

In this chapter, the system consists of a nanoscale single domain magnetoelastic ellipse deposited on a thin film piezoelectric wafer attached to a thick substrate. This composite is modeled by analytically coupling electrostatics, micromagnetics (LLG), and elastodynamic

partial differential equations. The piezoelectric thin film (500nm) is attached and clamped to a thick substrate which prevents relative in-plane motion of the piezoelectric film. In order to induce localized strains, two electrodes are placed under the Ni ellipse with an insulation layer. When a voltage is applied to these electrodes, bending deformation is exited, producing compression on the Ni dot. Furthermore, unlike Tiercelin's work, the piezoelectric clamping effect is fully captured by the model. The intrinsic coupling of the piezoelectric response with the magnetoelastic response through strain is modeled by coupled partial differential equations (i.e. electrostatics, micromagnetics, elastodynamics). The numerical formulation uses tetrahedral finite elements with a maximum size equal to the exchange length of Ni (~8.5 nm) providing both spatially varying strains, electric fields, and magnetic spins throughout structure. Therefore, the model captures all the relevant physics required to accurately predict the response of this multiferroic nanoscale structure.

4.2 Theory

In this section a fully-coupled micromagnetic elastodynamic simulation with piezoelectrics for finite size 3D structures is described. The coupled partial differential equations to be solved as well as the numerical method to simulate a wide range of shape and geometries are provided below. For a more detailed derivation the readers are referred to Ref.[137]

The model consists of magnetization dynamics using the Landau-Lifschitz-Gilbert (LLG) equations coupled with the mechanical strains and stresses via the equations of elastodynamics. The piezoelectric response of the thin film is modeled with linear constitutive equations relating strain with the electric field using a quasi-static electric field approximation. Other modeling assumptions include small elastic deformations, linear elasticity, electrostatics, and negligible electrical current contributions. The coupled governing equations used in this work are as follows. The elastodynamics governing equation for mechanical stresses and displacements is

$$\rho \frac{d\underline{u}^2}{dt^2} = \nabla \cdot \underline{\underline{\sigma}} \tag{4-1}$$

where ρ is the mass density, $\underline{\underline{\sigma}}$ is the stress tensor, $\underline{u}$ is the displacement vector, and t is time.

The dynamics of magnetization is defined by the phenomenological LLG equation,

$$\frac{\partial \underline{m}}{\partial t} = -\mu_0 \gamma \left(\underline{m} \times \underline{H}_{eff}\right) + \alpha \left(\underline{m} \times \frac{\partial \underline{m}}{\partial t}\right) \tag{4-2}$$

Where μ_0 is the permeability of free space, γ is the Gilbert gyromagnetic ratio, α is the Gilbert damping constant, and $\underline{m}$ is the normalized magnetization vector. The effective magnetic field, $\underline{H}_{eff}$, includes the external field ($\underline{H}_{ext}$), exchange field ($\underline{H}_{ex}$), demagnetization field ($\underline{H}_{d}$), magnetocrystalline anisotropy field ($\underline{H}_{anis}$), and magnetoelastic field ($\underline{H}_{me}$) effects. Detailed

expressions for these terms can be found in recent literatures[25][30][31][32][33][34] [137]. The demagnetization field is calculated by using the quasi-static Ampere's law. This leads to $\underline{H_d} = -\nabla\varphi$ where $\underline{H}_\mathrm{d}$ is the demagnetization field vector and φ is the potential. Combining this equation with the divergence of magnetic induction equal to zero and the constitutive relation, $\underline{B} = \mu_0(\underline{H} + \underline{M})$, produces the equation for the magnetic potential, φ, in terms of the magnetization (see Equation 4-5). The magnetization is coupled with the effective magnetic field through this demagnetization term.

Substituting the piezoelectric constitutive relations into the elastodynamics equation (4-1) and LLG equations (equation 4-2) produces a cross-coupled set of non-linear equations containing displacements, magnetization, electrical field, and magnetic potential as follows (Detail derivation in Ref. [137]):

$$\rho\frac{d\underline{u}^2}{dt^2} - \nabla\cdot\underline{\underline{\underline{C}}}\left[\frac{1}{2}\left(\nabla\underline{u} + (\nabla\underline{u})^T\right)\right] + \nabla\cdot\underline{\underline{\underline{C}}}\left[\underline{\underline{\underline{\lambda^m}}}\,\underline{mm^T}\right] + \nabla\cdot\underline{\underline{\underline{C}}}\left(\underline{\underline{dE}}\right) = 0 \qquad (4\text{-}3)$$

$$\frac{\partial\underline{m}}{\partial t} = -\mu_0\gamma\left(\underline{m}\times\left(\underline{H_{ext}} + \underline{H_{ex}}(\underline{m}) + \underline{H_d}(\varphi) + \underline{H_{ani}}(\underline{m}) + \underline{H_{me}}\left(\underline{m}, \underline{u}(\underline{E})\right)\right)\right) + \alpha\left(\underline{m}\times\frac{\partial\underline{m}}{\partial t}\right) \qquad (4\text{-}4)$$

$$\nabla^2\varphi = M_s(\nabla\cdot\underline{m}) \qquad (4\text{-}5)$$

where $\underline{\underline{\underline{C}}}$ is the stiffness tensor and $\underline{\underline{\underline{\lambda^m}}}$ is the magnetostriction tensor. $\underline{E}$ is the electric field vector, and $\underline{\underline{d}}$ is the piezoelectric coupling tensor.

In a similar fashion to magnetic potential, the quasi-static Faraday's Law implies that $\underline{E} = -\nabla V$, where V is the electric potential. This equation coupled with Gauss's Law and provides the piezoelectric coupling within the model. These coupled systems of partial differential equations are solved for the mechanical displacement (u, v, w), electric potential (V), magnetic potential (φ), and magnetization (m_x, m_y, m_z).

The numerical solution of micro-magneto-electro-mechanical coupled equations is obtained by using a finite element formulation (COMSOL) with an implicit backward differentiation (BDF) time stepping scheme[100] [101][102]. In order to decrease solution time, the system of equations is solved simultaneously but using a segregated method, which splits the solution process into sub-steps using a damped Newton's method. This coupled model provides dynamic results for the full strain and micromagnetic spin distribution in the magnetoelastic component coupled with a piezoelectric layer. For all numerical problems, convergence studies (i.e., mesh size and time steps) were evaluated to ensure accuracy.

4.3 Simulation Setup

Figure 4-1 shows the configuration studied in this paper. The design variables to be determined are the geometry of the ellipse (aaxis, baxis, caxis), position of electrodes (dist) and time history for the applied voltage V(t). A detailed description on determined these quantities in given in Section 4.4.

The material properties for the MRAM element system are as follows. The material properties for the nickel nano-dot are[102] $M_s = 4.8\times10^5(A/m)$, $A_{ex} = 1.05\times10^{-11}(J/m)$, $\lambda_{100} = -46\times10^{-6}$, $\lambda_{111} = -24\times10^{-6}$, $c_{11} = 2.5\times10^{11}(N/m^2)$, $c_{12} = 1.6\times10^{11}(N/m^2)$, $c_{44} = 1.18\times10^{11}(N/m^2)$. The nickel nano-dot is assumed polycrystalline; therefore, the magnetocrystalline anisotropy is neglected. The Gilbert damping ratio is set as α=0.5 to improve stability and process time. Using the high Gilbert damping ratio would cause the overdamped precessional motion in the magnetization response. When using realistic (lower) value of Gilbert damping, more precessional motion will be shown in the magnetization response (Figure 4-6a). The magnetization precesses with the amplitude gradually decreasing to equilibrium. For both Gilbert damping ratios, the final equilibrium state is the same. The PZT-5H material properties are $d_{33} = 5.93\times10^{-10}(C/N)$, $d_{31} = -2.74\times10^{-10}(C/N)$, $c_{11} = c_{22} = 1.27205\times10^{11}(N/m^2)$, $c_{12} = 8.02\times10^{10}(N/m^2)$, $c_{13} = c_{23} = 8.46\times10^{10}(N/m^2)$, $c_{33} = 1.17\times10^{11}(N/m^2)$, $c_{44} = c_{55} = 2.29885\times10^{10}(N/m^2)$, and $\rho = 7500(kg/m^3)$. The Young's modulus and Poisson's ratio for Au are $E^{Au} = 7\times10^{10}(N/m^2)$, and $\nu^{Au} = 0.44$, respectively. The exchange constant for nickel is $\sqrt{\frac{2A_{ex}}{\mu_0 {M_s}^2}} \sim 8.5(nm)$. The nickel nano-dot is discretized using tetrahedral elements with a size on the order of nickel's exchange length. The remainder of the structure (i.e., PZT-5H

thin film, Au electrodes) is discretized using tetrahedral elements with graded element sizes dependent upon local geometry.

The boundary conditions of the piezoelectric film are the four sides and the bottom surface of the film are clamped. The bottom surface is also grounded. The top surface is free to deform. The piezoelectric film is poling in –Z-direction. Two electrodes (electrodes A and B) are underneath the nano-dot.

4.4 Nano-dot Design

The objective in this memory applications is to design the elliptical nano-dot and actuation mechanism for minimum magnetization switching energy. In order to have deterministic rotation the stable states are offset by 5^o. This condition is not really required, but it was included here to show how this requirement can be incorporated to the design process. Also the energy barrier between stable states is constrained to be at least 40kT for thermal stability (T = 300 K room temperature). Geometric design variables for the ellipse are the major axis (aaxis), eccentricity (e, b=e*aaxis) and thickness (caxis) as well as the magnitude of the H_b to achive the offset of 5 degrees. Control design variables are the position of the electrodes (dist), amplitude and duration of the voltage pulse. The main difficulty in solving this optimization problem is that the numerical solution of the system equations (in particular the LLG equation) is extremely heavy computationally and therefore the approach of using and off the shelf optimizer linked to the finite element code in impractical as a design tool. The method adopted in this paper is to solve the problem in two steps. First the plant (ellipse geometry, H_b) is optimized with no control system and then the control system (actuator, voltage) is optimized for a fixed plan. The followings are the details of these two optimization procedures

Plant Design

In this first stage, the geometry of the ellipse and bias field (H_b) are optimized for minimum strain magnetization rotation between stable states. This design can be done neglecting the magnetization dynamics to avoid the solution of the LLG equation each time we change a dimension. Thus, we pose the problem as minimizing the average strain (ε_{xx}-ε_{yy}) required for a 90 degree rotation (the reason to use 90 instead of 180 will become evident in the next section)

subject to the conditions that the energy barrier is at least 40kT and that the stable states are offset by 5 degrees relative to the x-axis. The design variables are aaxis, e, caxis, H_b . The resultant optimal dimensions are aaxis= 130nm, e=0.9, c=10nm, H_b=492 A/m. The optimum strain, which actually corresponds to an estimate of the amplitude required by the dynamic strain, is 1000με. Also, it is important to mention that with the resultant optimal dimensions a full dynamic analysis was performed to verify that the nano-dot design satisfies the design requirements

Actuation and Control system design

In this second stage we keep the geometry of the ellipse fixed and optimized design for the control mechanism. There are two parts to it, first is the position of the electrodes and second the control law for the applied voltage (magnitude and duration of the pulse). For this optimization we run the complete fully coupled dynamic model. Due to the symmetry of the configuration, by applying the same voltage to both electrodes the magnetization will rotate 90 degrees at the most. Then, for the full rotation the symmetry has to be broken. Saying this first step was to determine the distance (dist) and the magnitude of the voltage for a 90 degree rotation. This is done for a minimum switching energy criterion. The result of this design phase is dist=52nm and V_{max}=1V (electrical field through the thickness is 2 (MV/m)). With this values we determined the proper duration of the pulses and finalize the control law for the voltage (how it is applied) First, the voltage is applied on electrodes A and B simultaneously at $time = 0$. At $time = 4$ (that is when the magnetization has rotated 90 degrees), voltage is removed from electrode B, returning to ground state. Following this, at $time = 6$, voltage on electrode A is removed and since this longer pulse on electrode A makes the magnetization cross the energy maximum, the process will make the magnetization to settle at the second energy well. Total

time duration for the cycle is 15. All the simulations for this second optimization phase consider the solution for the fully coupled dynamic model. Also, prior to application of the bias magnetic field and/or voltage, all magnetic spins are uniformly canted out of the x-y plane at 5° and allowed to precess toward an equilibrium state.

4.5 Simulation Results and Discussion

Figure 4-2 shows the deformation and strain distribution ($\boldsymbol{\varepsilon_{xx}}$) results for a bias field $H_b = 492\ (A/m)$ and voltage 1V is applied on both electrodes A and B with bottom surface grounded. In Figure 4-2(a), a three-dimensional deformation plot with bending strain along x-direction ($\boldsymbol{\varepsilon_{xx}}$) is presented. The strain ($\boldsymbol{\varepsilon_{xx}}$) represents the internal bending strain along the x-direction in the nano-dot. A 2D cross-sectional strain distribution plot is shown in Figure 4-2(b). This shows internal strain ($\boldsymbol{\varepsilon_{xx}}$) in the nano-dot and the deformation when the voltage is applied on both electrodes A and B. When positive voltage is applied, a local bending deformation is produced in the nickel nano-dot that causes stresses and strains. The magnitude of the strain is on the order of $1000\ \mu\varepsilon$ in the middle region of the nano-dot.

Figure 4-3 shows the mechanism of the bi-stable elliptical MRAM bit. Figure 4-3(a) shows the magnetization in the nano-dot with a bias field ($H_b = 492\ (A/m)$) before applying a voltage. The equilibrium magnetization was initially tilted with respect to the +x-direction by 5^o. Both electrodes A and B are initially energized as shown in Figure 4-3(b). When a positive voltage is applied, a tensile strain is produced below the neutral axis of the nano-dot and a compressive strain above the neutral axis, i.e. a bending strain. A voltage is applied for a time period (time period~4) until the magnetization rotates close to 90^o. When the magnetization rotates to 90^o, the voltage on electrode B is removed and voltage on electrode A remains on (during time=4~6). The removal of the voltage from electrode A causes the magnetization to rotate pass 90 degrees in this process. Once the magnetization rotates pass 90 degrees (at time~6), the voltage on electrode A is switched off and subsequently, the magnetization falls into the other stable energy well positioned at 170^o with respect to +x-direction as shown in Figure 4-3(d).

When all voltages are removed from electrodes, the magnetization remains at 170^o. By selecting a similar process of applying voltage to electrodes A and B, the magnetization can be switched back to 5^o, i.e. the other stable state. Therefore, the magnetization can be switched deterministically between these two states.

Figure 4-4(a) shows the strain distribution ($\boldsymbol{\varepsilon_{xx}}$) and Figure 4-4(b)-(d) show magnetization components (m_x, m_y, m_z) for different layers in the nano-dot along x-direction when voltage is applied to both electrodes A and B. Due to the bending effect in the nano-dot, internal strains result from lateral deformation. Note that the strain distribution are symmetric in both electrode regions. As shown in the Figure 4-4(a), the neutral axis is in the middle region of the nano-dot (at z=5nm), where the stress/strain induced by bending vanishes. Tensile strain is induced below the neutral axis and compressive strain is induced above the neutral axis near the electrode region. This bending strain develop from the localized out-of-plane bending effect near the electrodes when the voltage is applied on both electrodes A and B. These bending strains create a new strain-induced easy axis which causes the magnetization to rotate in the nickel nano-dot. Figure 4-4(b)-(d) show that the magnetization components (m_x, m_y, m_z) in each layer do not rotate coherently. Furthermore, due to the non-uniform strain distribution, magnetization components also have non-uniform distribution. This is important and suggests that single spin models are inappropriate for evaluating the response of this design.

Figure 4-5(a) shows the strain distribution ($\boldsymbol{\varepsilon_{xx}}$) and Figure 4-5(b)-(d) show magnetization components (m_x, m_y, m_z) for different layers in the nano-dot along x-direction when voltage is applied to electrodes A only. Due to the one-sided bending effect in the nano-dot, internal asymmetric strains result from lateral deformation. The strain distribution near the electrode A region is shown in Figure 4-5(a). As can be seen a one-side tensile strain is induced below the neutral axis and compressive strain is induced above the neutral axis near the electrode region. This is because the localized out-of-plane bending effect arises near region A when the voltage is applied on electrode A. Similar to the case of both electrodes being activated, the magnetization rotation in each layer is induced by symmetry breaking, when the voltage is applied only on electrode A, and affected by the shear lag effect resulting in non-uniform reorientation in each layer as shown in Figure 4-5(b)-(d).

Figure 4-6(a) shows the temporal response of the magnetization when a voltage is applied. The magnetization was initially in an equilibrium position, pointing to the +x-direction with 5 degrees tilt, which defines the "0" state in a representative memory device. The voltage is applied at time=0 on both electrodes A and B until time=4ns. The magnetization switches from 5^o to 90^o as approaches time=6ns. The magnetization has a relative response time of approximately 2.5 ns which is influenced by choice of damping coefficient α=0.5. This value was chosen to expedite the computation time and does not alter the results with the exception of the temporal response. When using a smaller more realistic damping coefficient α, the magnetization response is substantially faster. When the voltage is removed from electrode B while the voltage on A remains, the magnetization continues to rotate past 90^o. Once the magnetization passes 90^o, the voltage on A is removed (at time=6ns) and magnetization rotates to 170 at time=10ns, which is defined as the "1" state in a representative memory device. The

magnetization can be rotated back and forth deterministically between 5 and 170 using the appropriate voltage sequence. To determine the energy to rotate the bit the following process was used.

Figure 4-6(b) shows the temporal mechanical strain (ε_{xx}) changes in the nano-ellipse. Volume average strain response (blue line), middle point strain response (red line), and strain responses at points +-50nm from the center (green and purple lines, respectively). Three zones are shown in the strain curves. The first zone (0~4ns), when both electrodes A and B are on, shows negative average strain, negative strain for the points at +-50nm and positive strain at the middle point, therefore, symmetric bending. In the second zone (4~6ns), when the voltage is turned off from electrode B, shows negative average strain, negative strain for the points at +50nm, and positive strain at point -50nm, and positive at the middle point, therefore, unsymmetrical bending.

The write energy for this bending switching mechanism is the energy required to generate voltage on the electrodes. This energy is equivalent to amount of charge delivered to the electrodes on the PZT film, i.e., capacitor charging. This energy is called the "CV^2" energy, where C and V represent the the capacitance of the piezoelectric film and the applied voltage, and is equivalent to QV/2. The total charge (Q) supplied to the electrodes is determined from the simulations. Using this approach for the results presented in Figure 4-3 the write energy is calculated to be 0.2fJ. Here it is important to point out that the thickness of the PZT was not optimized in this study and that reduction in PZT film thickness should reduce the write energy further.

4.6 Conclusion

In this chapter, an analytical model was used to determine the optimal nanodot dimensions, electrode placement, and voltage control mechanism to cause 170^{o} magnetization rotation of a magnetoelastic single domain. The design consisted of two stages where the first stage determined the major and minor axis lengths to ensure thermal stability of a single domain nanodot as well as electrode overlap resulting in maximum localized strain with bending effect. The second stage optimized the input voltage control scheme to produce 170^{o} magnetization rotation. A physical description of the mechanism to produce the voltage induced magnetization was presented. The energy to reorient the single domain was 200 (aJ) in this particular design.

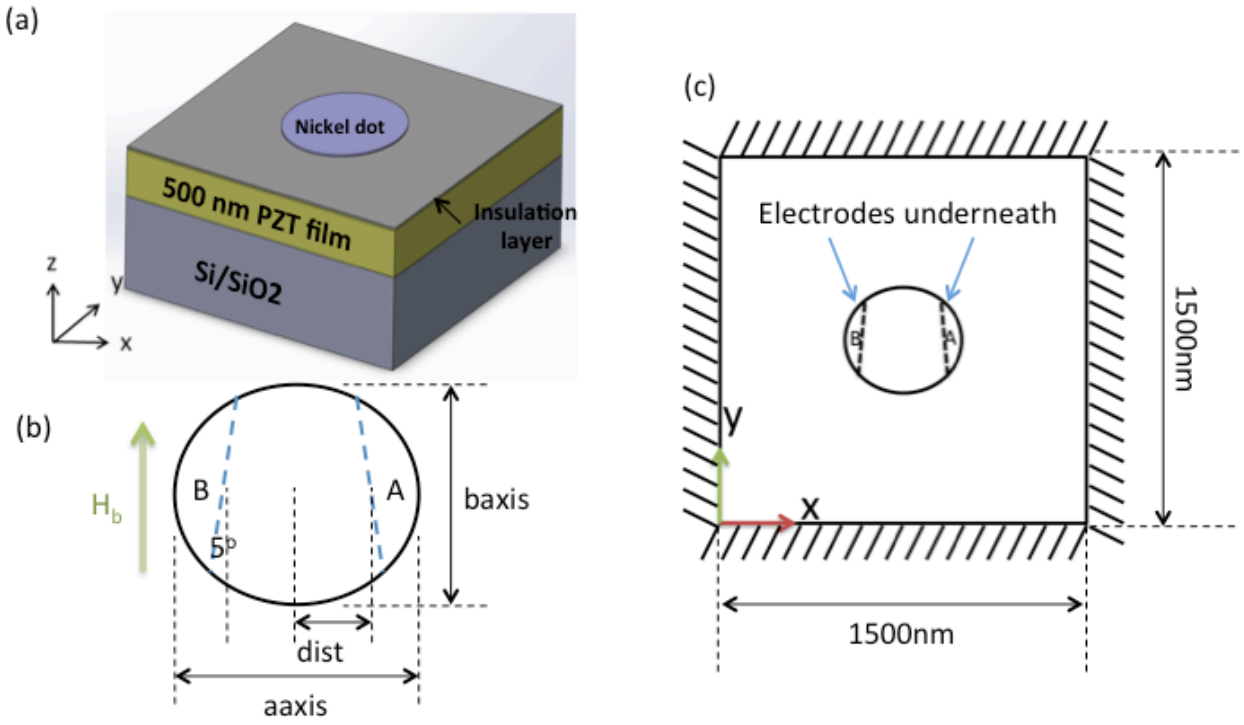

Figure 4-1 Schematic plot and Design arrangements

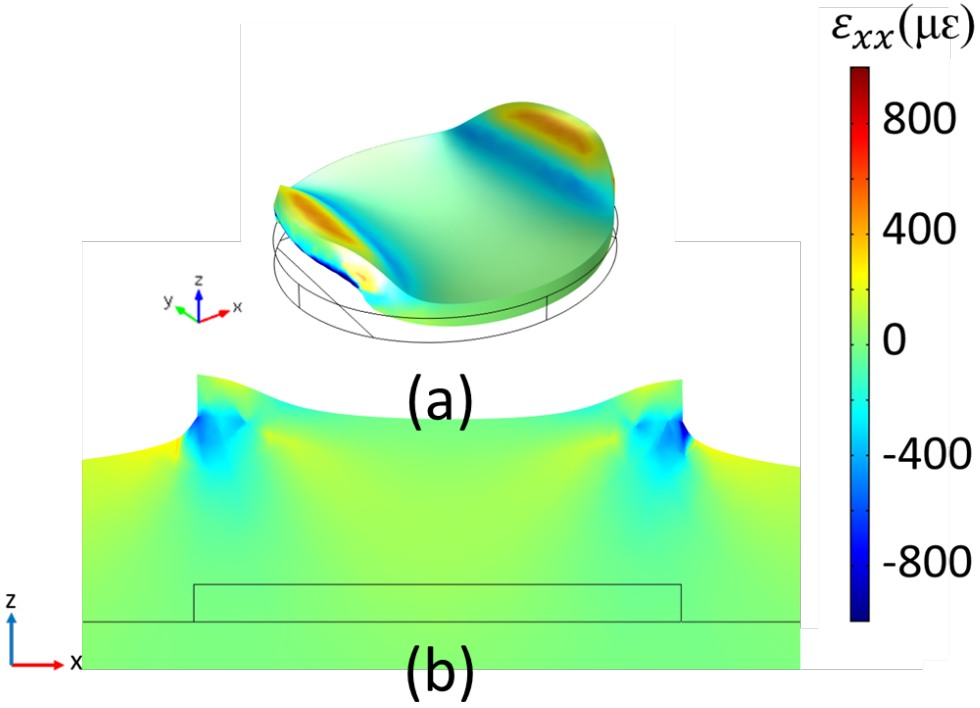

Figure 4-2 Simulation results (displacement scale exaggerated)

(a) Voltage applied on both electrodes A and B. Two electrodes expand out-of-plane and bending effect is induced in the nano-dot.

(b) Cross-section 2D plot along x-direction.

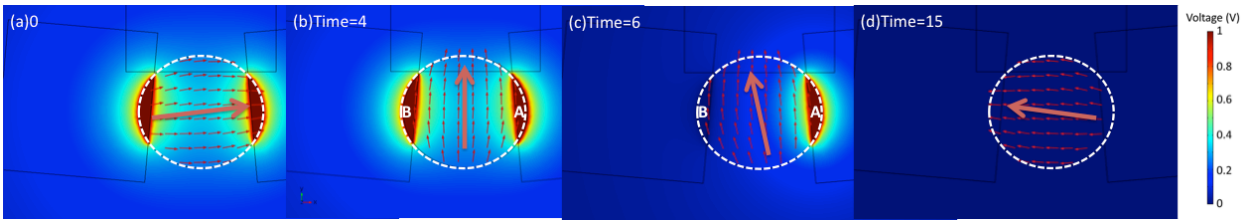

Figure 4-3 Response of the bi-stable elliptical memory bit. (Time in nanosecond)

(color: Voltage. arrow: magnetization)

(a) Starting position. The magnetization stays one of the stable states at 5 degrees with respect to x-axis.

(b) A positive voltage is applied on both electrodes A and B, the magnetization switches to 90 degrees.

(c) Switch off voltage on B and keep voltage on electrode A. The magnetization switches pass to 90 degrees.

(d) Switch off voltage on electrode A. the magnetization rotates to 170 degrees with respect to x-axis.

By applying appropriate voltage to the electrodes, the magnetization can be switched back and forth between the two bi-stable state.

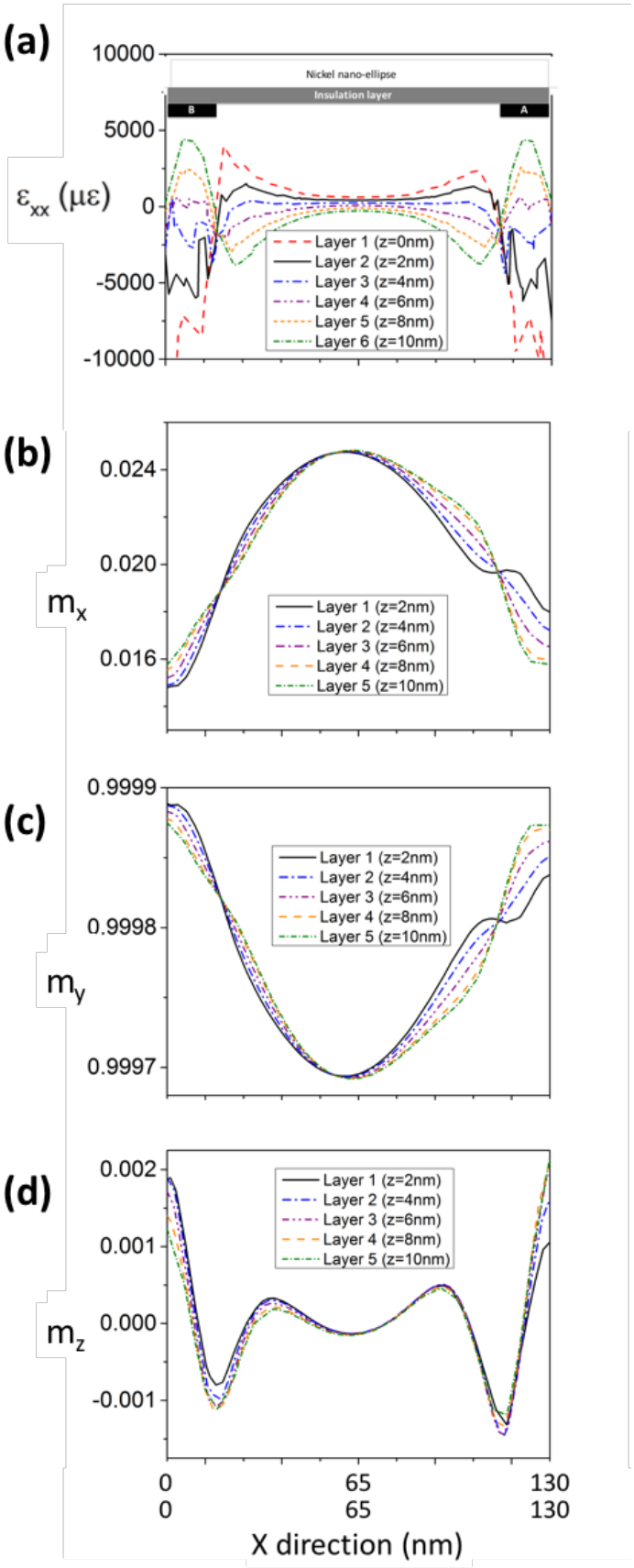
(a)
10000
5000
0
-5000
-10000
ε_{xx} (με)
Nickel nano-ellipse
Insulation layer
B
A
Layer 1 (z=0nm)
Layer 2 (z=2nm)
Layer 3 (z=4nm)
Layer 4 (z=6nm)
Layer 5 (z=8nm)
Layer 6 (z=10nm)
(b)
0.024
0.020
0.016
m_x
Layer 1 (z=2nm)
Layer 2 (z=4nm)
Layer 3 (z=6nm)
Layer 4 (z=8nm)
Layer 5 (z=10nm)
(c)
0.9999
0.9998
0.9997
m_y
Layer 1 (z=2nm)
Layer 2 (z=4nm)
Layer 3 (z=6nm)
Layer 4 (z=8nm)
Layer 5 (z=10nm)
(d)
0.002
0.001
0.000
-0.001
m_z
Layer 1 (z=2nm)
Layer 2 (z=4nm)
Layer 3 (z=6nm)
Layer 4 (z=8nm)
Layer 5 (z=10nm)
0
65
130
0
65
130
X direction (nm)

Figure 4-4 Strain and Magnetization component in different layers

Voltage applied on both electrodes A and B. Two electrodes expand out-of-plane and bending effect is induced in the nano-dot.

(a) Strain for different layers in the nano-dot along x-direction. Direct compressive strain is induced above the neutral axis of the nano-dot (z=6, 8,10nm), and direct tensile strain below the neutral axis of the nano-dot (z=0, 2,4nm).

(b) –(d) magnetization components (m_x, m_y, m_z) for different layers in the nano-dot along x-direction.

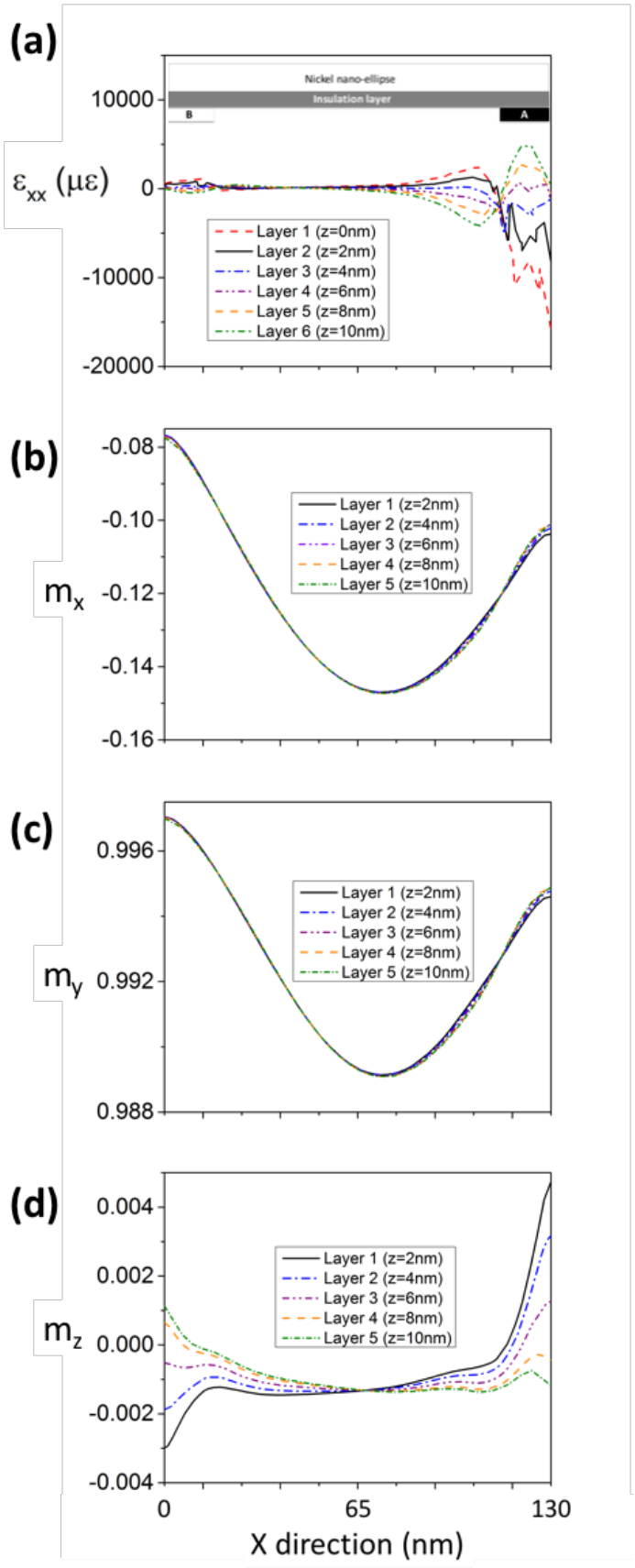
(a)
Nickel nano-ellipse
Insulation layer
B
A
10000
0
-10000
-20000
ε_{xx} (με)
Layer 1 (z=0nm)
Layer 2 (z=2nm)
Layer 3 (z=4nm)
Layer 4 (z=6nm)
Layer 5 (z=8nm)
Layer 6 (z=10nm)
(b)
-0.08
-0.10
-0.12
-0.14
-0.16
m_x
Layer 1 (z=2nm)
Layer 2 (z=4nm)
Layer 3 (z=6nm)
Layer 4 (z=8nm)
Layer 5 (z=10nm)
(c)
0.996
0.992
0.988
m_y
Layer 1 (z=2nm)
Layer 2 (z=4nm)
Layer 3 (z=6nm)
Layer 4 (z=8nm)
Layer 5 (z=10nm)
(d)
0.004
0.002
0.000
-0.002
-0.004
m_z
Layer 1 (z=2nm)
Layer 2 (z=4nm)
Layer 3 (z=6nm)
Layer 4 (z=8nm)
Layer 5 (z=10nm)
0
65
130
X direction (nm)

Figure 4-5 Strain and Magnetization component in different layers

Voltage applied on electrodes A. Electrode A expands out-of-plane and bending effect is induced in the nano-dot.

(a) Strain for different layers in the nano-dot along x-direction. Asymmetric strain is induced at electrode A region.

Direct compressive strain is induced above the neutral axis of the nano-dot (z=6, 8,10nm), and direct tensile strain below the neutral axis of the nano-dot (z=0, 2,4nm).

(b) –(d) magnetization components (m_x, m_y, m_z) for different layers in the nano-dot along x-direction.

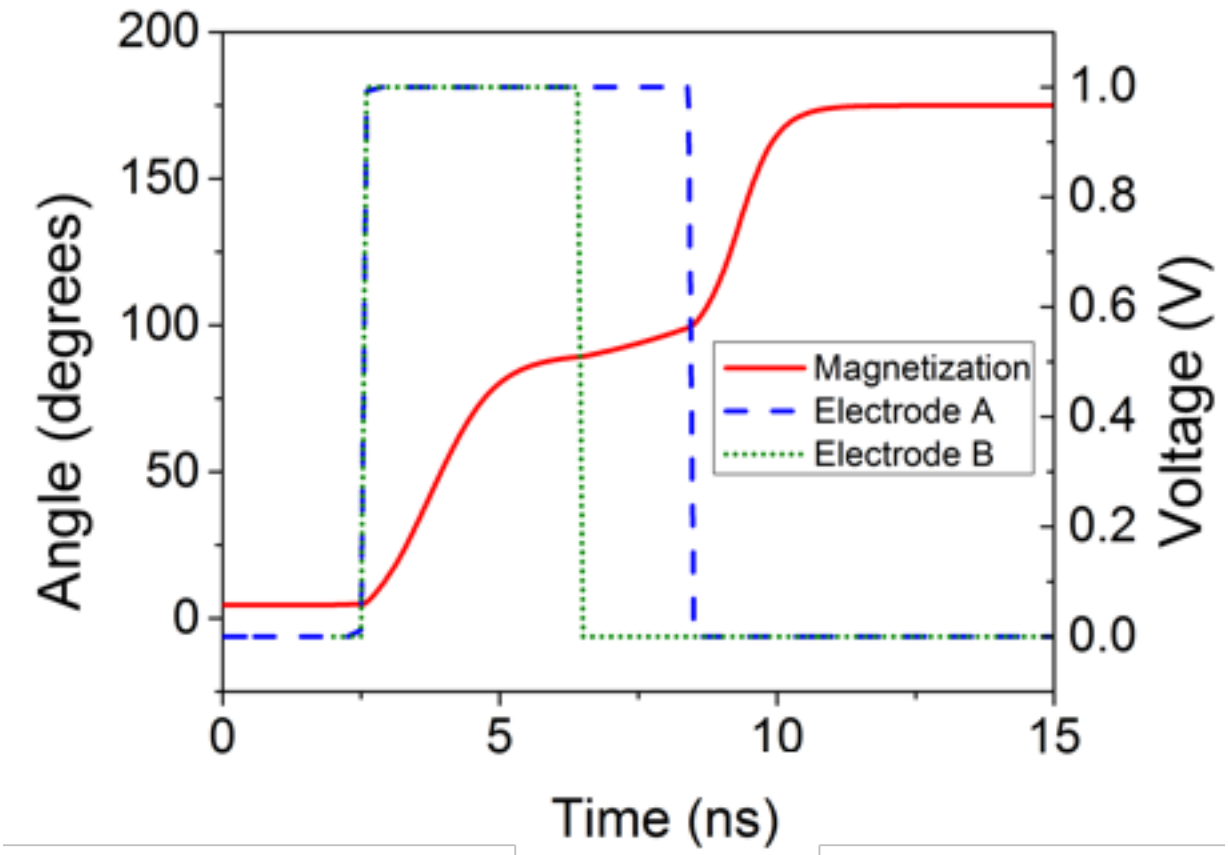

Figure 4-6(a) The magnetization starts at zero and a positive voltage is applied to both electrodes A and B, in which magnetization rotates from 5 degrees to 90 degrees. The voltage on electrode B is removed at time = 4 and the voltage remains on electrode A. The magnetization keeps rotating pass 90 degrees. Once the magnetization passes 90 degrees, the voltage on electrode A is removed and the magnetization rotates the other state (170 degrees with respect to x-axis). By applying appropriate timing application of voltages on electrodes A and B, the magnetization is able to be switched by 170 degrees.

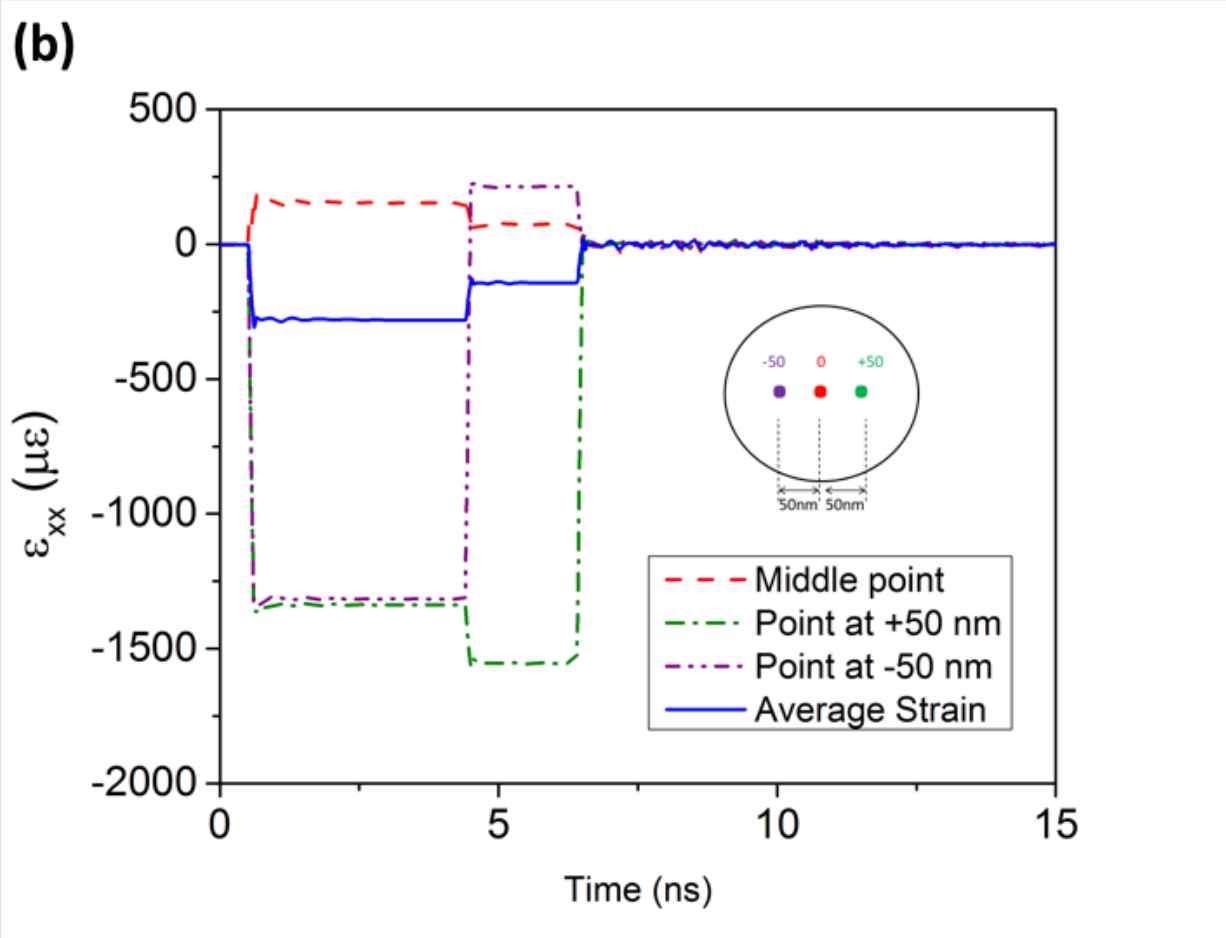

Figure 4-6(b) The temporal mechanical strain (e_{xx}) changes in the nano-ellipse. Volume average strain response (blue line), middle point strain response (red line), and strain responses at points +-50nm from the center (green and purple lines, respectively).

Figure 4-6 Time response of magnetization(a) and strain(b) for the memory bit.

5. Strain-mediated Deterministic Control of 360^o Domain Wall Motion in Magnetoelastic Nanorings

This study provides numerical simulations for deterministic 360^o magnetization rotation of the transverse domain walls in a nickel nano-ring (outer diameter: 500nm, inner diameter: 300nm, and thickness: 10nm) on a PZT thin film (500nm) deposited onto a Si substrate with surface patterned electrodes. Two alternative electrode architectures are studied, namely, a 4-electrode and a 6-electrode configuration. The 4-electrode configuration relies on magnetization dynamics to produce an overshoot coupled with proper timing control of the voltage applied to achieve 360^o magnetization rotation. In contrast, the 6-electrode configuration only requires sequential voltage application to successive pairs of electrodes and thus can be operated at quasi-static speeds and does not rely on magnetization dynamics to achieve 360^o magnetization rotation. These analytical models provide support for developing new devices such as nanoscale multiferroic driven electromagnetic motors.

5.1 Introduction

Considerable research has focused on the control of domain wall (DW) motion for various applications including those related to spintronics devices. Use of external magnetic fields[118] or spin-polarized[119] currents have been experimentally shown to move domain walls in a wide range of devices. More recently, researchers have become interested in multiferroics for controlling/moving DWs/spins due to substantially lower energy requirements (i.e. orders of magnitude lower[120]). However, a rigorous approach to deterministically move a DW has remained elusive due to the symmetry present in magnetoelastic control, i.e. 90^o domain wall movement. Furthermore, rotating a domain wall 360^o in a structure, such as those required in motor applications, has not yet been presented in the literature. If 360^o domain wall motion is possible, this could open several new avenues of study including those related to nanoscale electromagnetic motors that presently do not exist.

Researchers have long understood that magnetic fields move domain walls. For example, Kunz simulated the dynamics of domain wall motion in Permalloy nanowires[121], showing that the domain wall velocity is a function of the external magnetic field. Bryan et al.[122][123] used three dimensional micromagnetics simulations to demonstrate the propagation of transverse domain walls in magnetic nanowires under axial and transverse magnetic fields. S. Glathe et al[124][125]. reported the real time study of field driven DW motion in giant magnetoresistant nanostrips under the influence of both longitudinal and transverse magnetic fields, showing clear evidence that transverse fields influence the DW dynamics below and above the Walker field[126]. While these results are very informative, the generation of a local magnetic field the size of a nanoscale ring is problematic as well as very inefficient in the small scale.

To avoid the use of external magnetic fields spin current controlled domain wall motion has also been experimentally demonstrated in variety of materials including Permalloy and CoFe nano-structures. M. Tsoi et al[127]. measured current-induced domain wall propagation in CoFe stripes by both electrical transport measurements and magnetic force microscopy imaging. Furthermore, Klaui et al[128][129][130]. demonstrated that by injecting a DC current, the magnetic field to displace a head to head domain wall in a nanoscale ferromagnetic permalloy ring structure is decreased or increased depending on the direction of the dc current with respect to the propagation direction of the domain wall. While spin currents can be used to control domain walls this method is also very inefficient and new mechanisms need to be explored.

More recently, researchers have begun to explore multiferroics for moving DW. Strain-mediated multiferroic structures require substantially lower energy compared to spin current methods[45][116]. Roy and Atulasimha[45][116] showed with stochastic Landau-Lifshitz-Gilbert equations that switching can be carried with as little as 1.5 aJ of energy, i.e. orders of magnitude smaller (e.g. 100 fJ) than required in spin current methods. Hu et al[131]. analytically showed strain-induced magnetic domain switching in epitaxial (CFO) thin films. Wang et al[132]. introduced a method for magnetization reversals with electric fields relying on in-plane piezo-strains, magnetic shape anisotropy, and dynamics of ferromagnetic precision to achieve 180^{o} switching. Tiercelin et al[107]. proposed a memory cell concept based on a magnetostrictive element coupled to a piezoelectric substrate and actuated with a two electrodes. Biswas et al[133]. also proposed a low-power writing (~850kT) approach using a similar multiferroic element with two pairs of electrodes similar to a design presented in Cui[113]. Liang et al[134]. numerically demonstrated electric field controlled magnetization switching in a nickel nano-ellipse on a PZT thin film with patterned electrodes showing that substrate clamping can be

overcome. This work followed the experimental efforts of Cui et al[113]. suggesting the use of patterned electrodes to control the magnetic anisotropy in a Ni island on a piezoelectric substrate. There is also experimental data from Hockel et al[135]. and Hyunmin et al[136]. that demonstrate control of transverse domain wall rotation in nickel ring nanostructures with an electric field on a PMN-PT substrate. However, none of these studies demonstrated 360^{o} rotation of a domain wall that is requirement in many futuristic nanoscale applications such as electromagnetic motors.

In this work, numerical simulations are presented for 360^{o} deterministic domain wall motion in a nickel nano-ring on a PZT 500nm thin film with patterned electrodes. Two electrode configurations are presented, i.e., 4-electrode and 6-electrode patterns. The magnetization rotation for both configurations is demonstrated using a fully-coupled micromagnetics and elastodynamics numerical simulation. Results show that with the proper voltage application on the patterned electrodes, the domain wall rotates 360^{o} in the nano-ring.

5.2 Theory

In this section a fully-coupled micromagnetic elastodynamic simulation with piezoelectrics for finite size 3D structures is described. The coupled partial differential equations to be solved as well as the numerical method to simulate a wide range of shape and geometries are provided below. For a more detailed derivation the readers are referred to Ref [137].

The model consists of magnetization dynamics using the Landau-Lifschitz-Gilbert (LLG) equations coupled with the mechanical strains and stresses via the equations of elastodynamics[137]. The piezoelectric response of the thin film is modeled with linear constitutive equations relating strain with the electric field using a quasi-static electric field approximation. Other modeling assumptions include small elastic deformations, linear elasticity, electrostatics, and negligible electrical current contributions. The coupled governing equations used in this work are as follows. The elastodynamics governing equation for mechanical stresses and displacements is [25][31][32][33][97][115]

$$\rho \frac{d\underline{u}^2}{dt^2} = \nabla \cdot \underline{\underline{\sigma}} \tag{5-1}$$

where ρ is the mass density, $\underline{\underline{\sigma}}$ is the stress tensor, $\underline{u}$ is the displacement vector, and t is time.

The dynamics of magnetization is defined by the phenomenological LLG equation[25],

$$\frac{\partial \underline{m}}{\partial t} = -\mu_0 \gamma \left(\underline{m} \times \underline{H}_{eff}\right) + \alpha \left(\underline{m} \times \frac{\partial \underline{m}}{\partial t}\right) \tag{5-2}$$

Where μ_0 is the permeability of free space, γ is the Gilbert gyromagnetic ratio, α is the Gilbert damping constant, and $\underline{m}$ is the normalized magnetization vector. The effective magnetic field, $\underline{H}_{eff}$, includes the external field ($\underline{H}_{ext}$), exchange field ($\underline{H}_{ex}$), demagnetization field ($\underline{H}_{d}$), magnetocrystalline anisotropy field ($\underline{H}_{anis}$), and magnetoelastic field ($\underline{H}_{me}$) effects. Detailed expressions for these terms can be found in the previous chapter[137]. The demagnetization field

is calculated by using the quasi-static Ampere's law. This leads to $\underline{H_d} = -\nabla\varphi$ where $\underline{H}_\mathrm{d}$ is the demagnetization field vector and φ is the potential. Combining this equation with the divergence of magnetic induction equal to zero and the constitutive relation, $\underline{B} = \mu_0(\underline{H} + \underline{M})$, produces the equation for the magnetic potential, φ, in terms of the magnetization[24]. The magnetization is coupled with the effective magnetic field through this demagnetization term.

Substituting the piezoelectric constitutive relations into the elastodynamics equation (4-1) and LLG equations (equation (4-2)) produces a cross-coupled set of non-linear equations containing displacements, magnetization, electrical field, and magnetic potential as follows [25][31][32][33][97][115] (Detail derivation in Chapter 3. [137].):

$$\rho\frac{d\underline{u}^2}{dt^2} - \nabla\cdot\underline{\underline{\underline{C}}}\left[\frac{1}{2}\left(\nabla\underline{u} + \left(\nabla\underline{u}\right)^T\right)\right] + \nabla\cdot\underline{\underline{\underline{C}}}\left[\underline{\underline{\underline{\lambda}}}^m\underline{mm}^T\right] + \nabla\cdot\underline{\underline{\underline{C}}}\left(\underline{\underline{dE}}\right) = 0 \qquad (5\text{-}3)$$

$$\frac{\partial\underline{\underline{m}}}{\partial t} = -\mu_0\gamma\left(\underline{m}\times\left(\underline{H}_{ext} + \underline{H}_{ex}(\underline{m}) + \underline{H}_d(\varphi) + \underline{H}_{ani}(\underline{m}) + \underline{H}_{me}\left(\underline{m},\underline{u}(\underline{E})\right)\right)\right) + \alpha\left(\underline{m}\times\frac{\partial\underline{\underline{m}}}{\partial t}\right) \quad (5\text{-}4)$$

$$\nabla^2\varphi = M_s(\nabla\cdot\underline{m}) \qquad (5\text{-}5)$$

where $\underline{\underline{\underline{C}}}$ is the stiffness tensor and $\underline{\underline{\underline{\lambda}}}^m$ is the magnetostriction tensor. $\underline{E}$ is the electric field vector, and $\underline{\underline{d}}$ is the piezoelectric coupling tensor[25][31][32][33][97][115].

In a similar fashion to magnetic potential, the quasi-static Faraday's Law implies that $\underline{E} = -\nabla V$, where V is the electric potential. This equation coupled with Gauss's Law and provides the piezoelectric coupling within the model. These coupled systems of partial differential equations are solved for the mechanical displacement (u, v, w), electric potential (V), magnetic potential (φ), and magnetization (m_x, m_y, m_z).

The numerical solution of micro-magneto-electro-mechanical coupled equations is obtained by using a finite element formulation (COMSOL) with an implicit backward differentiation (BDF) time stepping scheme[100][102]. In order to decrease solution time, the system of equations is solved simultaneously but using a segregated method, which splits the solution process into sub-steps using a damped Newton's method[102]. This coupled model provides dynamic results for the full strain and micromagnetic spin distribution in the magnetoelastic component coupled with a piezoelectric layer. For all numerical problems, convergence studies (i.e., mesh size and time steps) were evaluated to ensure accuracy. Additionally, this model has been experimentally validated for ring structures on the thick PMN-PT substrate[136] as well as on nanoscale structure[134].

5.3 Simulation Setup

Figure 5-1 shows the two magnetoelastic nickel nano-ring configurations studied in this chapter, i.e. a 4-electrode pattern and a 6-electrode pattern. The Ni nano-ring dimensions are outer diameter 500 nm, inner diameter 300 nm and 10 nm thickness. The nano-ring is perfectly adhered to a 500 nm PZT-5H deposited onto a Platinum ground electrode on top of a 0.5mm thick Si/SiO2 Substrate. The PZT-5H is poled vertically downward. Each of the two configurations contains Au electrodes with dimensions of 330 nm x 330 nm x 10 nm. The electrodes are 500nm apart from the center of the nano-ring. The entire model containing the ring, electrodes, piezoelectric, and air has X-Y-Z dimensions of 2500nm x 2500nm x1000nm.

Figure 5-1 (a) shows the 4-electrode configuration consists of two pairs (A-A and B-B) of electrodes 90^{o} apart from each other. Figure1 (b) shows the 6-electrode configuration with three sets of electrode pairs A-A, B-B, and C-C that are 60^{o} apart from each other. The objective of this simulation is to apply a positive voltage to a set of electrode pairs (e.g. A-A, B-B or C-C) to produce rotation of the transverse domain walls in the Ni nano-ring using the principle of magnetoelasticity, i.e. strain-mediated multiferroics. To represent the Si substrate, the bottom surface of the PZT film is clamped with zero displacement. The four sides defining the boundary of the modeled structure (i.e. 2500nmx2500nm) are also clamped representing an infinite in-plane structure. The bottom surface is electrically grounded and a 1V signal is applied to the Au electrodes; that is the electric field is applied through the PZT-5H film thickness. A d_{33}-related out-of-plane deformation is generated with the application of voltage on the electrode pair. This out-of plane deformation produces in-plane anisotropic strain in the nickel nano-ring as shown in Figure 5-2. This anisotropic strain mechanism to control magnetic spin states has

been experimentally demonstrated on a bulk PZT sample, as described by Cui[113]. For this electrode/PZT film geometry the capacitance for each electrode can be calculated using the finite element program. The amount of charge required to produce a 1V potential on each electrode, shown in Figure 5-3 and Figure 5-4, is approximately $40x10^{-15}$ (Coulomb). This yields a capacitance of approximately 40 (femtoFarad). In this chapter the voltage is applied in 3 nano-seconds which is appropriate charging time to reach the 1V for this capacitance.

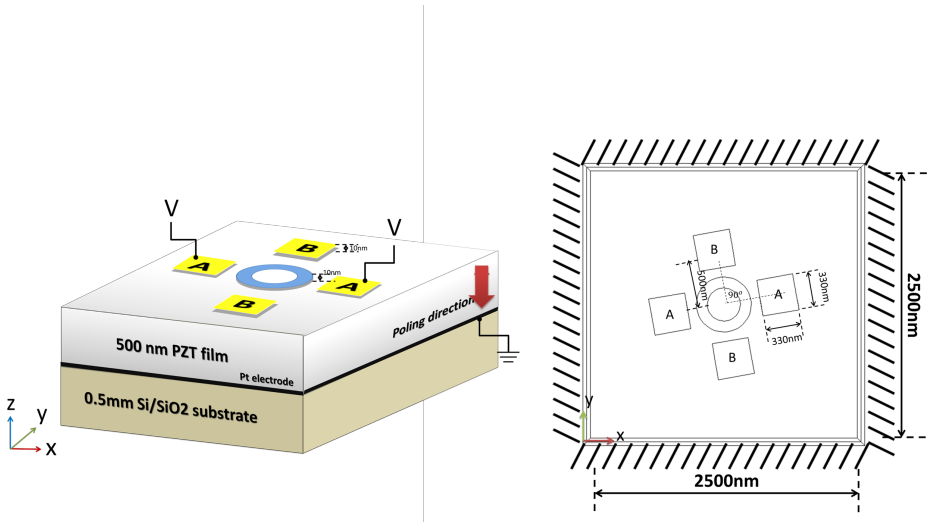

(a) 4-electrode configuration

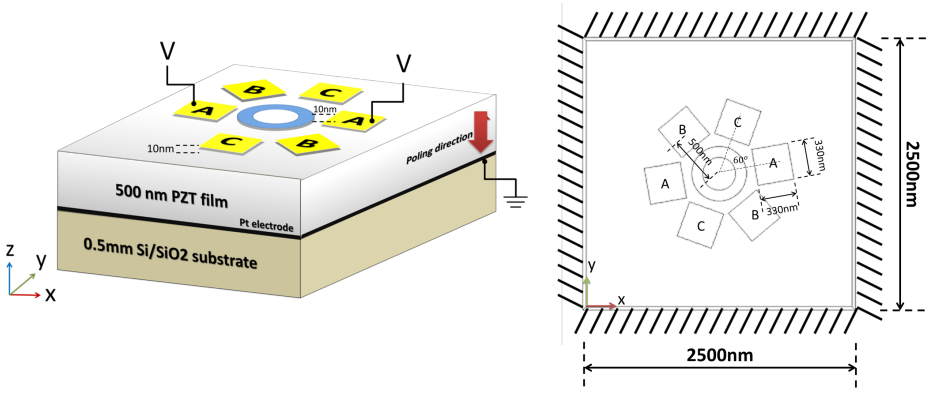

(b) 6-electrode configuration

Figure 5-1 (Color) Schematic plot.

(a) Schematic plot of the electric control nano-ring with 4 patterned electrodes and the boundary conditions.
(b) Schematic plot of the electric control nano-ring with 6 patterned electrodes and the boundary conditions.
(Boundary conditions: All four boundary conditions around the PZT film for both configurations are fixed)

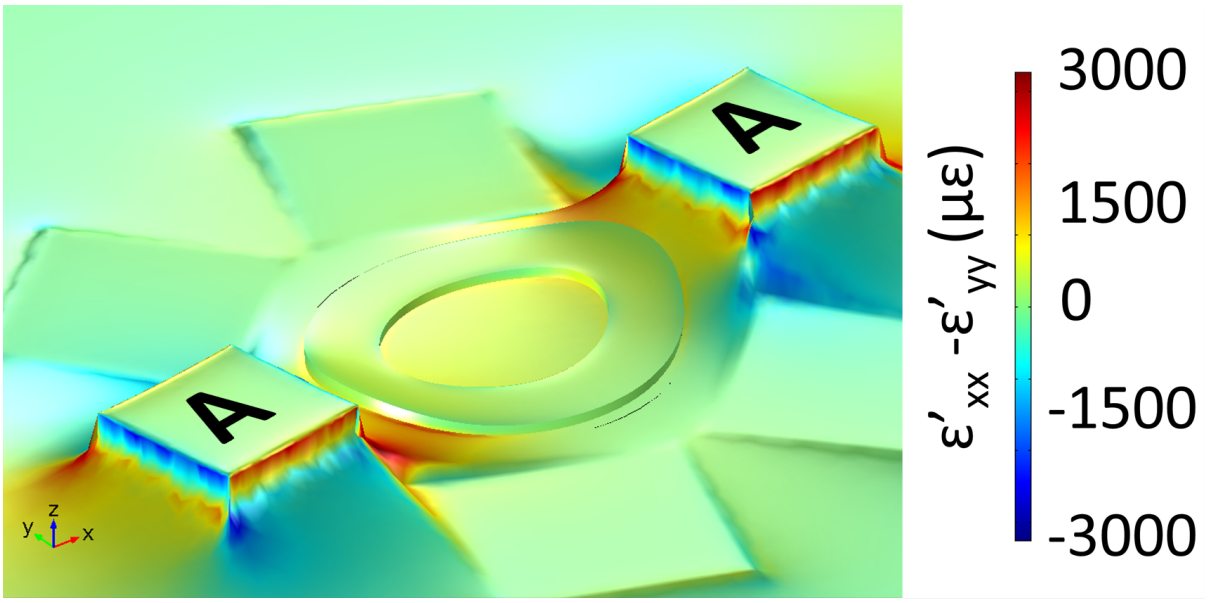

Figure 5-2 (Color) Deformation of the PZT film when voltage is applied.

The material properties used follows. The material properties for the nickel nano-ring are[97] $M_s = 4.8\times10^5(A/m)$, $A_{ex} = 1.05\times10^{-11}(J/m)$, $\lambda_{100} = -46\times10^{-6}$, $\lambda_{111} = -24\times10^{-6}$, $c_{11} = 2.5\times10^{11}(N/m^2)$, $c_{12} = 1.6\times10^{11}(N/m^2)$, $c_{44} = 1.18\times10^{11}(N/m^2)$. The nickel nano-ring is assumed polycrystalline with weak magnetocrystalline anisotropy compared to the other magnetic anisotropies and is thus neglected. The Gilbert damping ratio is set as α=0.08 to improve stability and process time. The PZT-5H material properties are[102] $d_{33} = 5.93\times10^{-10}(C/N)$, $d_{31} = -2.74\times10^{-10}(C/N)$, $c_{11} = c_{22} = 1.27205\times10^{11}(N/m^2)$, $c_{12} = 8.02\times10^{10}(N/m^2)$, $c_{13} = c_{23} = 8.46\times10^{10}(N/m^2)$, $c_{33} = 1.17\times10^{11}(N/m^2)$, $c_{44} = c_{55} = 2.29885\times10^{10}(N/m^2)$, and $\rho = 7500(kg/m^3)$. The Young's modulus and Poisson's ratio for Au are $E^{Au} = 7\times10^{10}(N/m^2)$, and $\nu^{Au} = 0.44$, respectively[102]. The nickel nano-ring is discretized using tetrahedral elements with a size on the order of nickel's exchange length calculated as $\sqrt{\frac{2A_{ex}}{\mu_0 {M_s}^2}} \sim 8.5(nm)$. The remainder of the structure (i.e., PZT-5H thin film, Au electrodes, and Air) is discretized using tetrahedral elements with graded element sizes dependent upon local geometry[102].

5.4 Simulation Results

The voltage control mechanism to produce 360^o domain wall motion in the 4-electrode pattern and the 6-electrode pattern are described below. Results demonstrate deterministic control in both cases however the 6-electrode pattern provides a more robust control approach as compared to the 4-electrode pattern. That is the 4-electrode pattern relies on domain wall dynamics to produce a deterministic 360^o rotation which is not required in the 6-electrode pattern.

Figure 5-3(a)-(o) show results from the 4-electrode pattern producing a 360^o rotation of the magnetic transverse domain walls with the application of voltage on electrode pairs. The first column of figures, Figure 5-3(a)-(e), provide color contour plots of the voltage applied to electrode pairs either A-A or B-B at different times. The second column of figures, Figure 5-3 (f)-(j), show the ring's magnetic state via contour plots and arrows. The in-plane components (m_x and m_y) are represented by the surface arrows while the out-of-plane magnetization component (m_z) is represented by the color scale. These figures were generated from their corresponding sequence position shown in the first column, i.e. Figure 5-3(a)-(e). The third column of figures, Figure 5-3(k)-(o), provide color contour plots of the relative strains (ε'_{AA} - ε'_{BB}) in the ring and substrate during voltage application while the large red and blue arrows provide average principle strain directions over the entire Ni ring structure. The first row of figures, i.e. Figure 5-3(a), (f) and (k), represent the magnetization/strain state at the moment the voltage is applied to electrodes A-A, i.e. prior to the domain wall responding to the applied electric field. The magnetization is initially in an onion state along the +x-direction and transverse domain walls form at 0^o/180^o in the nano-ring. Here it is important to point out that the onion state is shifted 10^o with respect to the A-A electrodes. This offset is required to

produce deterministic clockwise rotation. When electrode A-A pair is energized as shown in Figure 5-3(a), a tensile in-plane principle strain is induced along the A-A direction and a compressive principle strain is generated along the B-B direction (shown in Figure 5-3 (k)). These strains provide the driving force for the magnetization which moves the onion state to a new more energetically favorable state at approximately -80^{o} relative to the x axis as shown in Figure 5-3 (g). The two transverse domains that define the onion state, shown in Figure 5-3 (a) and Figure 5-3 (f), are driven by the strains (Figure 5-3 (k)) and these two transverse domains rotate simultaneously clockwise to -80^{o} and $+100^{o}$ respectively where they align to the compressive principle strain direction as shown in Figure 5-3 (g) and Figure 5-3 (l). The key issue for this mechanism to work in a continuous manner is to properly choose the timing at which the first pair of electrodes A-A is turned off and the second pair of electrodes B-B is turned on. This timing is accomplished by allowing the onion state to dynamically overshoot the compressive principle strain (at ~ -80^{o} and $+100^{o}$) as shown in Figure 5-3 (l) and will be described in more detail in the next paragraph[138]. When electrodes B-B is turned on, tensile principle strains are induced along the B-B direction and compressive principal strains along the A-A direction as shown in Figure 5-3 (m). The elastic energy induces an easy axis at ~ -170^{o} and $+10^{o}$ which drives the two transverse domain walls to rotate toward ~ $-170^{o}/+10^{o}$ (shown in Figure 5-3 (h) and (m)), which is the energetic favorable direction. If the voltage applications described above is now repeated for A-A, the corresponding induced strain will drive the two domains from ~ $-170^{o}/+10^{o}$ to -260^{o} /+80 as shown in Figure 5-3 (n), with the caveat that timing must be considered when applying the electric field (see next paragraph). Finally, when voltage is applied to electrode pairs B-B (as shown Figure 5-3 (e)), the two domain wall rotates from -

260^{o} /+80 to $-350^{o}/170^{o}$ as shown in Figure 5-3 (j) and (o) and thus produce transverse domain wall motion around the entire periphery of the ring.

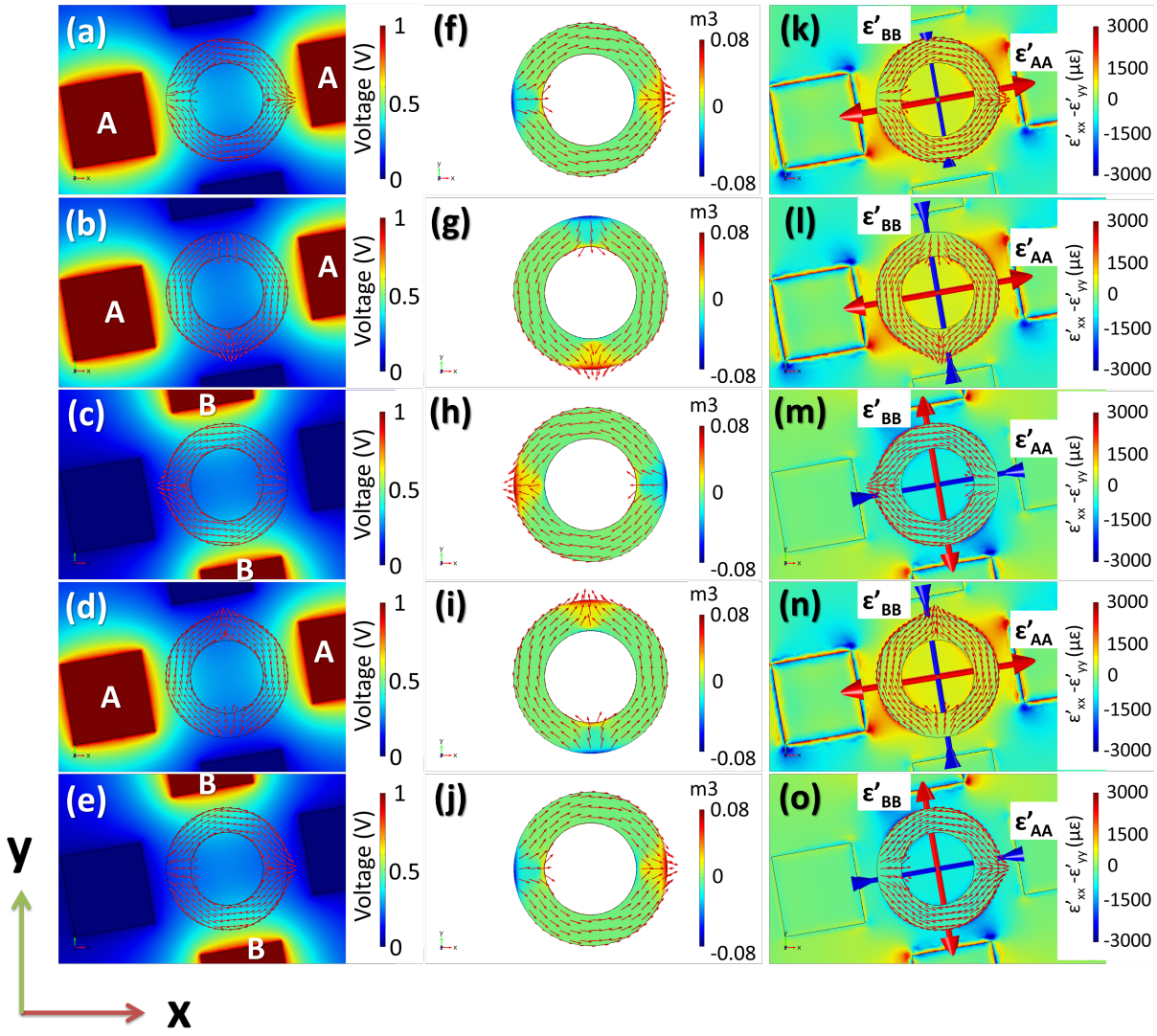

Figure 5-3 (Color) Mechanism of the 360^{o} rotation with 4 patterned electrodes

(a)-(e) Voltage applied on electrode pairs A-A and B-B.
(f)-(j) In-plane transverse domain wall (arrows) and magnetization (m_z) component (color).
(k)-(o) Principle strain directions due to the sequential voltage application on A-A and B-B.

Figure 5-4 shows the voltage applied to the electrodes (A-A or B-B) as well as the average magnetization angle as a function of time for the results described in Figure 5-3. The average in-plane magnetization angle is defined by $\theta = tan^{-1}\left(\frac{m_y}{m_x}\right)$ where m_x and m_y are averaged over the entire nano-ring volume. At time zero the magnetization angle is along the 0^o direction and the positive voltage of 1V is applied to electrode A-A at $time = 0$ sec. This time is representative of Figure 5-4 (a) where the voltage is applied but the initial magnetization is along the 0^o direction. The positive voltage (1V) is applied to electrode A-A for 3.5×10^{-9} sec which causes the magnetization to rotate to ~-83°. This represents approximately ~3° overshoot from the magnetoelasetically driven domain motion which is attributed to spin precession previously used for 180° switching. As can be seen in Figure 5-4, the magnetization rotational speed is variable during this time period. The magnetization angle initially accelerates during the initial 2×10^{-9} sec and slows down during the remainder 1.5×10^{-9} sec. This is because an easy axis is generated perpendicular to the A-A direction (shown in Figure 5-3 (l)) and the domain wall is falling down the slope of the energy gradient when A-A is energized producing non-uniform rotational speeds. Sequentially, at $time = 3.5\times10^{-9}$ sec, the voltage on electrode A-A is removed and the voltage on B-B is turned on. Here it is important to point out that the magnetization angle overshoots the compressive principle strain direction by approximately ~3 degree. To better see this overshoot Figure 5-4 (b) shows the magnetization rotation between $time = 2.5\times10^{-9} sec \; and \; time = 4.5\times10^{-9} \; sec$ in an expanded scale. The red line represents the magnetization rotation when the voltage is properly energized on electrode pair B-B while the gray dash line shows the magnetization rotation when the voltage on A-A is turned off and voltage is not applied to electrode pair B-B. First as can be seen in Figure 5-4, the magnetization overshoots the angle to approximately ~-83° and begins to return to ~-80° due to spin precession

to the energy minimum. If voltage is not applied to B-B, one can see from the gray curve that the magnetization precesses about ~-80^{o} where only one precession is presented. However, if electrode pair B-B is energized at the appropriate overshoot time interval (between $time = 3\times10^{-9} sec\ to\ time = 4\times10^{-9}\ sec$) following voltage removal from electrode pair A-A, the magnetization continues to rotate deterministically toward ~-170^{o}. Returning to Figure 4, if this process is repeated and also that the timing of the voltage is properly applied; the magnetization rotates the entire 360^{o} clockwise around the ring. However, if the voltage applied to a successive pair of electrodes is not timed appropriately deterministic 360^{o} rotation will not be achieved in this 4-electrode design.

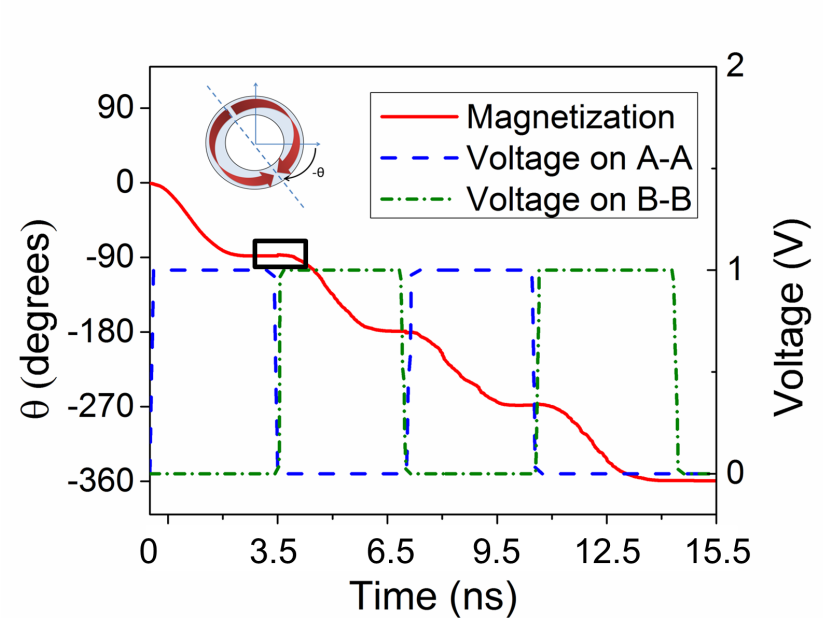

(a)

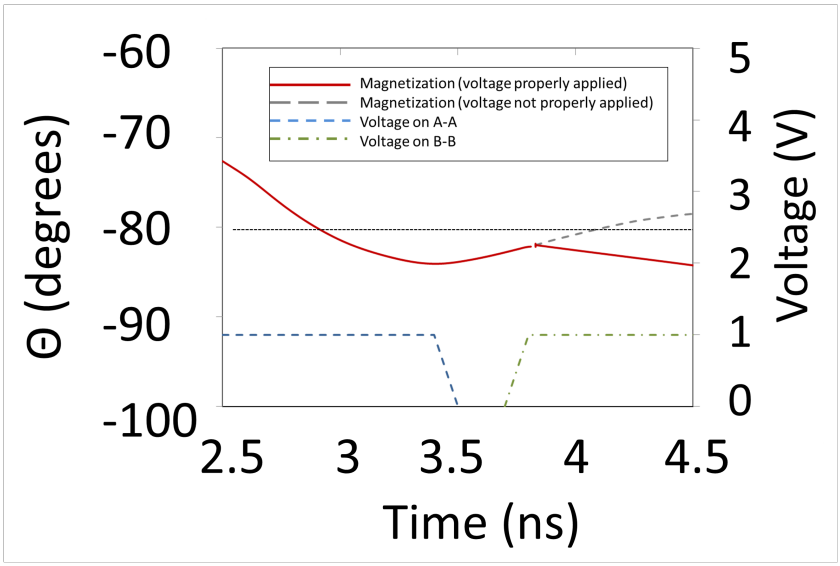

(b)

Figure 5-4 (Color) Time response of the domain wall reorientation for 4-electrode configuration.

(a) Total time period
(b) Zoom in from figure 4(a) (black box).Time period between 2.5ns and 4.5ns.

Figure 5-5 shows the results for the magnetic transverse domain wall rotation in the nano-ring with a 6-electrode pattern. The arrows, colors, and principle strain direction were previously defined in Figure 5-3 discussions and are not repeated here. Figure 5-5 (a)(e)(i) show the initial state right before the voltage is applied. The magnetization is an onion state with a 20^o shift of the electrode pair relative to A-A direction (10^o shift with respect to x-direction). Figure 5-5 (b)-(d) and Figure 5-5 (f)-(h) show the voltage application process and domain rotation when voltage is applied on electrode pairs A-A or B-B. When the electrode A-A pair is energized, due to out-of-plane expansion, tensile strain is induced along the A-A direction and compressive strain is generated perpendicular to A-A direction (shown in Figure 5-5 (j)), which produces energetic favorable direction between A-A and B-B. The two transverse domains rotate simultaneously clockwise to $\sim$-75^o/105^o as shown in Figure 5-5 (c) and (g). Now, electrode pair A-A is turned off and electrode pair B-B is energized, tensile strain is induced along the B-B direction and compressive strain is generated perpendicular to B-B direction (shown in Figure 5-5 (k)) and spins are reoriented by the strain. The two domains then rotate to $\sim$-125^o/55^o, which is the energetic favorable direction as shown in Figure 5-5 (d), (h) and (l). By sequentially applying voltage on electrode pairs (A-A >> B-B >> C-C>>A-A…and so on.), the domains will rotate 360^o clockwise around the ring. Moreover, by applying voltage on the specific electrode pairs, the domain wall motion can be rotated deterministically (i.e., counterclockwise or clockwise).

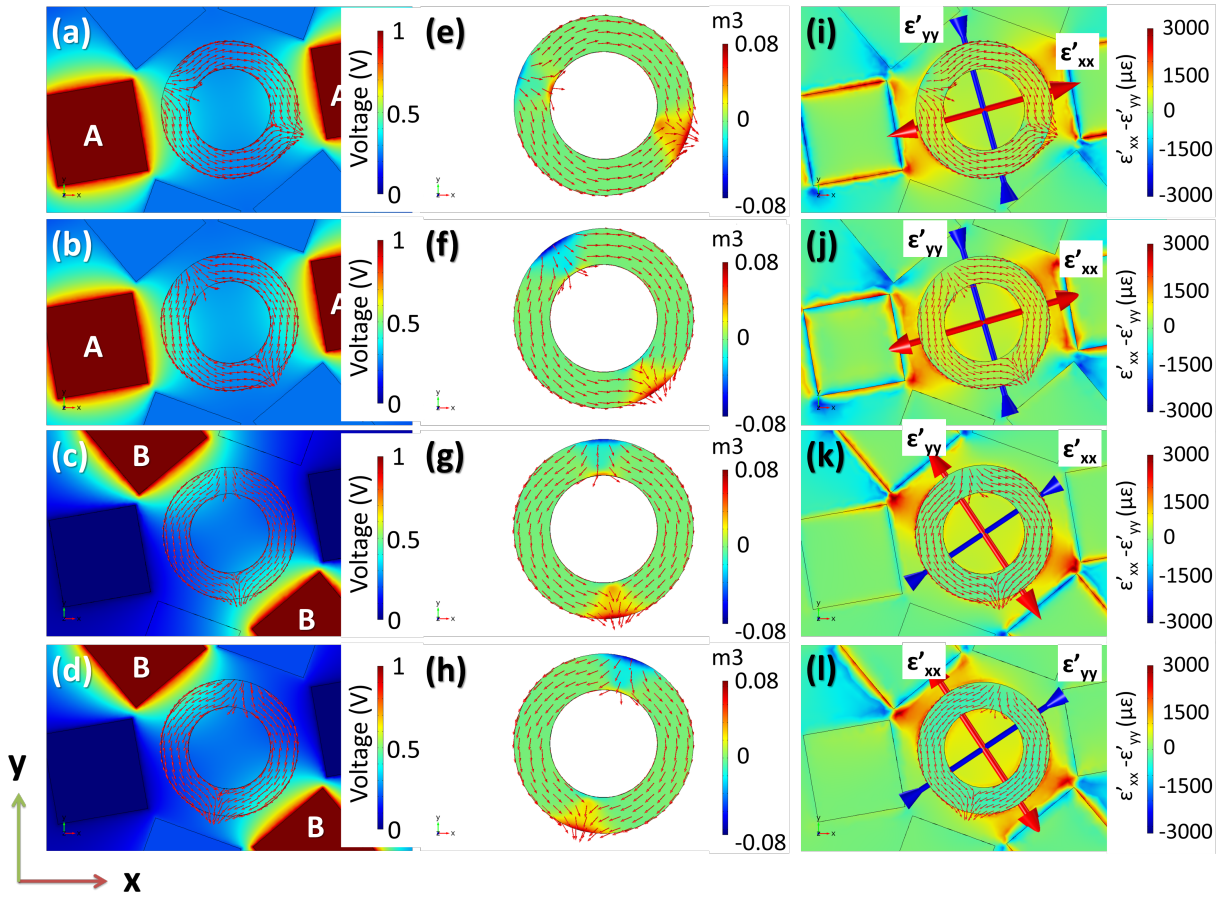

Figure 5-5 (Color) Mechanism of domain reorientation with 6 patterned electrode design.

(a)-(d) Sequential Voltage application to A-A and B-B. (a) Initial state in the nano-ring right at the voltage (A-A) is applied.
(e)-(h) domain wall (arrow) and magnetization component (m_z) reorientation plot (in color) due to electrode pair A-A or B-B energized.
(i)-(l) Principle strain directions when voltage is applied to A-A or B-B.

Figure 5-6 shows the temporal response of the magnetization angle for the 6-electrode configuration and the first two voltage cycles. The transverse domain wall starts at -20^{o} offset with respect to the x-direction (20^{o} shift with respect to A-A) and a positive voltage (1V) is applied to electrode pair A-A at $time = 0$ sec and the voltage is applied for 5.5×10^{-9} sec. Note that this time period is longer than that presented for the 4-electrode pattern shown in Figure 5-4. The magnetization in Figure 5-6 starts to rotate to -75^{o} at $time = 0$ sec. The speed of rotation is not constant and we observe a similar behavior as in the 4-electrode case. The rotation accelerates in the first 1×10^{-9} sec period and slows down in the following 4.5×10^{-9} sec period. Here it is important that the precsssion at this time period has completed such that the -75 angle represents the minimum energy well rather than that presented in Figure 5-4. The voltage on electrode A-A is removed at $time = 5.5\times10^{-9}$ sec and then the voltage on B-B is turn on at $time = 6\times10^{-9}$ sec. Here note that there is a purposely designed longer delay time (i.e. 0.5×10^{-9} sec demonstrating that timing is unimportant in this design. The voltage period for B-B is again 5.5×10^{-9} sec. The magnetization rotates from -75^{o} to about -125^{o}. Therefore, these results show that it is unnecessary to time the application of the voltage to produce continuous rotation of the transverse domain walls around the rings periphery as was required in the 4-electrode pattern.

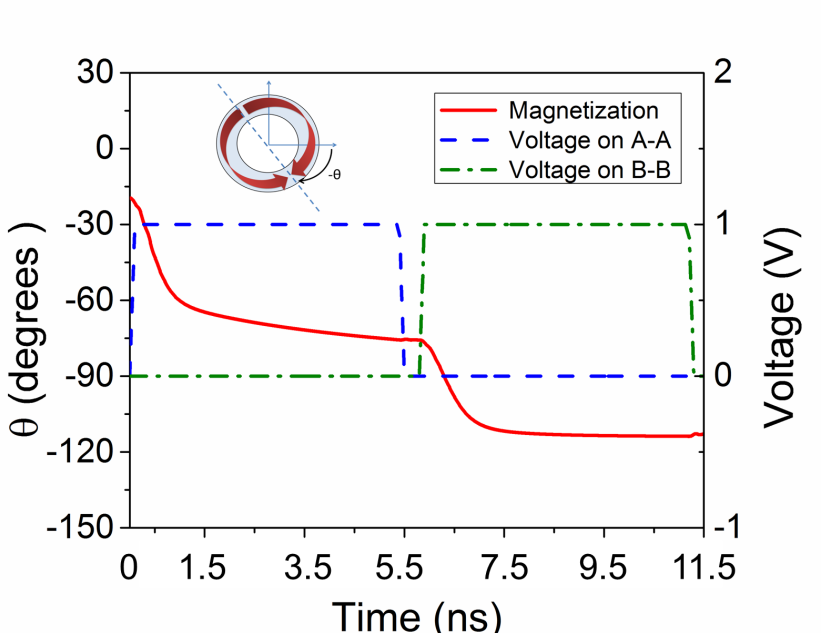

Figure 5-6 (Color) Time response of the domain wall reorientation for 6-electrode pattern.

5.5 Conclusion

In conclusion, this study presents a mechanism to deterministically rotate transverse domain 360^{o} in a nickel nano-ring on a PZT thin film with patterned electrodes. Two electrode configurations were presented, 4-electrode and 6-electrode configurations. The 4-electrode pattern configuration relies on proper voltage control and overshoot while 6-electrode pattern does not. The magnetization control for both configurations is demonstrated using a fully-coupled numerical simulations. Analytical results show that with the sequential application of voltage on the patterned electrodes, the transverse domain is able to be rotated 360^{o} in the nano-ring. This represents a potential nano-motor application. In this study the electrode configurations and voltage applications were not optimized. From Figure 5-4 and Figure 5-6, we observe that a better control law is needed to achieve smooth 360^{o} rotation or to obtain a given torque and/or angular speed. The non-uniform angular speed of the domain wall can be improved in an open loop on/off type of control for the electrode pairs by optimizing the switching time for the control law as well as the shape of the pulse. The main drawback of the open loop control law is that any uncertainty present in that actual device cannot be taken into account in the control voltage law. In particular, the presence of geometry imperfections and roughness due to manufacturing will have a significant impact on the angular speed and cause magnetization pinning. For a more robust control of the rotational speed, a feedback control approach may be required. In particular, this feedback control approach could help overcome imperfections or other disturbances at the cost of implementing a sensing mechanism.

6. Conclusion and Future Works

6.1 Conclusion

In summary, a theoretical methodology for micromagnetic-mechanical-electric modeling was developed in this dissertation. With accurate models, we were able to study multiferroic devices. Optimized design parameters and material properties were validated by experimental results. Some devices which were accurately modeled include strain-mediated magnetic random-access memory (MeRAM), and nano-motors.

In Chapter 1. , a brief introduction was given for current literature. Some of the work that was reviewed include the Stoner–Wohlfarth model for single domain small particles, the Landau-Lifhsitz-Gilbert (LLG) Equation for magnetization equilibrium states, and the stress-induced anisotropy analysis method (LLG+Elastodynamics), among other works. From these studies, the idea to develop a fully-coupled micromagnetic model was a driving force behind this dissertation.

In Chapter 2. , an analytical work was presented to significantly improve simulation of finite structures by fully coupling LLG with elastodynamics, i.e. the seven partial differential equations were intrinsically coupled. Material properties influenced by mechanical strains/stresses (e.g., M-H hysteresis curves, coercivity, and magnetic domains) were initially investigated with a magnetic-mechanical-electric fully-coupled model. The simulated results had good agreement with the experimental data as compared to the conventional Stoner–Wohlfarth model. This model was also validated by experiments, showing that it can be used in designing multiferroic devices.

In Chapter 3. , the robust analytical model combining micromagnetics with elastodynamics and electrostatics was applied to design a strain-mediated, bi-stable state multiferroic memory (MeRAM). The solution was implemented in a finite element code providing both spatial and temporal information on the magnetic, electric, and mechanical fields. A single domain magnetoelastic elliptical nano-structure, bonded to a clamped piezoelectric thin film with patterned electrodes, was studied. By applying electric field to patterned electrodes, out-of-plane deformations produced sufficient in-plane strain to overcome the classical substrate clamping and to switch magnetization between two stable states.

In Chapter 4. , a fully coupled analytical model between elastodynamics with micromagnetics is used to study the switching energies using voltage induced mechanical bending of a magnetoelastic bit. The bit consists of a single domain magnetoelastic nano-ellipse deposited on a thin film piezoelectric thin film (500 nm) attached to a thick substrate (0.5mm) with patterned electrodes underneath the nano-dot. A voltage applied to the electrodes produces out of plane deformation with bending moments induced in the magnetoelastic bit modifying the magnetic anisotropy. To minimize the energy two design stages are used. In the first stage, the geometry and bias field (H_b) of the bit are optimized to minimize the strain energy required to rotate between two stable states. In the second stage, the bit's geometry is fixed and the electrode position and control mechanism is optimized. The electrical energy input is about 200 (aJ) which is approximately two orders of magnitude lower than spin transfer torque approaches.

In Chapter 5. , a novel mechanism to deterministically control of magnetization 360^o rotation was demonstrated. The device was a nickel nano-ring on a PZT thin film with patterned electrodes. Two electrode configurations were shown, then 4-electrode and 6-electrode configurations were also tested. The 4-electrode pattern configuration relies on proper voltage

control and overshoot while 6-electrode pattern does not. The magnetization rotation for both configurations was demonstrated in this chapter. With the proper voltage application on the patterned electrodes, the magnetic domain rotates 360^{o} in the nano-ring, giving a potential multiferroic nano-motor application.

6.2 Future Works

In this dissertation, a fully-coupled micromagnetic with elastodynamics model was developed. This opens new research areas in strain-mediated multiferroic devices. There are several research areas arising from this study using the fully-coupled micromagnetic model.

First, we have deeply studied nickel-based memory devices. The energy dissipation in these devices is about 1fJ. The goal for those multiferroic In this work, we have deeply studied nickel-based memory devices. The energy dissipation in those devices is about 1fJ. The goal energy dissipation for strain-mediated multiferroic devices is down to 10aJ. Other materials, such as Terfenol-D, CoFe, FeGa, have relatively higher magnetoelastic coefficients than nickel, which help to improve the power consumption and efficiency. While using new materials, other issues may occur, for example, the electric control of magnetization, residual strain effects, and equilibrium states will change, thus, the physics needs to be studied deeply in the future.

Second, we have already figured out a way to reversibly rotate the magnetization in ring nanostructures with 4 or more patterned electrodes. However, problems rise when we are trying to fabricate the nanostructures. Therefore, we can take advantages of shape anisotropy, surface anisotropy, and strain-induced anisotropy to optimize the design using the fully-coupled model in order to reduce the complexity of the patterned electrodes and successfully fabricate a device.

Third, the model is able to capture the strain-induced dynamics of magnetization in ferromagnetic materials. In addition, the model is built on a customizable software, new physics can be added in the model to study the strain-mediated spin wave interactions, skyrmions, and strain-assist spin-transfer torque. Thus, this model can be easily modified in the future to accommodate the changes in physics for multiferroic devices of the future.

7. References

[1] H. Schmid, "Multi-ferroic magnetoelectrics," Ferroelectrics 162, 317.

[2] M. Fiebig,"Revival of the magnetoelectric effect," J. Phys. D 38, R123, 2005.

[3] A. K. Zvezdin, A. S. Logginov, G. A. Meshkov, A. P. Pyatakov, "Multiferroics: Promising materials for microelectronics, spintronics, and sensor technique," Bulletin of the Russian Academy of Sciences: Physics, Volume 71, Issue 11, pp 1561-1562, Nov. 2007.

[4] Manuel Bibes and Agnès Barthélémy, " Multiferroics: Towards a magnetoelectric memory," Nature Materials 7, 425 -426, 2008.

[5] H Béa, M Gajek, M Bibes and A Barthélémy, “Spintronicswith multiferroics," J. Phys.: Condens. Matter 20 434221.

[6] Th. Gerrits, H. A. M. van den Berg, J. Hohlfeld1, L. Bär and Th. Rasing, "Ultrafastprecessional magnetization reversal by picosecond magnetic field pulse shaping," Nature 418, 509-512, August 2002.

[7] S. M. Wu, Shane A. Cybart,P. Yu, M. D. Rossell, J. X. Zhang,R. Ramesh and R. C. Dynes, "Reversible electric control of exchange bias in a multiferroic field-effect device," Nature Materials 9, 756–761, July 2010.

[8] Martin Weisheit, Sebastian Fähler, Alain Marty, Yves Souche, Christiane Poinsignon, Dominique Givord, "Electric Field-Induced Modification of Magnetism in Thin-Film Ferromagnets," Science 19, Vol. 315 no. 5810 pp. 349-351, January 2007.

[9] M. Overby, A.Chernyshov, L.P. Rokhinson, X. Liu, "GaMnAs-based hybrid multiferroic memory device," Applied Physics LettersVol.92 , Iss. 19), pp. 192501 -192501-3, May 2008.

[10] Stoner & Wohlfarth 1948.

[11] C. Tannous and J. Gieraltowski, "The Stoner-Wohlfarth model of ferromagnetism," European Journal of Physics, vol. 29, pp. 475-487, May 2008.

[12] E. Bonet,W. Wernsdorfer, B. Barbara, A. Benoıt, D. Mailly, and A. Thiaville, "Three-Dimensional Magnetization Reversal Measurements in Nanoparticles," Phy. Rev. Lett., vol. 83, pp. 4188-4191, Nov. 1999.

[13] L. Callegaro and E. Puppin,"Rotational hysteresis model for stressed ferromagnetic films," Ieee Transactions on Magnetics, vol. 33, pp. 1007-1011, Mar 1997.

[14] M. J. Sablik and D. C. Jiles, "A modified Stoner-Wohlfarth computational model for

hysteretic magnetic properties in a ferromagnetic composite rod under torsion," Journal of Physics D-Applied Physics, vol. 32, pp. 1971-1983, Aug 21 1999.

[15] Z. Szabo and A. Ivanyi, "Computer-aided simulation of Stoner-Wohlfarth model," Journal of Magnetism and Magnetic Materials, vol. 215, pp. 33-36, Jun 2000.

[16] B. Peng, W. L. Zhang, W. X. Zhang, H. C. Jiang, and S. Q. Yang, "Effects of stress on the magnetic properties of the amorphous magnetic films," Physica B-Condensed Matter, vol. 382, pp. 135-139, Jun 15 2006.

[17] F. Izawa, "Theoretical-Study on Stress-Induced Demagnetization in Magnetic Recording Media," Ieee Transactions on Magnetics, vol. 20, pp. 523-528, 1984.

[18] M. J. Sablik, L. A. Riley, G. L. Burkhardt, H. Kwun, P. Y. Cannell, K. T. Watts, and R. A. Langman, "Micromagnetic Model for Biaxial Stress Effects on Magnetic-Properties," Journal of Magnetism and Magnetic Materials, vol. 132, pp. 131-148, Apr 1994.

[19] D. C. Jiles, "Theory of the Magnetomechanical Effect," Journal of Physics D-Applied Physics, vol. 28, pp. 1537-1546, Aug 14 1995.

[20] L. Callegaro and E. Puppin, "Stress dependence of coercivity in Ni films: Thin film to bulk transition," Applied Physics Letters, vol. 68, pp. 1279-1281, Feb 26 1996.

[21] Y. H. Chen and D. C. Jiles, "The magnetomechanical effect under torsional stress in a cobalt ferrite composite," Ieee Transactions on Magnetics, vol. 37, pp. 3069-3072, Jul 2001.

[22] D. P. Bulte and R. A. Langman, "Origins of the magnetomechanical effect," Journal of Magnetism and Magnetic Materials, vol. 251, pp. 229-243, Oct 2002.

[23] Chaitanya Mudivarthi ; Supratik Datta ; Jayasimha Atulasimha ; Alison B. Flatau ; Phillip G. Evans ; Marcelo J. Dapino, "Equivalence of magnetoelastic, elastic and mechanical work energies with stress-induced anisotropy," Behavior and Mechanics of Multifunctional and Composite Materials, 2008, 69291X (April 02, 2008)

[24] Chikazumi, "Physics of Ferromagnetism," Oxford Science Publications,1997

[25] T. L. Gilbert, "A phenomenological theory of damping in ferromagnetic materials," Ieee Transactions on Magnetics, vol. 40, pp. 3443-3449, Nov 2004.

[26] R. Kikuchi, "On the Minimum of Magnetization Reversal Time," Journal of Applied Physics, vol. 27, pp. 1352-1357, 1956.

[27] Visintin, "On Landau-Lifshitz' equations for ferromagnetism," Japan Journal of Applied Mathematics,vol. 2, Iss. 1, pp. 69-84, June 1985.

[28] J. C. Mallinson, "On Damped Gyromagnetic Precession," Ieee Transactions on

Magnetics, vol. 23, pp. 2003-2004, Jul 1987.

[29] P. A. Voltairas, D. I. Fotiadis, and C. V. Massalas, "Magnetization reversal in thin ferromagnetic films under mechanical stress," International Journal of Engineering Science, vol. 38, pp. 903-919, May 2000.

[30] B. Zhu, C. C. H. Lo, S. J. Lee, and D. C. Jiles, "Micromagnetic modeling of the effects of stress on magnetic properties," Journal of Applied Physics, vol. 89, pp. 7009-7011, Jun 1 2001.

[31] Y. C. Shu, M. P. Lin, and K. C. Wu, "Micromagnetic modeling of magnetostrictive materials under intrinsic stress," Mechanics of Materials, vol. 36, pp. 975-997, Oct 2004.

[32] J. X. Zhang and L. Q. Chen, "Phase-field microelasticity theory and micromagnetic simulations of domain structures in giant magnetostrictive materials," Acta Materialia, vol. 53, pp. 2845-2855, May 2005.

[33] L. Banas, "Numerical methods for the Landau-Lifshitz-Gilbert equation," Numerical Analysis and Its Applications, vol. 3401, pp. 158-165, 2005.

[34] R. L. Hu, A. K. Soh, G. P. Zheng, and Y. Ni, "Micromagnetic modeling studies on the effects of stress on magnetization reversal and dynamic hysteresis," Journal of Magnetism and Magnetic Materials, vol. 301, pp. 458-468, Jun 2006.

[35] J. Dean, M. T. Bryan, G. Hrkac, A. Goncharov, C. L. Freeman, M. A. Bashir, T. Schrefl, and D. A. Allwood, "The incorporation of the Cauchy stress matrix tensor in micromagnetic simulations," Journal of Applied Physics, vol. 108, Oct 1 2010.

[36] Bur, T. Wu, J. Hockel, C. J. Hsu, H. K. D. Kim, T. K. Chung, K. Wong, K. L. Wang, and G. P. Carman, "Strain-induced magnetization change in patterned ferromagnetic nickel nanostructures," Journal of Applied Physics, vol. 109, Jun 15 2011.

[37] J. C. Slonczewski, "Current-driven excitation of magnetic multilayers," Journal of Magnetism and Magnetic Materials, vol. 159, pp. L1-L7, Jun 1996.

[38] L. Berger, "Emission of spin waves by a magnetic multilayer traversed by a current," Physical Review B, vol. 54, pp. 9353-9358, Oct 1 1996.

[39] G. Bertotti, A. Magni, I. D. Mayergoyz, and C. Serpico, "Landau-Lifshitz magnetization dynamics and eddy currents in metallic thin films," Journal of Applied Physics, vol. 91, pp. 7559-7561, May 15 2002.

[40] P Monk, J Sun, "Analysis of an eddy current and micromagnetic model," Applicable Analysis, 2006

[41] R Iyer et al., " Micromagnetics with eddy currents," J. Phys.: Conf. Ser. 268 012011, 2011

[42] W. Eerenstein, M. Wiora, J. L. Prieto, J. F. Scott, and N. D. Mathur, "Giant sharp and persistent converse magnetoelectric effects in multiferroic epitaxial heterostructures," Nature Materials, vol. 6, pp. 348-351, May 2007.

[43] N. A. Pertsev, "Giant magnetoelectric effect via strain-induced spin reorientation transitions in ferromagnetic films," Physical Review B, vol. 78, Dec 2008.

[44] J. Atulasimha and S. Bandyopadhyay, "Bennett clocking of nanomagnetic logic using multiferroic single-domain nanomagnets," Applied Physics Letters, vol. 97, Oct 25 2010.

[45] K. Roy, S. Bandyopadhyay, and J. Atulasimha, "Switching dynamics of a magnetostrictive single-domain nanomagnet subjected to stress," Physical Review B, vol. 83, Jun 22 2011.

[46] M. S. Fashami, K. Roy, J. Atulasimha, S. Bandyopadhyay, and A. Markwitz, "Magnetization dynamics, Bennett clocking and associated energy dissipation in multiferroic logic (vol 22, 155201, 2011)," Nanotechnology, vol. 22, Jul 29 2011.

[47] K. L. Livesey, "Strain-mediated magnetoelectric coupling in magnetostrictive/piezoelectric heterostructures and resulting high-frequency effects," Physical Review B, vol. 83, Jun 27 2011.

[48] Jia-Mian Hu, T. N. Yang, L. Q. Chen, and C. W. Nan, "Voltage-driven perpendicular magnetic domain switching in multiferroic nanoislands," Journal of Applied Physics, vol. 113 19 194301, 2013.

[49] F. Zavaliche, H. Zheng, L. Mohaddes-Ardabili, S. Y. Yang, Q. Zhan, P. Shafer, E. Reilly, R. Chopdekar, Y. Jia, P. Wright, D. G. Schlom, Y. Suzuki, and R. Ramesh, "Electric field-induced magnetization switching in epitaxial columnar nanostructures," Nano Letters, vol. 5, pp. 1793-1796, Sep 2005.

[50] C. Thiele, K. Dorr, O. Bilani, J. Rodel, and L. Schultz, "Influence of strain on the magnetization and magnetoelectric effect in La(0.7)A(0.3)MnO(3)/PMN-PT(001) (A=Sr,Ca)," Physical Review B, vol. 75, Feb 2007.

[51] N. Moutis, D. Suarez-Sandoval, and D. Niarchos, "Voltage-induced modification in magnetic coercivity of patterned Co50Fe50 thin film on piezoelectric substrate," Journal of Magnetism and Magnetic Materials, vol. 320, pp. 1050-1055, Mar 2008.

[52] Brandlmaier, S. Geprags, M. Weiler, A. Boger, M. Opel, H. Huebl, C. Bihler, M. S. Brandt, B. Botters, D. Grundler, R. Gross, and S. T. B. Goennenwein, "In situ manipulation of magnetic anisotropy in magnetite thin films," Physical Review B, vol. 77, Mar 2008.

[53] T. K. Chung, S. Keller, and G. P. Carman, "Electric-field-induced reversible magnetic

single-domain evolution in a magnetoelectric thin film," Applied Physics Letters, vol. 94, Mar 30 2009.

[54] T. K. Chung, K. Wong, S. Keller, K. L. Wang, and G. P. Carman, "Electrical control of magnetic remanent states in a magnetoelectric layered nanostructure," Journal of Applied Physics, vol. 106, Nov 15 2009.

[55] T. Brintlinger, S. H. Lim, K. H. Baloch, P. Alexander, Y. Qi, J. Barry, J. Melngailis, L. Salamanca-Riba, I. Takeuchi, and J. Cumings, "In Situ Observation of Reversible Nanomagnetic Switching Induced by Electric Fields," Nano Letters, vol. 10, pp. 1219-1223, Apr 2010.

[56] Tuomas H. E. Lahtinen,Kévin J. A. FrankeSebastiaan van Dijken, "Electric-field control of magnetic domain wall motion and local magnetization reversal," SCIENTIFIC REPORTS 2 : 258, 2012

[57] S. Geprägsa, Corresponding author contact information, A. Brandlmaiera,M.S. Brandtb,R. Grossa, c,S.T.B. Goennenwein, " Strain-controlled nonvolatile magnetization switching," Solid State Communications

[58] P Gaunt, " Ferromagnetic domain wall pinning by a random array of inhomogeneities," Philosophical Magazine Part B Volume 48, Issue 3, 1983.

[59] Stefano Zapperi, Pierre Cizeau, Gianfranco Durin, H. Eugene Stanley, " Dynamics of a ferromagnetic domain wall: Avalanches, depinning transition, and the Barkhausen effect," Phys. Rev. B 58, 6353–6366 (1998).

[60] Hamrle, J et al. (2007). "Huge quadratic magneto-optical Kerr effect and magnetization reversal in the Co2FeSi Heusler compound". J. Phys. D: Appl. Phys 40: 1563.

[61] Wang, Yu U., Jin, Yongmei M., Khachaturyan, Armen G., "Phase field microelasticity theory and modeling of elastically and structurally inhomogeneous solid," Journal of Applied Physics vol.92 , Iss.3, pp.1351 –1360, Aug 2002

[62] Ce-Wen Nan, M. I. Bichurin, Shuxiang Dong, D. Viehland, and G. Srinivasan, " Multiferroic magnetoelectric composites: Historical perspective, status, and future directions," Journal of Applied Physics J. Appl. Phys. 103, 031101 (2008).

[63] Yao Wang, Jiamian Hu, Yuanhua Lin and Ce-Wen Nan, " Multiferroic magnetoelectric composite nanostructures," NPG Asia Mater. 2 (2) 61–68 (2010)

[64] Chung, J. H., Chung, S. J., Lee, S., Kirby, B. J., Borchers, J. A., Cho, Y. J., . . . Furdyna, J. K. (2008). Carrier-Mediated Antiferromagnetic Interlayer Exchange Coupling in Diluted Magnetic Semiconductor Multilayers Ga(1-x)Mn(x)As/GaAs:Be. Physical Review Letters, 101(23).

[65] Rondinelli, J. M., Stengel, M., & Spaldin, N. A. (2008). Carrier-mediated

magnetoelectricity in complex oxide heterostructures. Nature Nanotechnology, 3(1), 46-50.

[66] Castro, I. L., Nascimento, V. P., Passamani, E. C., Takeuchi, A. Y., Larica, C., Tafur, M., & Pelegrini, F. (2013). The role of the (111) texture on the exchange bias and interlayer coupling effects observed in sputtered NiFe/IrMn/Co trilayers. Journal of Applied Physics, 113(20).

[67] Ziese, M., Bern, F., & Vrejoiu, I. (2013). Exchange bias in manganite/SrRuO3 superlattices. Journal of Applied Physics, 113(6).

[68] Li, Z., & Zhang, S. (2003). Magnetization dynamics with a spin-transfer torque. Physical Review B, 68(2).

[69] Stiles, M. D., & Miltat, J. (2006). Spin-transfer torque and dynamics. Spin Dynamics in Confined Magnetic Structures Iii, 101, 225-308.

[70] Diao, Z. T., Li, Z. J., Wang, S. Y., Ding, Y. F., Panchula, A., Chen, E., . . . Huai, Y. M. (2007). Spin-transfer torque switching in magnetic tunnel junctions and spin-transfer torque random access memory. Journal of Physics-Condensed Matter, 19(16).

[71] Tehrani, S., Slaughter, J. M., Chen, E., Durlam, M., Shi, J., & DeHerrera, M. (1999). Progress and outlook for MRAM technology. Ieee Transactions on Magnetics, 35(5), 2814-2819.

[72] Tehrani, S., Engel, B., Slaughter, J. M., Chen, E., DeHerrera, M., Durlam, M., . . . Calder, J. (2000). Recent developments in Magnetic Tunnel Junction MRAM. Ieee Transactions on Magnetics, 36(5), 2752-2757.

[73] Wang, Y., Hu, J. M., Lin, Y. H., & Nan, C. W. (2010). Multiferroic magnetoelectric composite nanostructures. Npg Asia Materials, 2(2), 61-68.

[74] Nan, C. W., Bichurin, M. I., Dong, S. X., Viehland, D., & Srinivasan, G. (2008). Multiferroic magnetoelectric composites: Historical perspective, status, and future directions. Journal of Applied Physics, 103(3).

[75] Ma, J., Hu, J. M., Li, Z., & Nan, C. W. (2011). Recent Progress in Multiferroic Magnetoelectric Composites: from Bulk to Thin Films. Advanced Materials, 23(9), 1062-1087.

[76] Zhu, B., Lo, C. C. H., Lee, S. J., & Jiles, D. C. (2001). Micromagnetic modeling of the effects of stress on magnetic properties. Journal of Applied Physics, 89(11), 7009-7011.

[77] Hu, R. L., Soh, A. K., Zheng, G. P., & Ni, Y. (2006). Micromagnetic modeling studies on the effects of stress on magnetization reversal and dynamic hysteresis. Journal of Magnetism and Magnetic Materials, 301(2), 458-468.

[78] Jia, Y. M., Or, S. W., Chan, H. L. W., Zhao, X. Y., & Luo, H. S. (2006). Converse magnetoelectric effect in laminated composites of PMN-PT single crystal and Terfenol-D alloy. Applied Physics Letters, 88(24).

[79] Chung, T. K., Keller, S., & Carman, G. P. (2009). Electric-field-induced reversible magnetic single-domain evolution in a magnetoelectric thin film. Applied Physics Letters, 94(13).

[80] Chung, T. K., Wong, K., Keller, S., Wang, K. L., & Carman, G. P. (2009). Electrical control of magnetic remanent states in a magnetoelectric layered nanostructure. Journal of Applied Physics, 106(10).

[81] Weiler, M., Brandlmaier, A., Geprags, S., Althammer, M., Opel, M., Bihler, C., . . . Goennenwein, S. T. B. (2009). Voltage controlled inversion of magnetic anisotropy in a ferromagnetic thin film at room temperature. New Journal of Physics, 11.

[82] Chen, Y. J., Fitchorov, T., Vittoria, C., & Harris, V. G. (2010). Electrically controlled magnetization switching in a multiferroic heterostructure. Applied Physics Letters, 97(5).

[83] Wu, T., Emmons, M., Chung, T. K., Sorge, J., & Carman, G. P. (2010). Influence of mechanical load bias on converse magnetoelectric laminate composites. Journal of Applied Physics, 107(9).

[84] Bai, D. Z., Zhu, J. G., Yu, W., & Bain, J. A. (2004). Micromagnetic simulation of effect of stress-induced anisotropy in soft magnetic thin films. Journal of Applied Physics, 95(11), 6864-6866.

[85] Zou, P., Yu, W., & Bain, J. A. (2002). Effect of stress on stripe domain onset in sputtered FeAlN and CoFe films. Journal of Applied Physics, 91(10), 7830-7832.

[86] Khanna, G., Clemens, B. M., Zhou, H., & Bertram, H. N. (2001). Micromagnetic study of anisotropy sources in textured longitudinal media. Ieee Transactions on Magnetics, 37(4), 1468-1470.

[87] Hu, J. M., Li, Zheng, Chen, L. Q. & Nan,C.W. High-density magnetoresistive random access memory operating at ultralow voltage at room temperature. Nature Communications 2, 553, 2011.

[88] Varga, E., Orlov, A., Niemier, M. T., Hu, X. S., Bernstein, G. H., & Porod, W. (2010). Experimental Demonstration of Fanout for Nanomagnetic Logic. Ieee Transactions on Nanotechnology, 9(6), 668-670.

[89] Liu, S. L., Hu, X. S., Nahas, J. J., Niemier, M. T., Porod, W., & Bernstein, G. H. (2011). Magnetic-Electrical Interface for Nanomagnet Logic. Ieee Transactions on Nanotechnology, 10(4), 757-763.

[90] Chang, C. M., & Carman, G. P. (2007). Modeling shear lag and demagnetization effects in magneto-electric laminate composites. Physical Review B, 76(13).

[91] Alouges, F., & Jaisson, P. (2006). Convergence of a finite element discretization for the Landau-Lifshitz equations in micromagnetism. Mathematical Models & Methods in Applied Sciences, 16(2), 299-316.

[92] Cimrak, I., & Slodicka, M. (2004). An iterative approximation scheme for the Landau-Lifshitz-Gilbert equation. Journal of Computational and Applied Mathematics, 169(1), 17-32.

[93] Carbou, G., Efendiev, M. A., & Fabrie, P. (2011). Global weak solutions for the Landau-Lifschitz equation with magnetostriction. Mathematical Methods in the Applied Sciences, 34(10), 1274-1288.

[94] Miehe, C., & Ethiraj, G. (2012). A geometrically consistent incremental variational formulation for phase field models in micromagnetics. Computer Methods in Applied Mechanics and Engineering, 245, 331-347.

[95] Hubert, A., & Ruhrig, M. (1991). Micromagnetic Analysis of Thin-Film Elements. Journal of Applied Physics, 69(8), 6072-6077.

[96] Cavill, S. A., Parkes, D. E., Miguel, J., Dhesi, S. S., Edmonds, K. W., Campion, R. P., & Rushforth, A. W. (2013). Electrical control of magnetic reversal processes in magnetostrictive structures. Applied Physics Letters, 102(3).

[97] R. C. O'Handley, *Modern Magnetic Material: Principles and Applications* (John Wiley & Sons, Inc, 2000).

[98] E. C. Stoner and E. P. Wohlfarth, Philos Tr R Soc S-A **240**, 599 (1948).

[99] Fredkin, D. R., & Koehler, T. R. (1990). Hybrid Method for Computing Demagnetizing Fields. Ieee Transactions on Magnetics, 26(2), 415-417.

[100] Szambolics, H., Buda-Prejbeanu, L. D., Toussaint, J. C., & Fruchart, O. (2008). A constrained finite element formulation for the Landau-Lifshitz-Gilbert equations. Computational Materials Science, 44(2), 253-258.

[101] Weddemann, D. Kappe, A. Hutten, COMSOL Conference, Boston, MA (2011).

[102] COMSOL Multiphysics: http://www.comsol.com/

[103] Amritendu Roy, Rajeev Gupta, and Ashish Garg, " MultiferroicMemories," Advances in Condensed Matter Physics, vol. 2012, 926290.

[104] T. H. E. Lahtinen, K. J. A. Franke, and S. van Dijken, "Electric-field control of magnetic domain wall motion and local magnetization reversal," Scientific Reports, vol. 2, Feb 10 2012.

[105] N. Pertsev and H. Kohlstedt, “Resistive switching via the converse magnetoelectric effect in ferromagnetic multilayers on ferroelectric substrates.,” Nanotechnology, vol. 21, no. 47, p. 475202, Nov. 2010.

[106] J.-M. Hu, Z. Li, J. Wang, J. Ma, Y. H. Lin, and C. W. Nan, “A simple bilayered magnetoelectric random access memory cell based on electric-field controllable domain structure,” J. Appl. Phys., vol. 108, no. 4, p. 043909, 2010.

[107] N. Tiercelin, Y. Dusch, V. Preobrazhensky, and P. Pernod, “Magnetoelectric memory using orthogonal magnetization states and magnetoelastic switching,” J. Appl. Phys., vol. 109, no. 7, p. 07D726, 2011.

[108] R. Ramesh and N. A. Spaldin, "Multiferroics: progress and prospects in thin films," Nature Materials, vol. 6, pp. 21-29, Jan 2007.

[109] Z. Li, J. Wang, Y. Lin, and C. W. Nan, “A magnetoelectric memory cell with coercivity state as writing data bit,” Appl. Phys. Lett., vol. 96, no. 16, p. 162505, 2010.

[110] G. H. Dai, Q. F. Zhan, H. L. Yang, Y. W. Liu, X. S. Zhang, Z. H. Zuo, B. Chen, and R. W. Li, "Controllable strain-induced uniaxial anisotropy of Fe81Ga19 films deposited on flexible bowed-substrates," Journal of Applied Physics, vol. 114, Nov 7 2013.

[111] T. Wu, A. Bur, H. K. D. Kim, P. Zhao, and G. P. Carman, "Giant electrical control of magnetic anisotropy in magnetoelectric heterostructures using (011) PMN-PT single crystal," Behavior and Mechanics of Multifunctional Materials and Composites 2011, vol. 7978, 2011.

[112] T. Wu, A. Bur, P. Zhao, K. P. Mohanchandra, K. Wong, K. L. Wang, C. S. Lynch, and G. P. Carman, "Giant electric-field-induced reversible and permanent magnetization reorientation on magnetoelectric Ni/(011) [Pb(Mg1/3Nb2/3)O-3]((1-x))-[PbTiO3](x) heterostructure," Applied Physics Letters, vol. 98, Jan 3 2011.

[113] J. Cui, J. L. Hockel, P. K. Nordeen, D. M. Pisani, C. Liang, G. P. Carman, and C. S. Lynch, “A method to control magnetism in individual strain-mediated magnetoelectric islands,” Appl. Phys. Lett., vol. 103, no. 23, p. 232905, 2013.

[114] N. D’Souza, J. Atulasimha, and S. Bandyopadhyay, “Four-state nanomagnetic logic using multiferroics,” J. Phys. D. Appl. Phys., vol. 44, no. 26, p. 265001, Jul. 2011.

[115] B. D. Cullity, and C. D. Graham, “*Introduction to Magnetic Materials*”, Wiley-IEEE Press; 2nd Edition (December 10, 2008)

[116] Kuntal Roy, Supriyo Bandyopadhyay, and Jayasimha Atulasimha, "Energy dissipation and switching delay in stress-induced switching of multiferroic nanomagnets in the presence of thermal fluctuations," Journal of Applied Physics, vol. 112, 023914 (2012).

[117] V. Laukhin, V. Skumryev, X. Martí, D. Hrabovsky, F. Sánchez, M. V. García-Cuenca, C. Ferrater, M. Varela, U. Lüders, J. F. Bobo, and J. Fontcuberta, "Electric-Field Control of Exchange Bias in Multiferroic Epitaxial Heterostructures, "Phys. Rev. Lett. 97, 227201, Nov. 2006.

[118] Forster, H., Schrefl, T., Scholz, W., Suess, D., Tsiantos, V., & Fidler, J., "Micromagnetic simulation of domain wall motion in magnetic nano-wires," Journal of Magnetism and Magnetic Materials, 249(1-2), 181-186 (2002).

[119] Thiaville, A., Nakatani, Y., Miltat, J., & Vernier, N., "Domain wall motion by spin-polarized current: a micromagnetic study," Journal of Applied Physics, 95(11), 7049-7051 (2004).

[120] Roy, K., Bandyopadhyay, S. and Atulasimha, J., "Hybrid spintronics and straintronics: A magnetic technology for ultra low energy computing and signal processing," Applied Physics Letters, 99, 063108 (2011)

[121] Kunz, A., "Simulating the maximum domain wall speed in a magnetic nanowire," Ieee Transactions on Magnetics, 42(10), 3219-3221 (2006).

[122] Bryan, M. T., Fry, P. W., Fischer, P. J., & Allwood, D. A., "Observation of field-induced domain wall propagation in magnetic nanowires by magnetic transmission x-ray microscopy," Journal of Applied Physics, 103(7) (2008).

[123] Bryan, M. T., Schrefl, T., Atkinson, D., & Allwood, D. A., "Magnetic domain wall propagation in nanowires under transverse magnetic fields," Journal of Applied Physics, 103(7) (2006).

[124] Glathe, S., Berkov, I., Mikolajick, T., & Mattheis, R., "Experimental study of domain wall motion in long nanostrips under the influence of a transverse field," Applied Physics Letters, 93(16) (2008).

[125] Glathe, S., Mattheis, R., & Berkov, D. V., "Direct observation and control of the Walker breakdown process during a field driven domain wall motion," Applied Physics Letters, 93(7) (2008).

[126] Schryer, N. L. and Walker, L. R., "The motion of 180° domain walls in uniform dc magnetic fields," J. Appl. Phys. 45, 5406 (1974)

[127] Tsoi, M., Fontana, R. E., & Parkin, S. S. P., "Magnetic domain wall motion triggered by an electric current," Applied Physics Letters, 83(13), 2617-2619 (2003).

[128] Klaui, M., Vaz, C. A. F., Bland, J. A. C., Monchesky, T. L., Unguris, J., Bauer, E., . . . Cui, Z., "Direct observation of spin configurations and classification of switching processes in mesoscopic ferromagnetic rings," Physical Review B, 68(13) (2003).

[129] Klaui, M., Vaz, C. A. F., Lopez-Diaz, L., & Bland, J. A. C. "Vortex formation in narrow ferromagnetic rings," Journal of Physics-Condensed Matter, 15(21), R985-R1023 (2003).

[130] Klaui, M., Vaz, C. A. F., Rothman, J., Bland, J. A. C., Wernsdorfer, W., Faini, G., & Cambril, E., "Domain wall pinning in narrow ferromagnetic ring structures probed by magnetoresistance measurements," Physical Review Letters, 90(9) (2003).

[131] Hu, J. M., Sheng, G., Zhang, J. X., Nan, C. W., & Chen, L. Q., "Phase-field simulation of strain-induced domain switching in magnetic thin films," Applied Physics Letters, 98(11) (2011).

[132] Wang, J. J., Hu, J. M., Ma, J., Zhang, J. X., Chen, L. Q., & Nan, C. W., "Full 180 degrees Magnetization Reversal with Electric Fields," Scientific Reports, 4 (2014).

[133] Biswas, A. K., Bandyopadhyay , S. and Atulasimha, J., "Energy-efficient magnetoelastic non-volatile memory," Appl. Phys. Lett. 104, 232403 (2014).

[134] Liang, C. Y., Keller, S. M., Sepulveda, A. E., Sun, W. Y., Cui, J. Z., Lynch, C. S., & Carman, G. P., "Electrical control of a single magnetoelastic domain structure on a clamped piezoelectric thin film-analysis," Journal of Applied Physics, 116(12) (2014).

[135] Hockel, J. L.; Bur, A.; Wu, T.; Wetzlar, K. P.; Carman, G. P."Electric Field Induced Magnetization Rotation in Patterned Ni Ring/Pb(Mg1/3Nb2/3) O3](1–0.32)-[PbTiO3]0.32 Heterostructures," Applied Physics Letters, 100, 022401 (2012)

[136] Sohn, H., Nowakowski, M. E., Liang, C-Y, Hockel, J. L., Wetzlar, K., Keller, S., McLellan, B. M., Marcus, M. A., Doran, A., Young, A., Kläui, M., Carman, G. P., Bokor, J., and Candler, R. N., "Electrically Driven Magnetic Domain Wall Rotation in Multiferroic Heterostructures to Manipulate Suspended On-Chip Magnetic Particles," ACS Nano, 9 (5), pp 4814–4826 (2015).

[137] Liang,C.-Y., Keller,S. M., Sepulveda, A.E., Bur A., Sun,W.-Y.,Wetzlar,K., and Carman,G.P., "Modeling of magnetoelastic nanostructures with a fully coupled mechanical-micromagnetic model," Nanotechnology 25 435701 (2014).

[138] Hu, J-M., Yang, T., Wang, J., Huang, H., Zhang, J., Chen, L-Q, and NanC-W, "Purely Electric-Field-Driven Perpendicular Magnetization Reversal," Nano Letters, 15 (1), pp 616–622 (2015)

[139] Cheng-Yen Liang, Abdon E. Sepulveda, Daniel Hoff, Scott M. Keller, Gregory. P. Carman, *"Strain-mediated Deterministic Control of 360^o Domain Wall Motion in Magnetoelastic Nanorings,"* Journal of Applied Physics (2015)

[140] Noel D'Souza, Mohammad Salehi Fashami, Supriyo Bandyopadhyay, and Jayasimha Atulasimha, "Experimental Clocking of Nanomagnets with Strain for Ultralow Power Boolean Logic," Nano Lett., 2016, 16 (2), pp 1069–1075.

[141] Ayan K. Biswas, Supriyo Bandyopadhyay and Jayasimha Atulasimha, "Complete magnetization reversal in a magnetostrictive nanomagnet with voltage-generated stress: A reliable energy-efficient non-volatile magneto-elastic memory," Appl. Phys. Lett. 105, 072408 (2014).